This is to certify that the
dissertation entitled

SCALING STELLAR FEEDBACK: A STUDY OF THE PHYSICAL PROCESSES INVOLVED IN STAR-FORMING REGIONS OF VASTLY DIFFERENT SIZES

presented by

Eric W. Pellegrini

has been accepted towards fulfillment
of the requirements for the

Ph.D. degree in Physics and Astronomy

Major Professor's Signature

July 9, 2009

Date

**Doctoral Dissertation**
**BOOKPLATE INSTRUCTIONS**

*MSU is an Affirmative Action/Equal Opportunity Employer*

# SCALING STELLAR FEEDBACK: A STUDY OF THE PHYSICAL PROCESSES INVOLVED IN STAR-FORMING REGIONS OF VASTLY DIFFERENT SIZES

By

Eric W. Pellegrini

A DISSERTATION

Submitted to
Michigan State University
in partial fulfillment of the requirements
for the degree of

DOCTOR OF PHILOSOPHY

Physics and Astronomy

2009

**ABSTRACT**

SCALING STELLAR FEEDBACK: A STUDY OF THE PHYSICAL PROCESSES INVOLVED IN STAR-FORMING REGIONS OF VASTLY DIFFERENT SIZE

By

Eric W. Pellegrini

Regions of recent or ongoing star formation often contain massive stars capable of ionizing the surfaces of nearby molecular clouds. These layers of ionized gas, called H II regions, produce emission lines that serve as beacons of star formation as we look out into distant parts of our Galaxy and the universe. The complex physical processes of star formation are responsible for the chemical and structural evolution of galaxies throughout the history of the universe on many size scales. Light and winds from massive stars heat and compress nearby clouds, acting to simultaneously inhibit and enhance further star formation. To disentangle the importance of competing processes such as photoionization, supernovae, stellar winds, magnetic fields, radiation pressure, I have studied the dominant physical processes in nearby H II regions to determine the relative contribution of each feedback mechanism as a function of star formation intensity. The Orion Nebula is an H II region that is visible to the naked eye. Due to its proximity to the Sun and brightness, it has been studied extensively in all wavelengths. It is dominated by a single O star and offers the least complex environment to compare with models of H II regions. The most complex site of star formation in the local universe is 30 Doradus in the Large Magellanic Cloud. Hundreds of O stars dominated a region thousands of times larger than the Orion Nebula. Together these two examples provide the constraints necessary to quantify stellar feedback on different scales.

## Dedication

This dissertation is dedicated to all those family and friends who helped me overcome various obstacles as I struggled toward the finish line. With out the friendship and family support Joe, Joni and Dick Guerne provided the outcome of the effort would have far more uncertain. And to those who have suffered the most, my son Connor and wife Jennifer I dedicate this work.

Acknowledgments

I would like to thank the Center for the Study of Cosmic Evolution for their support via a fellowship in my last semester, the Graduate School for providing a Dissertation Completion Fellowship. I wish to also thank Dr. Horace Smith for maintaining my position as a T.A at the campus observatory for many semesters.

I owe Gary Ferland a special thanks, not only for the financial support, but also your time. You were always available, even during Christmas. And while completing this dissertation I found it helpful to remind myself that I was building a model of a plane, and not an actual plane, or I would never have finished.

I owe my largest debt of gratitude to Jack Baldwin, most of all for h unending patience. When I first started you always prioritized my class work during the school year and I thank you for that. You also taught me the importance of knowing now only how to operate an instrument, but to understand *how* it works. Thank you for allowing me to "drive" during observing runs and teaching me the finer detail of observing. The knowledge you have passed on will serve me well until the end of my career.

You have always demonstrated a well balanced attitude toward work and home. You never asked my to put my research before my family, and were conscience of when I did it anyway. For that, Jennifer, Connor and I are grateful.

## TABLE OF CONTENTS

LIST OF TABLES

LIST OF FIGURES

## SYMBOLS AND ABBREVIATIONS

$\odot$ - Solar

30 Dor – 30 Doradus

ALMA – Atacama Large Millimeter Array

arcmin – arcminute

GEHIIR – Giant Extragalactic HII Region

HST – Hubble Space Telescope

IR – InfraRed

ISM – InterStellar Medium

JWST – James Webb Space Telescope

$n$ — volume density

$P$ — Pressure

PA – Position Angle

PAH – Poly-Aromatic Hydrocarbons

SED – Spectral Energy Distrobution

$T$ — Temperature

$U$ — Ionization parameter

$Z$ — Metallicity, usually defined by the O/H ratio.

Chapter 1

Pellegrini, Eric W., Baldwin, Jack A., Ferland, Gary J., Shaw, Gargi, Heathcote, S. (2009), Orion's Bar: Physical Conditions Across the Definitive $H^+$/ $H^0$/ $H_2$ Interface. Astrophysical Journal, 693:285-302

# Orion's Bar: Physical Conditions across the Definitive $H^+$ / $H^0$ / $H_2$ Interface

E.W. Pellegrini & J.A. Baldwin
*Physics and Astronomy Department, Michigan State University, 3270 Biomedical Physical Sciences Building, East Lansing, MI 48824*

G.J. Ferland
*Department of Physics and Astronomy, University of Kentucky, 177 Chemistry/Physics Building, Lexington, KY 40506*

Gargi Shaw
*Department of Astronomy and Astrophysics, Tata Institute of Fundamental Research, Mumbai-400-005, India*

S. Heathcote
*SOAR Telescope, Casilla 603, La Serena, Chile*

pelleg10@pa.msu.edu

**Abstract**

Previous work has shown the Orion Bar to be an interface between ionized and molecular gas, viewed roughly edge on, which is excited by the light from the Trapezium cluster. Much of the emission from any star-forming region will originate from such interfaces, so the Bar serves as a foundation test of any emission model. Here we combine X-ray, optical, IR and radio data sets to derive emission spectra along the transition from $H^+$ to $H^0$ to $H_2$ regions. We then reproduce the spectra of these layers with a simulation that simultaneously accounts for the detailed microphysics of the gas, the grains, and molecules, especially $H_2$ and CO. The magnetic field, observed to be the dominant pressure in another region of the Orion Nebula, is treated as a free parameter, along with the density of cosmic rays. Our model successfully accounts for the optical, IR and radio observations across the Bar by including a significant magnetic pressure and also heating by an excess density of cosmic rays, which we suggest is due to cosmic rays being trapped in the compressed magnetic field. In the Orion Bar, as we had previously found in M17,

momentum carried by radiation and winds from the newly formed stars pushes back and compresses the surrounding gas. There is a rough balance between outward momentum in starlight and the total pressure in atomic and molecular gas surrounding the $H^+$ region. If the gas starts out with a weak magnetic field, the starlight from a newly formed cluster will push back the gas and compress the gas, magnetic field, and cosmic rays until magnetic pressure becomes an important factor.

**1. Introduction**

The interactions between light and winds from a newly-formed cluster and the molecular cloud in which the stars were born sculpts the geometry of the regions, produces the observed spectrum, and is a feedback mechanism that throttles the rate of star formation. To explore these processes in detail we are revisiting a series of well-studied nearby star forming regions. In particular we are examining objects with geometries viewed nearly edge-on, allowing us to measure the effect magnetic fields have at different depths as the starlight penetrates into the cloud. We use the observed stellar parameters, gas densities, and multi-wavelength emission-line spectrum to strongly constrain a numerical simulation of the physical conditions and emission along a ray from the central stars through the $H^+$, $H^0$, and $H_2$ regions. We include the effects of dust and of detailed molecule destruction and formation processes, and treat the detailed micro-physics of the $H^+$, $H^0$, and $H_2$ regions self-consistently. The only free parameters in simulations of a well observed cloud will be the cosmic ray density and magnetic field strength. In some cases the field can be directly measured. It is never possible to measure the cosmic rays directly so this approach is one of the few ways to infer their properties, although they are known to be produced in star-forming regions and can energize emission-line regions.

The modeling approach described in the preceding paragraph was recently applied to the Galactic H II region M17 (Pellegrini et al 2007; hereafter Paper I). That object contains a heavily obscured

and nearly edge-on interface that is excited by about a dozen O stars. This interface is of particular interest because it is a rare case where the magnetic field can be measured in the adjacent $H^0$ region (or photodissociation region, the PDR). This is possible because radio continuum emission from the $H^+$ zone provides a background light source against which Zeeman polarization can be measured with the H I 21cm line (Brogan et al. 1999; Brogan & Troland 2001). The magnetic field is strong and magnetic pressure is important (see § 3 below). Combining the Zeeman measurements together with existing radio, infrared, and X-ray maps and new optical spectroscopy, we found that the structure of M17 is well described by a model in which the outward momentum carried by the stellar radiation field, together with pressure from a stellar wind-blown bubble, has compressed the gas and its associated magnetic field until the magnetic pressure built up sufficiently to be able to halt the process. The overall geometry is set by hydrostatic equilibrium. In addition, the density of cosmic rays is enhanced as a result of partial trapping of the charged cosmic ray particles by the compressed magnetic field, so that cosmic ray heating is important in atomic regions. We consider this to be a very natural cause-and-effect explanation of why the M17 gas cloud has taken on its present form.

Here we investigate whether this is also a good description of another edge-on interface – the well-known Bar in the Orion Nebula. Because it is very close to us (here we adopt a distance of 437 pc; Hirota et al. 2007), Orion is perhaps the best studied of all H II regions, with data across the entire electromagnetic spectrum. A schematic of the geometry is shown as Figure 8.4 of Osterbrock & Ferland (2006, hereafter AGN3). The ionizing radiation field is dominated by the hot O star $\theta^1$ Ori C. Light from this star is steadily dissociating the background molecular cloud, resulting in a blister type geometry in which the $H^+$ region is a hot skin on the surface of the molecular cloud. A large cavity has been carved out of the molecular gas, breaking out of the cloud on the side nearest the Earth so that we can see through the bubble to the $H^+$ region on the

back wall (Zuckerman 1973; Balick et al. 1974; Baldwin et al. 1991, hereafter BFM91; Wen & O'Dell 1995; Ferland 2001; O'Dell 2001). The hot gas filling this cavity has recently been detected by Güdel et al (2008).

Given the important role that magnetic pressure plays in M17, it is natural to ask whether it might also be important in Orion. While there are no direct observations of the field strength in the atomic gas associated with the Orion Bar, the Orion complex shows a well-structured polarization pattern that drops to a low level of polarization in the Bar, suggesting that the magnetic field in the Bar is directed more or less along our line of sight (Schleuning 1998). This is the expected orientation for an initially tangled magnetic field frozen into gas that has been compressed by radiation pressure or stellar winds from $\theta^1$ Ori C. There are Zeeman measurements for the Orion Veil (a foreground structure that is associated with the Orion Molecular Cloud) showing that $B_{los}$ ~ 50 μG (Brogan et al. 2005). This is already an order of magnitude greater than the Galactic background of 5-10μG (Tielens & Hollenbach 1985), even though $B_{los}$ only represents the line of sight component. Detailed analysis suggests that the ratio of magnetic to gas pressure in the Veil is large (Abel et al. 2004, 2006). A further indication of the presence of a strong *B* field in the Veil is an indirect study using infrared line ratios (Abel and Ferland 2006), which indicated that along the line of sight to $\theta^1$ Ori C the ratio of magnetic/gas pressure is $P_{mag}/P_{gas} > 1$. Aside from the suggestive results of the Veil, turbulent velocities in the atomic region of the background cloud are supersonic and it has been suggested that magnetic fields are responsible (Kristensen et al. 2007; Roshi 2007). These results lend plausibility to the possible presence of a strong magnetic field in the Bar region.

The Bar appears as a bright ripple on the background ionization front, lying at a projected distance from $\theta^1$Ori C of 111 arcsec (0.23 pc). In an important series of papers Tielens et al (1993), Tauber et al. (1994), and Young Owl et al. (2000) showed that the $H^0$ and $H_2$ regions in

the Bar are easily resolved on the sky as separate structures displaced from each other in a way that clearly demonstrates that the Bar is indeed a roughly edge-on interface. They showed that most of the observed emission in PAHs, [O I], [C II], $H_2$ and the $^{12}CO$ J=1–0 lines can be understood as coming from a homogeneous region with density $n_H \sim 5\times 10^4$ cm$^{-3}$. However, they argued that large (9 arcsec = 0.02 pc) clumps with about 20 times higher density must be imbedded in this homogeneous medium to produce the observed high-level CO lines (J=14–13, 7–6) and also the $HCO^+$ and HCN emission. Indeed, their interferometer images directly show clumpy structures in these lines but not in the many lines attributed to the homogeneous medium. Those investigations considered only the molecular and neutral atomic regions of the Bar. The density chosen by Tauber et al. (1994) for their model was inferred from the observed offsets of the $H_2$ and $^{12}CO$ emission in the Bar relative to the ionization front, combined with the column density required to allow the observed CO emission to be produced. In doing so, the authors assumed constant gas density in the $H^0$ region, arguing that turbulence dominated the pressure. Van der Werf et al. (1996) combined new $H_2$ observations with the existing data set of the PDR and postulated that $H_2$ emission from the interclump medium required a filling factor less than unity for the interclump gas. Contradicting this result, Allers et al. (2005) also modeled the interclump region with constant pressure, not constant density. They concluded that a filling factor of unity described the region well. However they also found that an extra heating agent must be present in the Bar, but were unable to establish what it might be.

Here we investigate the physical conditions across the Bar that are implied by the variations of its spectrum across its full width. Like the previous work, we use the observed gas density, stellar parameters, and emission peak offsets. However, we consider the emission from the $H^+$ and PDR regions together in a self-consistent picture. By more fully understanding what determines the structure of the Bar we can better understand the general nature of such interfaces. Here we focus

on a line of sight through the interclump medium, not on the clumps described by Young Owl et al. (2000) and others. Like many (but not all) previous papers we conclude that the interclump medium dominates and determines the overall structure of the Bar. We find that the observed densities and the radial extent of the various stratified emission regions through the Bar are in fact the natural consequences of a cloud in roughly hydrostatic equilibrium, in which magnetic pressure and cosmic ray heating play major roles in the $H^0$ region. This study, combined with the companion work by Shaw et al. (2008; hereafter Paper III), which focuses on the detailed $H_2$ emission spectrum, lead to a better picture of the nature of these interfaces.

**2. The Observational Data Set**

The Orion Nebula has been observed extensively at all wavelengths. For this study of the Bar we draw on the following published data sets. From Tauber et al. (1994) we use maps of the $^{12}CO$ and $^{13}CO$ emission lines, and their summary of previous mid-IR observations of the CO 7–6, CO 14–13, O I λ63 μm, O I λ143 μm, C II λ158 μm, Si II λ35 μm, C I λ609 μm and C I λ370 μm emission lines. The $H_2$ 1-0 S(1) data are originally from van der Werf et al. (1996), who find an average surface brightness of $5.9\times 10^{-15}$ erg $s^{-1}$ $cm^{-2}$ $arcsec^{-2}$. However, the $H_2$ surface brightness varies significantly along the Bar. A05 and Young Owl et al. (2000) used the van der Werf et al. $H_2$ data set but extracted surface brightness profiles along different narrow lines perpendicular to the Bar. A05 did this for a particularly bright region and found a peak brightness of about $9\times 10^{-15}$ erg $s^{-1}$ $cm^{-2}$ $arcsec^{-2}$. Young Owl et al. (2000) did the same for a fainter region which is along the same cut for which most of the other published molecular data used here were measured, and found the peak $S(H_2)$ 1-0 S(1) = $3.3\times 10^{-15}$ erg $s^{-1}$ $cm^{-2}$ $arcsec^{-2}$. For consistency we adopt the Young Owl et al. $H_2$ surface brightness profile. The peak surface brightnesses of these emission lines are summarized in Table 1.1 with observed values in column 2 and results of our three models described below in columns 3 through 5.

Besides $H_2$ and CO, many other molecules are detected in the Bar. Here we will also compare our predictions with observations for $CO^+$ (Störzer et al. 1995), $SO^+$ (Fuente et al. 2003), CN (Simon et al. 1997), CS (Simon et al. 1997, Hogerheijde et al. 1995), SiO (Schilke et al . 2001), and SO (Leurini et al. 2006).

Pogge et al. (1992) made optical passband Imaging Fabry-Perot maps of Hα, Hβ, [O III] λ5007, [N II] λλ6548, 6583, [S II] λλ6716, 6731 and He I λ6678, and in their Figure 5 show a density profile across the Bar, measured from the [S II] λ6716/λ6731 intensity ratio. Wen & O'Dell (1995) used the Pogge et al. data to make a 3-dimensional map of the $H^+$ region in Orion and their Figure 4 shows intensity profiles across the Bar for several lines including Hα. García-Díaz & Henney (2007) mapped a number of optical emission lines by taking an extensive grid of echelle long-slit spectra, and in their Figure 9 show a density profile across the Bar (from the [S II] intensity ratio) that is very similar to the Pogge et al. (1992) result. From these papers, we have especially depended on several figures showing line intensities along the cuts across the Bar shown here in Figure 1.1.

To this existing data set we added an intensity profile across the Bar in [S II] λ6713+λ6731, measured from a continuum-subtracted, narrow-band [S II] image taken on 06 April, 2007 with the Southern Astrophysical Research (SOAR) Telescope [1]. The [S II] filter is 45Å wide and is centered at λ6723, while the continuum filter is centered at 6850Å with a width of 95Å.[2] The SOAR Optical Imager (SOI) was used; it provides a 5× 5 arcmin field of view with a 2× 2 binned pixel scale of 0.15 arcsec/pixel and yielded images with 0.6 arcsec FWHM in both filters. The images were processed in IRAF in the usual way, then the continuum image was scaled to

[1] The Southern Astrophysical Research Telescope is a joint project of Michigan State University, Ministério da Ciência e Tecnologia-Brazil, the University of North Carolina at Chapel Hill, and the National Optical Astronomy Observatory. Further information about SOAR and its instruments may be found at www.soartelescope.org.

[2] We are grateful to Dr. Frank Winkler for loaning us the filters.

unsaturated stars in the nebula and subtracted from the emission line image. Next, the continuum-subtracted [S II] image was flux calibrated using the emission-line surface brightness measurements from the long-slit spectrophotometry of BFM91, following the example of O'Dell and Doi (1999). Finally, the [S II] intensity profile was measured along the same cut as is shown in Figure 1.1 for the Wen & O'Dell Hα profile.

Figure 1.2 combines together the four key intensity profiles that we will use to constrain our models of the Bar. The ionizing radiation comes in from the left. Using the new SOAR [S II] images, the different profiles have all had their zero points set to match the distance from the peak in the [S II] emission along each cut. There are several key features to note. The ionization front (IF) is assumed to be at the position of the peak [S II] emission. Hα emission comes from a broad plateau before (to the left of) the IF. The $H_2$ brightness profile peaks about 12 arcsec after the IF (i.e. deeper into the cloud). In the $^{12}$CO J = 1–0 line the peak intensity occurs about 20 arcsec after the IF and is very broad.

As can be seen in Figure 1.1, these cuts across the Bar are not at identical locations. The Wen & O'Dell Hα profile and our [S II] profile are averaged over 20 arcsec wide swathes extending in PA 322 deg from $\theta^1$ Ori C, while the $^{12}$CO (from Tauber et al. 1994) and $H_2$ profiles (Young Owl et al. 2000) are taken in PA 315 deg crossing the Bar about 60 arcsec SE of the Hα and [S II] cuts. However, close examination of maps of the [S II] ratio in the vicinity of the Bar (e.g. Fig. 11 of Henney et al. 2005a), and the similarities of the same lines published for a different position along the Bar (Young Owl et al. 2000) indicates that the relative offsets and shapes of the different line profiles are typical of the interclump component of the Bar as a whole, and therefore are valid criteria for fitting our models.

## 3. A ray through the $H^+$ / $H^0$ / $H_2$ Layers of the Bar

### 3.1 Numerical simulations of the Bar

The bright ridge of emission seen as the Bar in Figure 1.1 is a region where the gas goes from $H^+$, closest to the central stars, through $H^0$ when ionizing radiation has been attenuated, eventually becoming $H^2$ when ultraviolet light is sufficiently extinguished (see also Figures 8.4 and 8.6 of AGN3). We derive physical conditions across the Bar by comparing predicted and observed spectra at various distances away from the star cluster (as represented by $\theta^1$ Ori C). The simulations are done with the spectral synthesis code Cloudy. Last described by Ferland et al. (1998),[3] Cloudy has since been updated to include a large model of the hydrogen molecule (Shaw et al. 2005), more complete grain physics (van Hoof et al. 2004) and the chemistry of a PDR (Abel et al. 2005). We used the publicly available version of Cloudy, but with updated $H_2$ collision rates as described in Paper III.

We begin the calculation at the ionized or illuminated face of the $H^+$ region and follow a beam of starlight away from the central cluster into the molecular cloud. The $H^+$, $H^0$ and $H_2$ regions are actually a flow from cold molecular gas through the atomic region into hot and ionized gas with the ionizing radiation gradually eating into the molecular cloud. However, we approximate the situation here with a hydrostatic model. We will present predicted and observed quantities along this line from the stars into the molecular cloud, with the ionizing radiation coming in from the left in all relevant figures.

The most important assumption in all of this is that the conditions within the various regions are related to one another by continuous variations in the gas, radiation, and magnetic pressures. The equation of state, the relationship between these pressures and the density, is described in Paper I and further in Appendix A. Because the structure of the $H^+$, $H^0$ and $H_2$ regions are all the result of a single calculation, with a single set of initial conditions, we minimize the number of

[3] Many additional physical processes described in Cloudy are documented and referenced in Hazy, the approximately 1500 page Cloudy manual. It can be downloaded from ftp://gradj.pa.uky.edu/gary/cloudy_gold/docs

adjustable parameters compared to the number of observational constraints. As will be shown in section 4.1 our best model will have only 6 arbitrary input parameters, but will satisfactorily match 17 observational constraints. For example, the UV radiation that penetrates into the PDR is the result of a detailed treatment of radiation transport through the $H^+$ region. By treating the $H^+$ region and PDR together in a single calculation, the radiation affecting the PDR is guaranteed to be consistent with the observed properties of $\theta^1$ Ori C and the gas density of the $H^+$ region. The emission from ionized and neutral atoms, grains and PAH chains, and several molecular species including $H_2$ and CO, are all predicted by self-consistently treating the microphysics of the gas. Starlight is attenuated by each layer and passed on to more distant regions. All models were also required to reproduce the observed 111 arcsec projected offset of the [S II] emission from $\theta^1$ Ori C, which clearly defines the Bar's ionization front.

The location of the illuminated face of the $H^+$ region, and the gas density there, are set by the Hα emission profile. There is a steep drop in the Hα surface brightness where the $H^+$ zone ends and the $H^0$ zone begins. There is no similar sharp rise to mark the illuminated face of the Bar because the light emitted by the edge-on Bar structure is diluted by additional emission coming from parts of the $H^+$ region which are on the background cavity surface but which lie along the same line of sight. Therefore, the initial density and radius of our models can only be constrained by their effects beyond the illuminated face. These initial parameters are chosen so that the observed Hα and [S II] surface brightness and [S II] doublet ratio are matched. Since we assume hydrostatic equilibrium the gas pressure increases as starlight with its associated momentum is absorbed. This causes an increase in density and emission measure, $n^2\ dV$, producing the observed brightness profile.

The parameters assumed in our simulations are largely observationally based and are summarized next. The main free parameters will be the magnetic field intensity and cosmic ray density. We assume flux freezing and a scrambled magnetic field to relate the gas density and field.

Three models are presented here, designated (1) Gas Pressure Model, (2) Magnetic Field Model and (3) Enhanced Cosmic Ray Model. They all share the following assumptions:

- The grain optical properties, described by BFM91, are based on the observed extinction in Orion. Many previous investigations, going as far back as Tielens & Hollenbach (1985), assume standard ISM extinction. Orion grains have a more nearly grey dependence of extinction on wavelength compared with ISM grains, changing the structure of the layers. The Orion size distribution is deficient in small particles so produces less heating of the gas by grain electron photo-ejection.
- The PAH abundance is $n_{PAH}/n_{H0} = 3\times 10^{-7}$ (Draine et al. 2007) with a power-law distribution of PAH sizes with 10 size bins, according to Bakes & Tielens (1994).
- We assume overall hydrostatic equilibrium as described in Appendix A, with magnetic fields (when included) described by Eq. A1 with $\gamma = 2$.
- The gas-phase abundances are the standard Cloudy values for H II regions, and are largely based on observations of the Orion Nebula described by BFM91, Osterbrock et al (1992), and Rubin et al (1991, 1993). These abundances are listed in Table 2 of Paper III.
- We have taken the distance to the Orion Nebula to be 437± 19 pc (Hirota et al. 2007). This is a VLBI parallax measurement, which should be more accurate than previous results.
- All models are constrained to reproduce the observed [S II] ratio I(λ6716)/I(λ6731) = 0.63 ± 0.05, converted from the reported electron density of $n_e \sim 3200$ cm$^{-3}$ at the peak of the Bar (Pogee et al. 1992). This is consistent with the [S II] ratios reported by García-

Díaz & Henney (2007) for the Bar. The calculations predict the full spectrum including this ratio. We match this ratio instead of using a deduced density since the conversion from ratio to density depends on the kinetic temperature and ratio of electrons to atoms.

- The observed stellar X-ray emission caused by wind activity immediately around the Trapezium stars is modeled with a bremsstrahlung distribution with a temperature $T = 10^6$K and an integrated luminosity $L_X = 10^{32.6}$ erg s$^{-1}$ over the 0.5–8 keV passband (Feigelson et al. 2005). This represents the X-ray emission from just $\theta^1$ Ori C. There are additional X-ray point sources in this region besides $\theta^1$ Ori C, but their positions along the line of sight are poorly known. Omitting them is not likely to be a large source of error because $\theta^1$ Ori C accounts for 68% of the total observed X-ray flux from the Orion region. The diffuse X-ray emission detected by Güdel et al (2008) is much weaker than the stellar contribution.
- A constant turbulent velocity was assumed. The observed $^{13}$CO line width is 1.8 km s$^{-1}$ FWHM (Tauber et al. 1994), while the $H_2$ line widths are in the range 2–4 km s$^{-1}$ after allowance for a poorly known instrumental profile (A05). Here we adopt a constant turbulent velocity of 2 km s$^{-1}$ FWHM throughout the nebula and include it as a source of pressure in our models.

The three models are described below. Each builds on the results from the preceding one by adding additional physical processes.

### 3.2 The Gas Pressure Model

This first model represents the BFM91 hydrostatic model of the $H^+$ region. It does not include a magnetic field but does include radiation and turbulent pressure. We shall refer to this as the gas pressure model even though turbulent and radiation pressures make significant contributions. Cosmic ray heating and ionization are included in the calculation using a cosmic ray density set to

the Galactic average of $2.6\times 10^{-9}$ $cm^{-3}$ (Williams et al. 1998). The ionization rate per particle corresponding to this density is $2.5\times 10^{-17}$ $s^{-1}$ for $H^0$ and $5\times 10^{-17}$ $s^{-1}$ for molecular $H_2$. For this model the heating due to cosmic rays is mostly insignificant, with the cosmic rays peaking at 15% of the heating in the coldest and most neutral regions, where the starlight is heavily extinguished. Collisional heating of grains (Drain 1978) is the most important heating mechanism in the molecular region, providing 70% of the total heating. In this model we find the heating in the deep molecular gas is not dominated by cosmic rays but by grain heating processes, consistent with the conclusions of A05.

Figure 1.3 shows our assumed geometry. The Bar is a thin slab tilted slightly to our line of sight. Because the hydrogen ionization front is thin, the observed [S II] profile on the sky is very sensitive to the angle of inclination. The thin slab extends 0.115 pc along the line of sight and is inclined 7 deg relative to the line of sight. This is very similar to many previous models of the Bar's geometry (eg. Tielens et al. 1993; Hogerheijde et al. 1995; Wen & O'Dell 1995; Walmsley et al. 2000; A05).

For a given incident ionizing flux $\Phi$(H) photons $s^{-1}$ $cm^{-2}$, the shape and intensity of the [S II] profile is set by the initial hydrogen density $n_0$(H). This also defines the position of the hydrogen ionization front. The problem is that we do not initially know either $\Phi$(H) or $n_0$(H).

The number of ionizing photons per second $Q$(H) emitted by $\theta^1$ Ori C and hence the ionizing flux $\Phi$(H) incident upon the slab is uncertain. Although the star's spectral type is clearly O6.5, there is a significant range in the $Q$(H) and effective temperature values that are thought to be appropriate for even a "normal" O6.5 star. At the high end is $Q(H) = 10^{49.23}$ $s^{-1}$ with $T_{eff}$ = 42,300 K (Vacca et al. 1996), while Hanson et al. (1997) adopted the much lower value $Q(H) = 10^{48.89}$ $s^{-1}$ and $T_{eff}$ = 41,200 K for this spectral type. Intermediate values are suggested by Smith et al. (2002) and Sternberg et al. (2003). In addition to this uncertainty, $\theta^1$ Ori C has an unusually strong magnetic

field, which is thought to channel the flow of stellar winds from the star in ways that modulate the observed spectrum (Wade et al. 2006). This could produce a significantly anisotropic radiation field.

Given the above uncertainty, we explored a range of values of $T_{eff}$ and $Q$(H). Our models have only a very slight dependence on the exact value of $T_{eff}$, but the value used for $Q$(H) clearly does matter. Changing $Q$(H) while matching all the observations of the $H^+$ region, including the density $n_e$ which is a measured quantity, does not significantly affect the predictions for the $H^0$ and $H_2$ regions, but it does change the deduced distance between $\theta^1$ Ori C and the ionization front. Since the projection of this distance on the sky is fixed, the position of the slab along our line of sight must change relative to $\theta^1$ Ori C to match the observed geometry. For the largest $Q$(H) value cited above the slab would have to lie about 0.125 pc farther away from us than in the adopted model, while maintaining the same inclination angle relative to our line of sight. We eventually adopted the Kurucz (1979) stellar model as the continuum shape of $\theta^1$ Ori C with $Q(H) = 10^{49.00}$ $s^{-1}$ and $T_{eff}$ = 39,700 K. This $Q$(H) is the same as was used in the 3D model for which Wen and O'Dell (1995) show figures, and also was used in the hydrodynamic wind models computed by Henney et al. (2005a), simplifying comparison to those papers.

However, this still left many combinations of the Bar's thickness $l$ along the ray from $\theta^1$ Ori C and in its density $n_0$(H) at the illuminated face, and consequently of the radial gas density distribution $n_H(r)$, which were consistent with the constraints used so far. We used the additional constraints of the Hα and [S II] brightness profiles together with the [S II] λ6716/λ6731 intensity ratio to determine the remaining properties of the entire $H^+$ zone. The electron density $n_e \sim n_H$ is directly measured in the region where the [S II] lines are formed, so the [S II] surface brightness was used to determine the distance $h$ through the Bar *along the line of sight* using

$$S([\text{S II}]) \propto n_S + n_e h. \qquad (1)$$

Then the Hα surface brightness at other points on the Bar was used to determine the relationship between density and position on the sky for the known $h$. Besides increasing the peak surface brightness, a higher $n_H$ also decreases the deduced thickness $l$ of the $H^+$ region.

The result of this was a model, with predicted emission line strengths and magnetic field summarized in column 3 of Table 1.1, which reproduced the structure and emission of the $H^+$ region. In this model, $h$ = 0.115 pc, the illuminated face of the cloud lies 0.114 pc from $\theta^1$ Ori C, $l$ = 0.141 pc, and $\Phi$(H) = 6.45× $10^{12}$ $s^{-1}$ $cm^{-2}$.

The bottom row of Figure 1.4 shows the pressure sources and $H^+$, $H^0$ and $H_2$ density distributions calculated for the gas pressure model. This figure also includes the same plots for the other two models which are described in the following two sections.

Figure 1.5 shows, again for all three models, how well the computed surface brightness distributions of [S II], Hα, $H_2$ and CO lines match the observations. The results for the gas pressure model are shown in the left-hand column. We computed the conditions and locally emitted spectrum for each point along a ray from the central star through the layers shown in Figure 1.3. For the case of optically thin lines ([S II], Hα and $H_2$), the comparisons of the models to the observed surface-brightness distributions were made by integrating the volume emissivity along the line of sight into the cloud according to

$$S_i = \int \epsilon_i(r)/4\pi \times 10^{-dA_i(r)/2.5} dh \qquad (2)$$

The integration is along the line of sight into the modeled region of thickness $h$, $\varepsilon_i$ is the volume emissivity for the $i^{th}$ line, $\vec{r}$ is the radial vector from $\theta^1$ Ori C, and $dA_i$ is the amount of internal reddening, in magnitudes, providing a correction to the observed line intensities for internal extinction by dust. The computed surface brightness of the visible-passband emission lines shown in Figure 1.5 and listed below in Table 1.1 have been increased by a factor 1.5 to account for an

additional component reflected from dust in the molecular cloud (Wen and O'Dell 1995; O'Dell et al. 1992). At longer wavelengths the Orion dust does not scatter efficiently (BFM91) so no similar correction is needed for the infrared and mm-wavelength lines.

The reddening correction is specific for each line according to the $R = 5.5$ reddening curve used for Orion. The mid-IR and longer wavelength lines are unaffected by extinction due to their long wavelength and the $H^+$ region observations have been dereddened (BFM91, Wen & O'Dell 1995). Only the analysis of the $H_2$ 2.121μm line is affected by internal extinction. This amounts to a flux decrement of roughly 40% for the models presented below. Increasing the depth of the slab along the line of sight (*i.e.* parallel to the ionization front) increases the intensities of all lines except that of the $H_2$ 2.121μm line which stays approximately constant due to the effects of extinction by dust.

The $^{12}$CO J = 1–0 line is also different because of its large optical depth. For optically thick thermalized lines the emission is directly related to the kinetic temperature of the gas via the antenna temperature $T_{antenna}$. Deep in the cloud the density is very high and the optical depth increases rapidly. The antenna temperature quickly approaches the kinetic temperature according to the equation

$$T_{antenna} = T_{kin}(1-e^{-\tau}) \qquad (3),$$

where $\tau$ is the CO line optical depth along our line of sight into the cloud and $T_{kin}$ is the computed spin temperate of the $^{12}$CO levels. Our calculations solve for $\tau$ toward the illuminated face, which we then scale to account for the enhanced path-length caused by our viewing angle (see Figure 1.3). The computed CO surface brightness curves in Fig. 1.5 show $T_{antenna}$ starting at the edge of the slab farthest from us, which from our viewing angle is projected to lie closest to $\theta^1$ Ori C.

The top-left panel in Figure 1.5 shows the excellent fit of the gas pressure model's [S II] surface brightness distribution to the data. The gas pressure model's match to the observed Hα surface brightness profile (Figure 1.5, second panel down in left-hand column), as well as [O III] 5007Å and [N II], with no further adjustments to the model, validates our assumptions.

The gas pressure model accurately describes the $H^+$ region, but does not correctly predict the positions of the $H_2$ and $^{12}CO$ emission peaks on the sky, as can be seen in the left-hand panels of Figure 1.5. This model was tuned to reproduce the observed $H^+$ emission region using only gas, radiation, and turbulent pressures. In this situation, the gas density in the $H^0$ region that is required to maintain hydrostatic equilibrium is $1.4\times 10^5$ $cm^{-3}$ (Fig. 1.4). Since the depth of the $H^0$ region is set by the path length required to reach an $A_V \sim 1$ where $H_2$ forms, this high-density $H^0$ region is quite narrow. The result of the high density is that the computed $H_2$ emission peak occurs two times closer to the ionization front than is observed (5 arcsec predicted separation rather than the observed 12 arcsec), as is seen in Fig. 1.5. This result is consistent with the theory of $H_2$ emission as presented by Black and van Dishoeck (1987) and Draine and Bertoldi (1996). For further discussion of $H_2$ we refer the reader to Paper III. For the same reason, the CO emission also peaks at a point too close to $\theta^1$ Ori C. Table 1.1 shows that the predicted peak $H_2$ emission is equal to 1.51 times the peak value, while the predicted CO emission is several times fainter than is observed.

**3.3 The Magnetic Pressure Model**

This second model uses the same constraints as the gas pressure model described above, but includes a magnetic field similar in strength to that seen in the Veil (Abel et al. 2005). The cosmic ray density was maintained at the Galactic background level. We ran a series of models with increasing values of the strength of the magnetic field at the illuminated cloud face, in the same way that we had done in Paper I for M17. The initial magnetic field sets the field strength

throughout the model since we assume flux freezing (Eq. A1 in the Appendix). The resulting magnetic pressure contributes to the total pressure according to Eq. A2. The center two panels in Figure 1.4 show the pressure contributions and densities as a function of depth in the final version of this model.

In the $H^+$ region where the temperatures are of the order $10^4$ K, gas pressure still dominates, so the gas pressure and magnetic pressure models are very similar in this region. The observed [S II] density and [S II] and Hα surface brightness profiles are matched by either model using the same initial conditions.

In the $H^0$ region the temperature drops and the gas density increases. According to equation A1, the magnetic field is amplified as well, so magnetic pressure support becomes important and further compression of the gas is halted. With a lower average density in the $H^0$ region a longer path length is required to absorb the UV photons that prevent $H_2$ from forming, so the $H^0$ region becomes more extended. Stronger fields at the illuminated face produce more magnetic pressure in the $H^0$ region, resulting in a lower density and larger thickness. We changed the initial magnetic field at the face of the cloud so that the $H_2$ emission peak occurred at its observed offset of about 10 arcsec (0.021 pc) from the ionization front. We found that an initial field of 8 μG best fits the observed brightness distribution of the $H_2$ emission line. In the $H^0$ region this field is $\langle B \rangle$ = 438 μG and the density in the $H^0$ region is $8\times 10^4$ $cm^{-3}$, about 2 times lower than the density in the gas pressure model.

With the magnetic pressure model, the brightness and position of the $H_2$ peak now match the observations (Fig. 1.5). However, the model still does not reproduce the position and antenna temperature of the $^{12}CO$ J = 1–0 emission peak or the high surface brightness in the higher-level $^{12}CO$ lines (Table 1.1).

**3.4 The Enhanced Cosmic Ray Model**

The magnetic field model fails because it does not provide sufficient heating in the deeper parts of the $H^0$ region. Based on the results from M17 in Paper I, we next explored the effect of assuming that cosmic ray particles are trapped by the compressed magnetic field, so that the cosmic ray density is also increased. The increased density of cosmic rays acts as an additional heat source, which becomes important in the region emitting the $H_2$ and $^{12}CO$ lines. The cosmic rays also increase the ionization level in molecular regions, increasing the speed of ion–molecule interactions and enhancing the CO formation rate. This moved the $^{12}CO$ J = 1–0 peak inwards toward the central stars. A second effect is that the kinetic temperature is increased and the $H_2$ emission is enhanced deep into the cloud. The model with enhanced cosmic rays produces extended $H_2$ emission beyond the emission peak. We ran models with the cosmic ray density increased by different values over the Galactic background density, up to the point where the cosmic ray energy density is in equipartition with the magnetic energy density. Figure 1.6 shows the dependence of the computed $^{12}CO$ J=1–0 brightness temperature on the cosmic ray density. The observed CO brightness temperature, peak $H_2$ intensity, and shapes and positions of the $H_2$ and CO profiles all are matched best by a cosmic ray density in equipartition with the magnetic field. That is the cosmic ray density we adopted in our final best model, which we call the enhanced cosmic ray model.

The average magnetic field, weighted by the 21 cm opacity $T_{spin}/n(H^0)$, for the enhanced cosmic ray model is $\langle B \rangle = 516\mu G$, almost $100\mu G$ higher than in the magnetic field model, where the cosmic ray density was set to the Galactic background. The difference is due to the weighting of $B$ by $T_{spin}/n(H^0)$ that is used to calculate $\langle B \rangle$. The ratio is the 21 cm opacity used by Zeeman measurements to derive $B$. In the enhanced cosmic ray model, deep regions of the cloud which would normally be fully molecular have a significant amount of $H^0$ produced by cosmic ray dissociation. The effects of the cosmic rays on the chemistry are shown in Figure 1.4. Neutral

hydrogen persists deep into the molecular core, where *B* peaks at about 530μG. Here the cosmic ray density is enhanced by a factor of $10^{3.6}$ over the Galactic background. This corresponds to an ionization rate of $1\times 10^{-13}$ $s^{-1}$ for $H^0$ and $2\times 10^{-13}$ $s^{-1}$ for $H_2$. In the case of the magnetic model, the neutral hydrogen does not coexist with $H_2$. This extended distribution of neutral hydrogen is a result of the enhanced cosmic rays and is not dominated by FUV photons. It would be incorrect to consider it part of the classically defined "PDR", but it will still affect the weighted <*B*> an observer will measure.

**4. Discussion**

**4.1 The parameters needed to fit the observations**

Our final model (the enhanced cosmic ray model) provides an integrated description of the ionized, neutral and molecular regions of the Bar. It is based on the idea that the pressure of photons from $\theta^1$ Ori C has compressed the surface of the molecular cloud, and along with it a magnetic field that was already present, until the combination of gas, magnetic and turbulent pressure became high enough to halt the compression. This model indicates that the Bar is in (quasi)hydrostatic equilibrium. This picture of the Orion Bar, combined with straightforward assumptions about the geometry, provides a good fit to the observed parameters. It reproduces the observed surface brightness profiles in the sense of both the position and the peak brightness of the Hα, [S II], $H_2$ and $^{12}CO$ emission lines. As is shown in Table 1.1, it satisfactorily reproduces the [S II] λ6716/λ6731 ratio, the integrated strengths of many other lines from the $H^+$ region, and the peak surface brightness of important atomic lines from the $H^0$ region including [O I] λ63μm, [Si II] λ34.1μm and [C II] λ158μm. We do not have a good optical spectrum with the slit set across the Bar, but we checked the predicted optical emission lines in Table 1.2 and verified that the computed optical spectrum is similar to that found by BFM91 at their position 5 on the west side of the Orion Nebula and that no unusual lines are predicted to be strong. Position 5

represents a region with a density comparable to the Bar. Our final model provides a quite good fit to the data. We matched 17 observed properties with 6 free parameters: the location of the illuminated face and the gas density at the face, the tilt of the IF and its depth along the line of sight, the magnetic field strength, and the cosmic ray density.

We arrived at this model in three steps. The properties of the $H^+$ region were determined by fitting a hydrostatic model that included only gas, radiation, and turbulent pressure – the gas pressure model. The location of the illuminated face and the gas density at the face, the tilt of the IF and the depth of the IF along the line of sight needed to be adjusted to reproduce the properties of the $H^+$ region. However, the resulting gas pressure model produced an $H^0$ region that is too narrow. To accurately fit the distance from the IF to the $H_2$ emission peak, it was necessary to add magnetic pressure. For the case of hydrostatic equilibrium this results in a decrease in the gas density, causing the $H^0$ region to become more extended and pushing the peak emission of $H_2$ and $^{12}CO$ to the observed value. However, this magnetic pressure model still failed to reproduce the observed $H_2$ and CO emission from deep in the cloud because the kinetic temperature was too low. We propose that the extra heating comes from cosmic rays trapped by the compressed magnetic field, the same thing that appears to be happening in M17. This fully reproduces the emission and geometry.

**4.2 Predicted column densities of additional molecules**

Cloudy includes 94 molecules in its calculations, using data mainly from the UMIST data base[1] (Abel et al. 2005). Chemical fractionation is not included in UMIST, so we cannot now deal with molecular isotopes. The UMIST data base does not include information about the internal structure of molecules. Therefore, we can only compute the molecular space density and derive column densities for this full set of molecules. Here we compare results for the subset of

[1] www.udfa.net

molecules which we consider most reliable and for which observations are available. Figure 1.7 shows this comparison as a function of projected distance from the IF for $CO^+$, CN, $SO^+$, SO, CS and SiO. Our models directly predict the volume density of each molecule. We have then computed a predicted column density $N_j(r)$ at an angular offset $r$ arcsec from the IF using

$$N_j(r) = h \times n_j(r) cm^{-2} \tag{4}$$

where $h$ is the depth into the cloud along our line of sight. From §3.2 $h$ is found to be 0.115 pc. The number density from the model is $n_j$ for the $j^{th}$ molecule.

In most cases observations of diatomic molecules are presented as column densities. In cases where the observed surface brightness is the quantity reported, we have converted it into a column density using the assumption that the line is optically thin and the energy levels of the molecule are in LTE. Under these assumptions the relation between column density $N_T$ and surface brightness $\langle I \rangle$ averaged over frequency $\nu$ is given by Miao et al. (1995)

$$N_T = \frac{2.04\langle I \rangle}{\theta_a \theta_b}\left[\frac{B(T_{rot})}{B(T_{rot}) - I_{back}}\right]\frac{S_f Q_{rot} \exp\left(\frac{E_u}{T_{rot}}\right)}{g_l g_k S \mu^2 \nu^3} \times 10^{20} cm^{-2} \tag{5}$$

where $Q_{rot}=2kT_{rot}/h\nu$, and $B(T_{rot})$ is the Plank function at a temperature $T_{rot}$ with $I_{back}$ equal to the background continuum. In the analysis done by Young Owl et al. (2000) the conversion from $I$ to $N$ assumed that $T_{rot}$ = $T_{kin}$ = 100K, a value similar to the CR enhanced model. This is approximately the observed temperature of the $^{12}CO$ gas. When it is not possible to derive $T_{rot}$, $T_{kin}$ is often used. This underestimates the true column density if the line is subthermally populated as occurs when the gas density is below the critical density of the line.

Figure 1.7a shows the $CO^+$ comparison. Storzer et al. (1995) and Fuente et al. (2003) both measured $N(CO^+)$ as a function of depth into the Bar along the same line of sight as the other molecules measured by Tielens et al. (1993) and Tauber et al. (1994). The $CO^+$ observations are

characterized by a rise in column density with distance from the IF reaching a peak column density of $3\times 10^{12}$ cm$^{-2}$ at $r$ =17±7". After the peak a gradual decrease is observed out to a distance of 40" where $N(CO^+) = 4.8\times 10^{11}$ cm$^{-2}$. The column densities found by Storzer et al. are uncertain and may actually be higher based on uncertainties in the excitation mechanism assumed in the analysis, as explained in their paper. The $CO^+$ column density computed using the magnetic model with the canonical cosmic ray ionization rate peaks too early and is a factor 100 too low. With increasing cosmic ray ionization rate the peak column density increases and moves farther from the IF. For the enhanced cosmic ray model the peak column density is $4.85\times 10^{12}$ cm$^{-2}$ and occurs at $r$ = 12". The subsequent decrease in the modeled $N(CO^+)$ follows the observations very closely. $CO^+$ is shown to be very sensitive to the presence of cosmic rays. Decreasing the ionization rate by a factor of 10 decreases the column density by a factor of 100 at $r \geq 20$". We conclude that the enhanced cosmic ray model is in good agreement with the observed $CO^+$ column densities.

The CN column density (Fig. 1.7b) of our enhanced cosmic ray model is equal to the observed value of $1\times 10^{14}$ cm$^{-2}$ at 20" (Simon et al. 1997), and is 5 times higher than the observed value of $2\times 10^{14}$ at $r$ = 30". These are decreased to 0.5 and 3.75, respectively, if we adopt a gas phase C abundance of 30 percent of the solar value (Jansen et al. 1995). In contrast our magnetic model underpredicts CN by more than a factor of 10 at 20" and by a factor of 3 at r = 30". We consider our enhanced model to match the CN observations to an acceptable level, given that the uncertainties in the molecular data result in uncertainties of up to an order of magnitude in the absolute chemical abundance of species like CN (Simon et al. 1997).

The $SO^+$ column density (Fig. 1.7c) is observed to steadily increase with distance from the IF reaching $8.4\times 10^{12}$ cm$^{-2}$ (Fuente et al. 2003) at $r$ = 28". The computed column densities for the cases including the magnetic field without and with enhanced cosmic rays rise steeply at around

$r$ = 20" to 3.4× $10^{9}$ $cm^{-2}$ and 1.1x$10^{13}$ $cm^{-2}$ respectively, followed by a nearly constant plateau. Our cosmic ray enhanced model reproduces the observed peak column density, although additional $SO^{+}$ emission is observed near the IF and may be due to the background molecular gas. The peak measured column densities of SO (Fig. 1.7d) are 6× $10^{14}$ $cm^{-2}$ at 28" (Jansen et al 1995). Taking beam dilution into account, this corresponds to a factor of 6 greater than the predicted value, which is reasonable agreement.

The observed column density of CS (Fig. 1.7e) is 5× $10^{13}$ $cm^{-2}$ at $r$ = 20" and increases to 5× $10^{14}$ $cm^{-2}$ at 30" (Simon et al. 1997). Hogerheijde et al. (1995) find $N$(CS) = 1.5× $10^{15}$ $cm^{-2}$ at 28" for a similar position. The profiles of our magnetic model and enhanced cosmic ray model have nearly the same value as the observations at $r$ = 20", however these profiles are not convolved with the resolution of the observations which is very important in this case due to the rapid rise in the enhanced cosmic ray model at that point. If the resolution were taken into account, the enhanced cosmic ray model would have a column density ~2× $10^{15}$ $cm^{-2}$ or 40 times the observed value, while the magnetic model would match the observed column density to within a factor of 2. At 30" the situation is the same with the enhanced cosmic ray model overpredicting CS by a factor of 40. These conclusions are tenuous given the large range in assumed S abundance relative to H present in the literature. For example Jansen et al. (1995) and Simon et al. (1997) found the gas phase S abundance relative to H to be 2× $10^{-7}$, while Young Owl et al. (2000) assumed 7.9× $10^{-6}$. If S/H in the PDR is changed to 2× $10^{-7}$, the abundance assumed by Simon et al. (1997), our modeled N(CS) would drop to 1.25× $10^{15}$ at $r$ = 28", which is 0.83 times the observed value. Thus the CS column density taken by itself could easily be adjusted to fit the observations. However if the lower abundance of S that reproduces CS is used, the predicted SO and $SO^{+}$ become many orders of magnitude too faint. Therefore, the predicted ratio of CS to SO and $SO^{+}$ does not match the observations.

SiO observations (Fig. 1.7f) are available for three areas across the Bar (Schilke et al. 2001). The observations along their cut labeled "Bar-CO" lie in the same region of the Bar that we are studying. However, the exact location of the observations is unimportant because the measurements are statistically consistent with a constant value near $2\times 10^{12}$ cm$^{-2}$ (Schilke et al. 2001). All of our models are in disagreement with this result. Our enhanced cosmic ray model predicts a column density equal to $1\times 10^{13}$ cm$^{-2}$, a factor of 5 larger than observed at depths between 10" & 20". Then $N$(SiO) sharply increases to $4\times 10^{14}$ cm$^{-2}$. Any decrease in the cosmic ray density by a factor greater than 10 results in an underprediction of SiO for depth shallower than 20", but even with the canonical Galactic value used in the magnetic model, there is an overprediction by at least an order of magnitude at depth greater than 25". There are two explanations that may account for the discrepancy. First the gas phase Si abundance is likely to be depleted by at least an order of magnitude in the PDR compared with the ionized $H^+$ region (Schilke et al 2001). However the rate of depletion would have to be matched in such a way as to maintain a constant gas phase Si density with depth. The second possibility is that the emission is from an outflow in the foreground, although the velocity profiles suggest this is not the case (Schilke et al. 2001)

We conclude that for 4 of the 6 diatomic molecules shown, the addition of cosmic rays brings our model into general agreement (within a factor of 6) with the observations. For CS, our "magnetic model" agrees well with the observations and the further inclusion of enhanced cosmic ray heating hurts the agreement, but this depends on the fraction of S depleted onto grains in the molecular region. For SiO, none of our models agree with the observations. We stress that we did not use the molecular column densities discussed in this subsection as constraints when we fit our models to the observations. Rather, we are using them as *ex post facto* tests of how well our simulations of the inter-clump medium reproduce a wider body of data. We should also again

mention that we did not do a formal calculation of the predicted emission from these molecules. Some transitions, of $CO^+$ for example, may be significantly sub-thermally populated and would therefore produce little emission and would have to be attributed to unmodeled clumps. Still Simon et al. (1997) found that the CN and CS emission could be characterized by a diffuse gas with a density of 1-4x$10^5$ $cm^{-3}$ despite the critical densities of CN N=3→2 and CS J=7→6 being 9x$10^6$$cm^{-3}$ and 3x$10^7$ $cm^{-3}$, respectively. This is comparable to our peak density of 9x$10^4$ $cm^{-3}$. While some moderately complex molecules are included in the UMIST database and therefore in our computations, the predictions for anything more complex than diatomic molecules are highly uncertain. There are two sources of uncertainty. The first is in the rate coefficients for the many processes that lead to the formation or destruction of a species. The systematic errors in the rates are not possible to quantify. The second systematic uncertainty is in the assumptions that go into creating an equilibrium model. The comparisons presented in Röllig et al. (2007) between models computed with different codes show nearly an order of magnitude scatter in the computed number densities of these complex molecules even in cases where all models used the same fixed gas kinetic temperature and an agreed upon subset of the UMIST data set. The scatter between actual thermal equilibrium models was far worse. Because of the resulting large uncertainty in the computed column densities of these complex molecules, we will not consider them further.

**4.3 Sensitivity of final model to input parameters**

*Q(H).* During the course of this investigation, we explored the parameter space $10^{49.00} \leq Q(\mathrm{H}) \leq 10^{49.23}$ $s^{-1}$, and distance to the nebula $437 \leq d \leq 500$ pc. We could always find a placement and tilt of the Bar that would provide a good fit to the observations. It was always the case that the $H^+$ region could be described by a version of the gas pressure model, but that magnetic pressure support and cosmic ray heating were needed to also match the $H^0$ region properties. Specifically we found no combination of parameters that produced a gas pressure model in which the $H_2$

emission was displaced from the ionization front by the observed distance, nor in which the observed peak $H_2$ intensity was reproduced.

*Distance.* If the distance to the nebula were in fact 500 pc (the distance adopted by Wen & O'Dell 1995 and many other authors), $\langle B \rangle$ would be affected in two ways. The projected distance of the $H_2$ emission from the IF increases from 0.021 pc to 0.024 pc. To match the larger offset a higher value of $P_{mag}/P_{gas}$ is required, with a nonlinear relation between the offset distance and $\langle B \rangle$. Countering this effect, the inferred radiation pressure responsible for compressing the magnetic field also would drop, since $\theta^1$ Ori C would have to be farther away from the illuminated face. The average magnetic field in the $H^0$ region from Paper I, eq. 7 has $\langle B \rangle \propto 1/R$, where $R$ is the distance to the IF. For a distance of 500 pc, $\langle B \rangle$ is expected to decrease by 12 per cent. The combination of these two effects was calculated for the magnetic model without enhanced cosmic rays. The magnetic field dropped from 448μG to 435 μG.

*Inclination.* If the Bar is inclined by more than the 7 deg angle assumed here, the observed offsets would require a greater radial distance between the observed emission peaks and $\theta^1$ Ori C. Take for example a model with a calculated radial separation $\Delta x$ between two emission peaks. For a tilt angle $\phi$, the projected separation on the sky is $\Delta x' = \Delta x \cos\phi$. For increased values of $\phi$, the modeled radial separation must increase. This increased radial separation would in turn imply a lower density $H^0$ region, so that a higher magnetic field would be required to maintain hydrostatic equilibrium. The effect at 7 deg is less than 1 percent. Therefore our models with magnetic fields represent the lower limit for $\langle B \rangle$ in the Bar when considering the geometry.

*Density and scattered Hα light.* The [S II] ratio found in our model is 0.05 lower than the observed value, within the 15% uncertainty in the collision rate (AGN3). Wen & O'Dell (1995) estimate that 1/3 of the surface brightness of Hα and other optical emission lines is due to light reflected from dust in the molecular cloud, which we have included in our current computed

results. If this is wrong and scattered light is not such a large effect, we could compensate by making the slab somewhat larger along the line of sight.

*Turbulence.* We have considered turbulence in two ways. For all of the models presented here the turbulence was fixed to be 2 km $s^{-1}$ FWHM, consistent with observations of $H_2$ and $^{12}CO$ lines. This turbulence was counted as part of the total pressure. Another approach possible in any model with a magnetic field is to assume that $P_{mag} = P_{turb}$, motivated by equipartition arguments. In that case the turbulent velocity would vary as a function of depth and would be about 3 km $s^{-1}$ in the molecular gas. The associated increase in $P_{turb}$ then would lead to a lower magnetic field. In the enhanced cosmic ray model, the final derived cosmic ray density is in equipartition with the magnetic field, so the density of cosmic rays would also decrease. We rule out this type of model for two reasons: (1) the $^{12}CO$ emission would peak 10 arcsec farther from the ionization front than is observed; and (2) the molecular gas temperature is predicted to be only 70 K , at least 20 K colder than the observed temperature of the Bar. The offset is geometry dependent, while the temperature is not.

**4.4 Magnetostatic equilibrium**

Each of the three models assumes hydrostatic equilibrium. The left-hand column of Fig. 1.4 shows how the various pressure components from Eq. A2 adjust themselves to maintain this condition. As was discussed in detail in Paper I, the integrated radiation pressure from absorbed starlight steadily builds up with depth until all of the incoming photons have been used up at the bottom of the $H^0$ region. The sum of the other pressure terms must steadily rise to balance this. It is clear from Fig. 1.4 that in each model there is a large residual gas pressure at the illuminated face of the cloud (depth = 0). This has to happen in these models because they describe the cloud as suddenly beginning with some gas density and temperature. The $H^+$, $H^0$ and $H_2$ regions are actually a flow from cold molecular gas through the atomic region into hot and ionized gas with

the ionizing radiation gradually eating into the molecular cloud. For the case of M17 (Paper I) we found that the residual pressure at the cloud face actually is in equilibrium with the hot bubble of X-ray emitting gas that is observed to surround the ionizing stars. A similar bubble of diffuse X-ray emitting gas has recently been found to the SW of the Bar region, although the close proximity to $\theta^1$ Ori C and foreground absorption by the Veil blocks a direct view of the Bar in diffuse X-ray emission (Güdel et al. 2008). The estimated pressure from the X-Ray emitting gas was found to be roughly equal to the gas pressure of the $H^+$ region. The observed champagne flow and pressure equilibrium suggest the bubble is a leaky cavity (Güdel et al. 2008).

Our final enhanced cosmic ray model should be a realistic simulation of the Bar for a snapshot in time. The key feature is that at the same time that the radiation field from $\theta^1$ Ori C is dissociating and then ionizing the original molecular gas, the momentum carried by the photons has pushed the gas back into the molecular cloud, compressing both the gas and any magnetic field that is frozen into it. The natural and straight-forward result is that this compression is halted when the combination of gas, turbulent, and magnetic pressure has risen enough to offset the radiation pressure, so the system is in "magnetostatic equilibrium". The current quasi-equilibrium situation in the Orion Bar might represent an extrapolation of the situation described in recent MHD models (Krumholz et al. 2007) of the effects of magnetic fields on the early stages of expansion of an H II region.

**4.5 Heating mechanisms**

Figure 1.8 shows the relative contribution of each important heating mechanism for each of the three models. Cosmic ray heating is a minor effect in the gas pressure and magnetic field models, but in the enhanced cosmic ray model it completely dominates the heating beyond a depth of about 0.2 pc, which is well into the molecular ($H_2$) region. Cosmic ray heating accounts for 80 percent of the total heating in this region, while the remaining 20 percent is due to cosmic ray

excitation of permitted FUV lines. We note that cosmic ray heating is generally thought to be responsible for heating molecular clouds (Lequeux 2005).

**4. 6 Comparison to previous models of the Bar**

*Geometry.* Almost all previous models of the Orion Bar PDR agree that the observed stratified $H^+$, PAH and $H_2$ emission must come from a diffuse gas with density 1–5x$10^4$ $cm^{-3}$, rather than from the superposition of many small optically thick clumps ( i.e. Tielens et al (1993); Tauber et al. (1994); Hogerheijde et al. (1995); Young Owl et al (2000)). The pressure of this gas is of the same order as the gas pressure at the IF inferred from the ratio of [S II] λ6716/λ6731. The geometry of the homogenous region can be estimated from the use of optically thin emission lines. With estimates of the emissivity per unit volume we have used [S II] λ6716+λ6731 to find the depth of the bar to be 0.115pc. Estimates using [O I] λ6300 and FIR continuum measurements from 20μm to 100μm lead to a similar conclusion. Since these are observations of a region close to the IF, they only directly trace the geometry at the narrow $H^+/H^0$ transition.

A more complete, 3-dimensional model of the IF over the entire nebula was constructed by Wen & O'Dell (1995), working backwards from the observed Hα surface brightness and projected positions. Their work indicated that the Bar is an upward corrugation of the main IF, which is the basic geometry that we have adopted here. We initially attempted to rather closely follow their result by describing the Bar as a surface steadily curving upward towards the observer, with $\theta^1$ Ori C at the center of curvature. We also experimented with a slab inclined at 20 deg to our line of sight, which is the tilt of the layer in the Wen & O'Dell models. In neither case were we able to reproduce the observed [S II] brightness profile and intensity simultaneously. It should be noted that Wen & O'Dell warned in their paper that their model was not expected to be very accurate in the region of the Bar. These problems led us to switch to the more nearly edge-on slab geometry described above. However, our model is still generally consistent with the basic Wen & O'Dell

picture, especially if the Bar is connected to the background cloud in the way sketched in Fig. 1.3. We note that the computed $H_2$ profile shown in Figure 1.5 is narrower than the observed one, which suggests that the $H^0$ region in the Bar does have a more complicated geometry (curvature or corrugations) than we have assumed here, as Wen & O'Dell suggested. Note that the separation between $\theta^1$ Ori C and the ionization front immediately behind it is fixed by $Q$(H) and the H$\alpha$ surface brightness to be 0.183 pc (this is different than the value found by Wen & O'Dell because we have adopted a different distance to the Orion Nebula, which changes $Q$(H)). Hogerheijde et al. (1995) showed that the molecular gas also has a geometry that changes from face-on to edge-on (the Bar) and then back to face-on. Figure 13 of their paper illustrates the PDR geometry derived from $C^{18}O$. They assumed a constant abundance ratio $H_2/C^{18}O = 5\times 10^6$ and $n(H_2) = 5\times 10^5$ cm$^{-3}$ to estimate the volume density of $C^{18}O$. Using the measured column density of $C^{18}O = 1.3\times 10^{16}$ cm$^{-2}$, the line of sight path length would be 0.6 pc. Applying our more detailed calculations and assuming $CO/C^{18}O \sim 500$ (Wilson & Rood 1994) our enhanced cosmic ray model predicts $N(C^{18}O) = 1.25\times 10^{16}$ cm$^{-2}$, in good agreement with Hogerheijde et al. (1995). However the path length came out to be 0.115 pc, which is smaller than the one found by Hogerheijde et al. but is in good agreement with the path length derived above from the [S II] lines. In contrast our magnetic model has a predicted $N(C^{18}O) = 2.2\times 10^{16}$ cm$^{-2}$ which would require the geometry to decrease in size by almost a factor of 2 between regions in the PDR. The similarities of the geometry between the $H^+$ region, IF and PDR therefore support our enhanced cosmic ray model.

*Interclump Region.* Our final model largely reproduces the interclump densities used by Tielens et al (1993), Tauber et al. (1994) and Young Owl et al (2000) to model the $H^0$ region. This is a factor of 5 greater than the interclump medium density proposed by van der Werf et al. (1996). The main difference in our work is in the starting point of the calculation. Previously, the

observed offsets between the emission line peaks were used to establish the $H^0$ region density. Having assumed a $H^0$ region temperature of 1000 K and a constant density, Tielens et al. (1993), Tauber et al. (1994) and Young Owl et al (2000) argued that the $H^0$ region gas density was consistent with the ionized gas density for a system with gas pressure equilibrium across the IF. It is this assumption that our calculations treat in detail by including not only gas and turbulent pressure but also a pressure gradient caused by absorbed starlight. Starting from the assumption of hydrostatic equilibrium we constrained our models to match the observed properties of the $H^+$ region of the Bar. Our model using only gas pressure did not correctly describe the density and geometry of the $H^0$ region. We then added a magnetic field whose pressure is also in hydrostatic equilibrium, and the $H^0$ region density deduced by Tielens et al. then came out as a natural result. Our models are most similar to those presented by A05 who considered a constant pressure model with an equation of state that determines the density as a function of depth, as we have, as opposed to using a constant density. Unlike van der Werf et al. (1996) for example, A05 used a single-component medium with a filling factor of unity for the $H_2$ emitting region. This was motivated by a lack of unambiguous evidence that clumping is important in the $H_2$ emitting region. A pressure of $P/k = 8 \times 10^7$ cm$^{-3}$ K was derived from the electron density and temperature at the IF. This is the same total pressure found in our models significantly beyond the IF. However, the spot measured by A05 has a higher surface brightness than the interclump region we have modeled here. Paper III shows that their $H_2$ measurements are matched by the enhanced cosmic ray model as described here but with a factor two increase in peak $H_2$ density. The detailed study by A05 determined that a source of extra heating was required to reproduce the observed level populations of $H_2$ as well as the 100-120 K temperatures where other molecules form. They were unable to determine a realistic heating mechanism to account for this, concluding that "future modeling must address the high temperatures in the CO/$HCO^+$/$NH_3$ zone

of the Orion Bar." In this paper we propose enhanced cosmic ray heating as a major source of that extra heating and present the effects of such a high cosmic ray ionization rate on the chemistry of the Bar.

*Clumping.* Tielens et al. (1993), Tauber et al. (1994) , Young-Owl et. al, (2000), van der Werf et al. (1996) and many others have also considered the effects of small (< 1 arcsec) and large scale (5–10 arcsec) regions of higher density (clumps). Clumping is directly observed in maps made in molecular lines from optically thing high levels, such as $^{12}$CO J(14-13) as well as H$^{13}$CN (Lis & Schilke 2003). We have not attempted to address this sub-structure in our model.

The Tielens et al. (1993) model for the inter-clump gas component which dominated most of the observed emission lines under-predicted the strengths of the CO (7–6) and (14–13) lines by a large factor, so these lines were attributed to emission from clumps. Our final model does in fact reproduce the observed $^{12}$CO (7–6) line strength (as well as $^{12}$CO (1–0)) to within a factor of two (Table 1.1). However, we under-predict the J = 14-13 line by a factor of 4, and clumps clearly are visible on direct images taken in this line (e.g. Young Owl et al. 2000), so they likely are significantly affecting the strengths of the higher-level molecular lines. We conclude in general agreement with all the previously mentioned studies except van der Werf et al. (1996) that the UV penetration responsible for the observed stratification in the Orion Bar is dominated by a roughly homogeneous inter-clump medium, with filling factor close to unity. In our view the density concentrations comprising the clumps are just details on top of this.

Van der Werf et al. (1996) arrived at a model that had a rather lower density interclump medium ($n(H_2) = 1\times10^4$ cm$^{-3}$) in combination with clumps characterized by two different densities. A high density component with $n(H_2) \sim 10^6$ cm$^{-3}$ was deduced from photochemical models in which high densities are necessary to effectively produce hot $HCO^+$ and $CO^+$. The $^{13}$CO J = 3-2 brightness temperatures of 40 to 50K are typically only reached in PDRs with densities of at least

$10^6$ cm$^{-3}$. However, the observed CS line ratios indicate a lower-density clump component with $n(H_2) = 2.5\times 10^5$ cm$^{-3}$. Our model overpredicts the CS column density (Fig. 1.7e) that is derived from the observed surface brightness assuming LTE and a constant gas phase S abundance from the $H^+$ region through the PDR. However, if the space density of $H_2$ is lower than the critical density of a few times $10^5$ cm$^{-3}$, the levels will be subthermally populated and the column densities deduced from the observed CS surface brightness assuming LTE will be too small. Our derived $n(H_2) = 4.6\times 10^4$ cm$^{-3}$ is significantly below the critical density of CS so we conclude that the reported column densities are a lower limit. Likewise if the gas phase S abundance were lowered in the PDR our predicted CS column density would be lowered.

Neglecting clumps in our treatment is unlikely to affect our conclusions regarding the presence of a magnetic field for two reasons. First, every paper about clumps (except van der Werf et al. 1996) find the clumps to have a low filling factor (*i.e.* 0.3% clump filling factor according to Hogerheijde et al. 1995) so that they do not strongly affect the transport of the UV light responsible for the overall structure of the $H_2$ emission. Second, the studies that include clumps such as that of Young Owl et al. (2000) do not require a clumpy ridge to match the HCN and $HCO^+$ until depths greater than 20" are reached, significantly beyond the peak $H_2$ emission. Even a clumped medium does not offer a perfect explanation of the emission at this depth. As Young Owl et al. (2000) noted, significant differences in the HCN and $HCO^+$ surface brightness distributions indicates that localized variations in the production mechanisms for HCN and destruction mechanisms for $HCO^+$ are required. These may be explained by density enhancements caused by local variations in the magnetic field.

**4.7 Is enhanced cosmic ray heating a realistic prospect?**

Our best-fitting model is for the case where the cosmic ray energy density is in equipartition with the magnetic field's energy density. Equipartition occurs in the local ISM (Webber 1998) where

B ~ 8μG and the energy density of cosmic rays is ~1.8eV $cm^{-3}$, although we do not know of any first-principle physical reason why this must occur. Still, the idea of equipartition has been used to argue for the existence of a high cosmic ray energy density in the Arches cluster near the galactic center (Yusef-Zadeh et al. 2007), with an energy density of $6\times 10^4$ eV $cm^{-3}$. This is an order of magnitude larger than what we are suggesting here. In the Sagittarius B region the cosmic rays are thought to be enhanced by a factor of 10 over the Galactic background (van der Tak et al. 2006).

Gamma ray observations provide a limit to the cosmic ray ionization rate (Ramaty 1996). A preliminary analysis of COMPTEL satellite observations (Bloemen et al. 1994) suggested a very high gamma ray flux. Although Bloemen et al. (1999) revised this to a $2\sigma$ upper limit three times lower than the originally-claimed detection, Giammanco & Beckman (2005) used the preliminary value to find a cosmic ray ionization rate of $2\text{–}7\times 10^{-13}$ $s^{-1}$, depending on the cloud mass. We rescaled their result to the revised measurement to find a $3\sigma$ upper limit on the cosmic ray ionization rate of $3\times 10^{-13}$ $s^{-1}$ for $H_2$, as compared to our predicted value of $2\times 10^{-13}$ $s^{-1}$. Thus the predicted gamma-ray flux from our enhanced cosmic ray model is consistent with the upper limit detected by COMPTEL.

These high energy particles in the presence of magnetic fields also produce synchrotron radiation, so we next examine whether they are ruled out by radio continuum observations. The total power emitted per unit volume for a power law distribution of particles is, from chapter 6 of Rybicki and Lightman (2004),

$$\epsilon_{Total}(\nu)=\frac{\sqrt{3}q^3 C B\sin\alpha}{mc^2(p+1)}\times\Gamma\left(\frac{p}{4}+\frac{19}{12}\right)\times\Gamma\left(\frac{p}{4}-\frac{1}{12}\right)\times\left(\frac{2\pi mc\nu}{3qB\sin\alpha}\right)^{\frac{(p-1)}{2}} \qquad (6)$$

where $B$ is the strength of the magnetic field, m the electron mass, $c$ the speed of light, and $\alpha$ is the angle between the electron velocities and the magnetic field. $C$ and $p$ parameterize the distribution of the volume density of relativistic electrons $n_{CR}$ as a function of energy E

$$n_{CR}=C\times E^{-p} \tag{7}$$

where $p \sim 2.4$ as measured from the spectra of radio-loud active galaxies (Kellerman 1966) and $C$ is a normalization constant. We have assumed an initially tangled magnetic field. If the field were still tangled the synchrotron emission would be isotropic. However the field would become less tangled as it is swept up with the gas. This will result in beaming that could increase or decrease the observed flux depending on the exact orientation of the magnetic field relative to our line of sight. If to first order, we assume the radiation will still be fairly isotropic, the predicted surface brightness due to 20 cm synchrotron emission from the PDR for our enhanced cosmic ray model is

$$S_{sync}=\frac{\epsilon}{4\pi}\times L=1.08\times 10^{-27} erg\, s^{-1} cm^{-2}\, arcsec^{-2} Hz^{-1} \quad . \tag{8}$$

Continuum measurements have been made of the Orion Nebula using both single dish and interferometric radio telescopes at 20 and 2cm (Felli et al 1993). The single dish measurements provide a total flux but do not have adequate angular resolution to resolve the Bar. Interferometric observations using the VLA C and D configurations with a beam size of 28" show that the observed surface brightness at the same position in the Bar is $1.35\times 10^{-26}$ erg $s^{-1}$ $cm^{-2}$ $arcsec^{-2}$ $Hz^{-1}$ at 20cm. This is a lower limit to the true flux because the total interferometric observation contains only 60 percent of the single dish flux. Assuming that this lower limit is the true value, the predicted synchrotron radiation is 8% of the observed value and therefore is consistent with the observations. The observed flux is dominated by thermal emission.

A further question is how long an enhanced rate of cosmic ray heating could go on for, even if the cosmic ray density does become large at some point in time. With no inflow of new cosmic rays, the rate at which cosmic rays heat the gas is the same as the rate at which the overall cosmic ray energy density is decreasing, and this can be used to determine a time scale. An analytical form of the cosmic ray heating rate can be found in Tielens & Hollenbach (1985). Assuming that the cosmic rays are trapped in the cloud by a tangled magnetic field, we can then define the lifetime of a high-energy cosmic ray by

$$\tau_{CR} = U_{CR} / \Gamma_{CR} \qquad (9)$$

where $U_{CR}$ is the energy density of cosmic rays and $\Gamma_{CR}$ is the heating rate from Tielens and Hollenbach. This lifetime depends on the $H_2$ and $H^0$ density, but is independent of the cosmic ray density. For the gas density $n_H = 4.6\times 10^5$ cm$^{-3}$ which exists in the appropriate zone of our best model, the cosmic ray lifetime is only 2000 years. This short lifetime applies to all PDRs with similar densities. The transport of cosmic rays through a magnetized partially ionized medium is a rich and complex problem with no easy solutions (see, for example, Lazarian & Beresnyak 2006; Snodin et al. 2006). The details of their motion depend on the field geometry, which is unknown in this region of Orion. However, the timescale problem we have pointed out is shared by most models of the neutral and molecular regions. The short timescale is a consequence of the hydrogen density and not the cosmic ray density.

We have shown that an enhanced cosmic ray density can account for the observed properties of the Bar. Enhanced cosmic rays will result from compression of magnetic field lines. If the field is well ordered and connected to the diffuse ISM the cosmic rays will leak out at nearly the speed of light and the CR density quickly will go back to the background value. If field lines are tangled, as assumed in our work, the CRs will be trapped and lose their energy through collisional processes. This is clearly a crucial issue. Recent studies (Indriolo et al. 2007) have shown that the

cosmic ray ionization rate varies widely along various sight lines through the diffuse ISM with a maximum value over 1 dex larger than the accepted background value. Clearly the picture of a single Galactic cosmic ray background with ordered fields sustaining this rate is an oversimplification.

**4.8 Comparison to the magnetic field in other PDRs**

The other star forming region where this type of analysis has been performed is M17 (Paper I). The edge-on ionization front in M17 has a considerably lower gas density than does the Orion Bar (the [S II] ratio indicates $n_e$ ~560 $cm^{-3}$ in M17, as compared to $n_e$ ~3200 $cm^{-3}$ in the Orion Bar). At the same time, the magnetic fields are measured to be roughly equal in the two $H^0$ regions. This means that the ratio $P_{mag}/P_{gas}$ is much larger in M17, so that the magnetic field has a much larger (and hence more noticeable) effect. Paper I showed that the magnetic field produces a very large increase in the extent of the $H^0$ region in M17, as is observed. In the case of the Orion Bar, $P_{mag}/P_{gas} \sim 1$ in the $H^0$ region (Fig. 1.4) so the $H^0$ region size is increased by only about a factor of two. In addition, while the magnetic pressure also affects the region where the [S II] doublet is formed in M17, this does not really happen in Orion. None-the-less, the magnetic pressure does change the overall structure of the Orion Bar by a significant amount, and so should be included in models of it.

At a depth greater than 0.15pc into the cloud our best model predicts most hydrogen is molecular and has a density $n(H_2)=10^{4.66}$ $cm^{-3}$, and a magnetic field of 543μG. Crutcher (1999) has combined most of the available direct measurements of $|B_{los}|$ for a number of systems, including molecular cores and star forming regions such as M17, along with estimates of $n(H_2)$. Figure 1.9 has been adapted from Figure 1 of Crutcher (1999) to include our point for the Orion Bar. The filled circles are measured points for other systems, while the triangles represent systems for which only an upper limit on $B_{los}$ is available. The Orion point is consistent with the general

trend, showing that the magnetic field strength that we have deduced for the Bar is in line with the values found in the cases where direct measurements are possible.

**4.9 The effect of radiation pressure on gas density**

In the simplest case, the Bar is an edge-on ionization front where the observed increase in surface brightness can be attributed to the depth along the line of sight. However, this cannot be the whole story. The maps of the measured [S II] λ6716/λ6731 ratio shown by both Pogge et al. (1992) and García-Díaz & Henney (2007) show that the Bar is also a density enhancement over the regions to either side of it. We suggest that this increase in density is due to the Bar being more face-on to the light from $\theta^1$ Ori C than is the surrounding ionized cloud face, so that radiation pressure due to starlight is greater in the Bar. To illustrate this, we perturbed the momentum (as set by $\Phi(\mathrm{H}) \propto Q(\mathrm{H})$) at the illuminated face upwards and downwards by a factor of 2. Figure 1.10 shows that the density at the ionization front responds roughly according to $n_H \propto \Phi(\mathrm{H})$, indicating that in the $\mathrm{H}^+$ zone the momentum $p \propto \Phi(\mathrm{H})$ is balanced by gas pressure. This effect, the changing flux of momentum in the ionizing radiation field, may be what drives the density variations across many H II regions. It appears to occur over the Orion Nebula as a whole. For example, in a strip reaching radially to the W of $\theta^1$ Ori C that is covered by the long-slit spectrum of BFM91, the electron density falls off steadily as a function of the distance $r$ from $\theta^1$ Ori C approximately as $n_e \propto r^{-1.7}$ (see their Fig. 7), consistent with the dilution of the incident momentum entering the cloud per unit area along this strip. Wen & O'Dell (1995) find $n \propto r^{-1.63}$ from a more comprehensive plot of $n_e$ vs. $r$ covering the two-dimensional face of the Orion Nebula (their Fig. 6). While this is not quite as rapid a falloff as the expected $r^{-2} \cos(\theta)$ dependence (where $\theta$ is the angle at which the ionizing radiation strikes the IF), it certainly suggests that the decrease in momentum flux is an important factor. Radially decreasing density gradients also are found in a number of additional H II regions, both Galactic (Copetti et al. 2000)

and extragalactic (Castañeda et al. 1992). These may be other cases in which the ionization front forms a background sheet behind the ionizing star(s), similar to the situation in Orion.

**5. Conclusions**

We simultaneously modeled the Orion Bar's $H^+$ and PDR regions in order to find out which physical processes are important in determining the overall structure. We assumed that the Bar is in hydrostatic equilibrium throughout; while not likely to be strictly true, this should be a fair approximation. We compared models that include a magnetic field that is well-coupled to the gas to models without magnetic fields and developed a final best-fitting model that includes both magnetic fields and an enhanced cosmic ray density.

Our final model reproduces the observed surface brightness profiles, in the sense of both their position and the actual brightness, of the Hα, [S II], $H_2$ and $^{12}CO$ emission lines and also the [S II] λ6716/λ6731 ratio, and the strengths of [O III], [N II], [O I], [Si II], [C II] and additional CO emission lines. This is achieved by varying the location of the illuminated face and the gas density at the face, the tilt of the IF and its depth along the line of sight, the magnetic field strength, and the cosmic ray density. These emission lines come from what are really three very different regions (ionized, atomic and molecular) associated with star formation. Self consistently modeling all the zones together provides us with additional constraints that are not available when treating either the $H^+$ or the combined $H^0$ and molecular zones as independent entities.

We find that in the case of the Bar, magnetic pressure plays an important role in the $H^0$ region, providing about half of the total pressure support. The evidence for this is the offset of the $H_2$ emission peak from the position of the ionization front as marked by the [S II] emission peak, which is mostly a measurement of the gas density in the $H^0$ region. Since in hydrodynamic equilibrium the magnetic pressure offsets some of the need for gas pressure, the result is a lower gas density. For this model we find $\langle B \rangle = 438\mu G$ in the $H^0$ region.

The above model still did not provide a very good fit to the location and brightness of the $^{12}CO$ J=1–0 emission peak, nor did it reproduce the extended $H_2$ emission reaching into the deeper regions of the cloud. We find that these features can be explained if there is an associated enhancement in the density of cosmic rays by the factor expected if the cosmic ray and magnetic field energy densities are in equipartition, with $\langle B \rangle = 516\mu G$ in the $H^0$ region and the cosmic ray density $10^{3.6}$ times higher than the Galactic background value. Although we don't know exactly how this equipartition would occur, and there may be problems about the timescales over which these cosmic rays lose their energy, this is the same situation that we found in M17. This suggests that an increase in the cosmic ray density may be a natural consequence of the compression of magnetic fields frozen into these gas clouds. We find that an enhanced abundance of cosmic rays in a diffuse inter-clump medium can explain the observed $CO^+$ surface brightness profile as well as the surface brightness profiles of a number of other molecules, although some molecular lines clearly do come from clumps.

We note that the initial magnetic field (before compression) needed to create such a scenario is very close to the average field for the Galaxy, suggesting that magnetic fields may be important in many similar regions of star formation. In both this current model of the Orion Bar and in our earlier model of M17, the basic concept is that the momentum carried by radiation and winds from the newly formed stars compresses the surrounding gas until enough pressure builds up inside the gas cloud to resist (i.e. until an approximate hydrostatic equilibrium is set up). If the gas starts out with a weak magnetic field, that field can be compressed along with the gas until magnetic pressure becomes an important factor and magnetostatic equilibrium is established. The enhancement of the cosmic ray density would then just be an additional side effect. We believe that this is a very straight-forward, cause-and-effect description of some of the key processes that shape the gas clouds that are found in star-forming regions of all sizes.

EWP and JAB gratefully acknowledge support from NSF grant AST-0305833. GJF thanks NSF for support through AST-0607028, NASA for support through NNG05GD81G and STScI for support through HST-AR-10653.

**Appendix A. The gas equation of state**

The equation of state is the relationship between the gas density and pressure. The terms we include in the equation of state are described here.

There are three broad classes of simulation codes that could be applied to a region such as the Orion molecular cloud. Hydrodynamics codes such as Zeus (Hayes et. al 2006) or Gadget (Springel 2005) will follow the gas dynamics in detail, often in three dimensions and sometimes with a treatment of the magnetic field. This class of codes generally does not do the atomic physics in detail but rather treats thermal and ionization processes with generalized fits to universal functions and neglect the radiative transfer. Radiative transfer codes such as ATLAS (Kurucz 2005) or Phoenix (Hauschildt et al. 1997) will do the radiative transfer with great care but at the expense of the atomic physics and dynamics. Finally, plasma simulation codes such as Cloudy, which we use in this paper, treat the atomic, molecular, and emission physics with great care but do the dynamics and radiative transfer with more approximate methods.

All three classes of codes are trying to do the same thing, a true simulation of what occurs in nature, but are limited by available computers and coding complexity. All are being improved in the areas in which they are weak but we are still many years away from being able to perform a true simulation of the spectral emission of a magnetized molecular cloud with an advancing ionization front.

In this paper we model the $H^+$ / $H^0$ / $H_2$ layers as a hydrostatic atmosphere. This is clearly a simplification – the layers are actually a flow from cold-molecular into hot-ionized regions. For a D-critical ionization front the ram pressure, the pressure term due to the motions of the gas, will equal the gas pressure once the gas has attained its full motion (Henney et al 2005b; Henney 2007). This term is not present in a static geometry, so the pressure we use may be off by as much as a term equal to the gas pressure. In most of the cloud the gas pressure is only a fraction

of the total pressure, which includes terms from turbulence, radiation pressure, and the magnetic field. The uncertainty introduced by the hydrostatic approximation is likely to be of the same order as uncertainties in the chemistry network or the grain properties.

We treat magnetic pressure as a scalar which is added to the gas and radiation pressures. This is formally correct if the field is highly disordered. For an ordered magnetic field the forces acting on a charged particle produce a directed motion rather than a scalar pressure term. We know that the magnetic field in the Veil, the atomic layer of gas in front on the Orion Nebula (Abel et al. 2005), is ordered since a disordered field would produce no net Zeeman polarization. The field strength and geometry across the Bar are unknown. The approach we take is simple but reasonable given the uncertainties and complexities.

The magnetic field is computed assuming flux freezing, that is, that the field and gas are well coupled. The field at any place in the cloud is related to the field at the illuminated face of the cloud by the ratio of densities. The gas density at the ionization front is in turn constrained by the observed [S II] I(λ6716)/I(λ6731) intensity ratio. As is explained in detail in Paper I, the magnetic field is assumed to scale with the gas density according to the relation

$$B = B_0 \times \left( \frac{n}{n_0} \right)^{\gamma/2} \quad . \tag{A1}$$

Here $B_0$ and $n_0$ are the magnetic field and the gas density at the illuminated face of the cloud and $\gamma$ depends on the geometry of the system. For spherical collapse $\gamma$ is 4/3 while $\gamma = 2$ describes the 2D compression of a shell. We choose $\gamma = 2$ on the assumption that the Bar is an edge-on section of the general shell of material which has been swept up and compressed by the radiation pressure from $\theta^1$ Ori C. This is similar to the situation in M17, for which this choice was justified in some detail in Paper I.

The total pressure $P_{tot}$ is then given by

$$P_{tot}(r) = nkT + \frac{B^2}{8\pi} + P_{turb} + P_{lines} + P_{stars}(r) \qquad \text{(A2)}$$

This is the equation of state assumed in BFM91, who ignored the magnetic and turbulent pressure terms. They called this a constant pressure model, and Cloudy continues to do so today, although hydrostatic is a better term. The first term in Eq. A2 is thermal gas pressure, the second is the magnetic pressure, $P_{turb}$ is the pressure from non-thermal turbulent motions, $P_{lines}$ is the radiation pressure due to trapped emission lines (mainly Ly$\alpha$), and $P_{stars}$ is the net pressure resulting from the absorption of starlight. This last term is given by

$$P_{stars}(r) = \int_{r_1}^{r} a_{rad}\, \rho\, dr \qquad \text{(A3)}$$

This is equal to zero at the illuminated face, where $r = r_1$, and then grows with depth, reaching its full value near the ionization front, where $r = R_H$. The total outward force is approximately given by the total momentum in ionizing radiation,

$$P_{stars} = \frac{Q(H_0)\langle h\nu \rangle}{4\pi R_H^2 c} \quad . \qquad \text{(A4)}$$

The local pressure is not actually constant, although there is no net force acting on the gas, since the $P_{stars}$ term increases with increasing depth. Paper I gives a more detailed description of these effects.

**Table 1.1**
**Observed and predicted quantities for the Orion Bar.**

| Quantity[1] | Observed (Ref[2]) | Gas Pressure | Magnetic | Enhanced Cosmic Rays |
|---|---|---|---|---|
| [S II] ratio | 0.62 | 0.59 | 0.59 | 0.59 |
| $S$([S II]λ6716+λ6731) | 5.7e-13 (1) | 5.6e-13 | 5.5e-13 | 5.6e-13 |
| $S$(Hα) | 6.6e-12 (2) | 6.5e-12 | 6.5e-12 | 6.5e-12 |
| $S$(O III) | 6.8e-12 (2) | 8.2 e-12 | 8.2e-12 | 8.2e-12 |
| $S$(N II) | 2.2e-12 (2) | 2.8e-12 | 2.7e-12 | 2.7e-12 |
| $S$($H_2$ 2.121μm) | 3.3e-15 (3) | 5.0e-15 | 3.3e-15 | 3.1e-15 |
| $S$($^{12}$CO J(1-0)) | 9.4e-18 (4) | 1.7e-17 | 8.0e-18 | 7.5e-18 |
| $S$($^{12}$CO J(7-6)) | 4.7e-15 (4) | 3.0e-15 | 4.3e-17 | 7.2e-15 |
| $S$($^{12}$CO(14-13)) | 7.1e-15 (4) | 2.0e-17 | 2.6e-21 | 2.6e-15 |
| $S$(OI 145μm) | 4.7e-14 (4) | ≤ 2.9e-13 | ≤ 1.3e-13 | ≤ 1.2e-13 |
| $S$(OI 63μm) | 9.4e-13 (4) | ≤ 4.4e-12 | ≤ 1.8 e-12 | ≤ 2.2e-12 |
| $S$(Si II 34μm) | 2.1e-13 (4) | 8.8e-13 | 3.7e-13 | 3.9e-13 |
| $S$(CII 158 μm) | 1.2e-13 (4) | 2.4e-13 | 1.2e-13 | 1.2e-13 |
| $\langle B \rangle$ μG[3] | Unknown | 0μG | 438μG | 516μG |

[1] Peak surface brightness $S$ is in erg $s^{-1}$ $cm^{-2}$ arcsec $^{-2}$.

[2] References for peak surface brightness: (1) new SOAR observations; (2) Wen and O'Dell 1995; (3) Young Owl et al. 2000; and (4) Tauber et al. 1994.

[3] $\langle B \rangle$ is weighted by $T_{spin}/\, n(H^0)$.

**Table 1.2**
**Comparison of face-on predicted optical lines to BFM spectrum**

| Emission Line | Observed[1] | Enhanced Cosmic Ray Model[2] | Model/Observed |
|---|---|---|---|
| [O II] 3727 | 1.246 | 1.43 | 1.14 |
| [Ne III] 3869 | 0.165 | 0.366 | 0.22 |
| Hγ | 0.460 | 0.467 | 1.02 |
| He I λ4471 | 0.044 | 0.045 | 1.04 |
| [O III] λ4959 | 1.052 | 0.955 | 0.91 |
| [O III] λ5007 | 3.144 | 2.875 | 0.91 |
| [O I] λ5577[3] | 0.003 | 0.0002 | 0.06 |
| [N II] λ5755 | 0.007 | 0.008 | 1.10 |
| He I λ5876 | 0.133 | 0.136 | 1.02 |
| [O I] λ6300[3] | 0.025 | 0.010 | 0.41 |
| [O I] λ6363[3] | 0.007 | 0.003 | 0.50 |
| Hα | 2.960 | 2.893 | 0.98 |
| [N II] λ6584 | 0.548 | 0.588 | 1.07 |
| He I λ6678 | 0.034 | 0.035 | 1.04 |
| [S II] λ6725 | 0.070 | 0.113 | 1.61 |
| [S II] λ6717 | 0.026 | 0.042 | 1.61 |
| [S II] λ6731 | 0.051 | 0.071 | 1.39 |
| [S II] λ6731/λ6717 | 1.642 | 1.663 | 1.02 |
| He I λ7065 | 0.059 | 0.085 | 1.44 |
| [Ar III] λ7751 | 0.036 | 0.049 | 1.36 |
| [S III] λ9069+λ9532 | 1.705 | 1.600 | 0.94 |
| [S III] 9532 | 1.452 | 1.140 | 0.79 |

[1]Line strengths from BFM91, relative to Hβ.

[2]Model predictions are for a face-on observation, relative to Hβ.

[3]Observed line is blended with night sky emission.

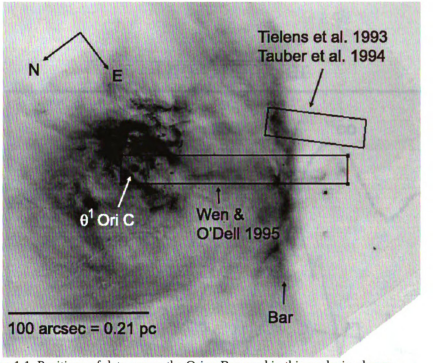


Figure 1.1. Positions of data across the Orion Bar used in this analysis, shown superimposed on a dereddened Hα image provided by C.R. O'Dell. The lines included for each cut are: Wen & O'Dell (1995), Hα; Tauber et al. (1994), $H_2$ and $^{12}CO$. The image is rotated so that the ionizing radiation strikes the Bar from the left, the same as in Figs. 1.2, 1.3, 1.4, 1.5, 1.7 and 1.8.

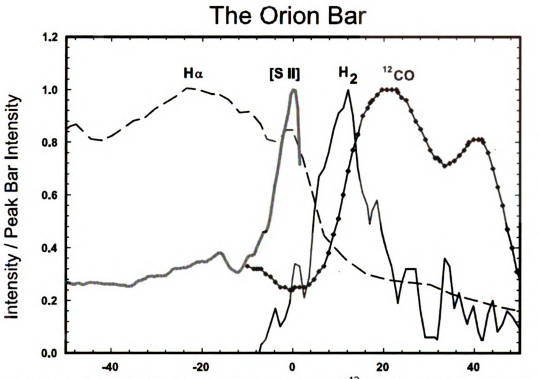


**Figure** 1.2. Observations of the Orion Bar from Tielens et al. 1993 ($^{12}$CO ), Wen and O'Dell 1995 (Hα), **Young** Owl et al. 2000 ($H_2$) and this paper (SII [λ6716+λ6731]), all relative to the IF defined by the peak **in the** [S II] emission. $\theta^1$ Ori C is to the left at –111 arcsec. There is clear stratification indicating an **ioniz**ed region viewed nearly edge-on.

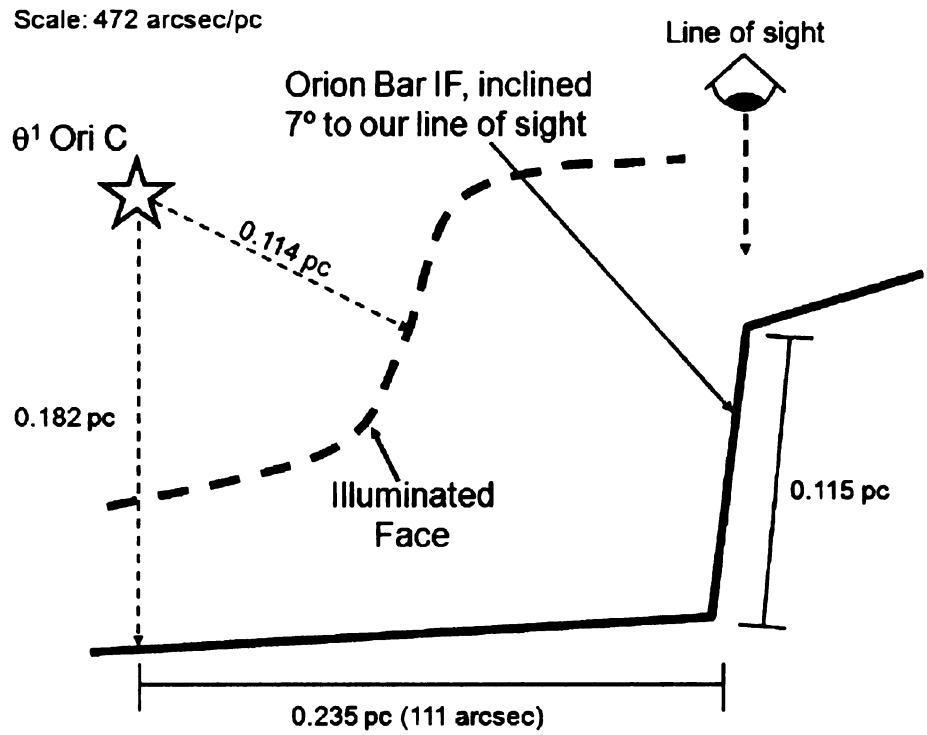


**Figure** 1.3. The geometry derived from the [S II] emission at the ionization front. The Bar is well **represented** by a slab 0.115 pc long inclined at 7 deg to the viewing angle.

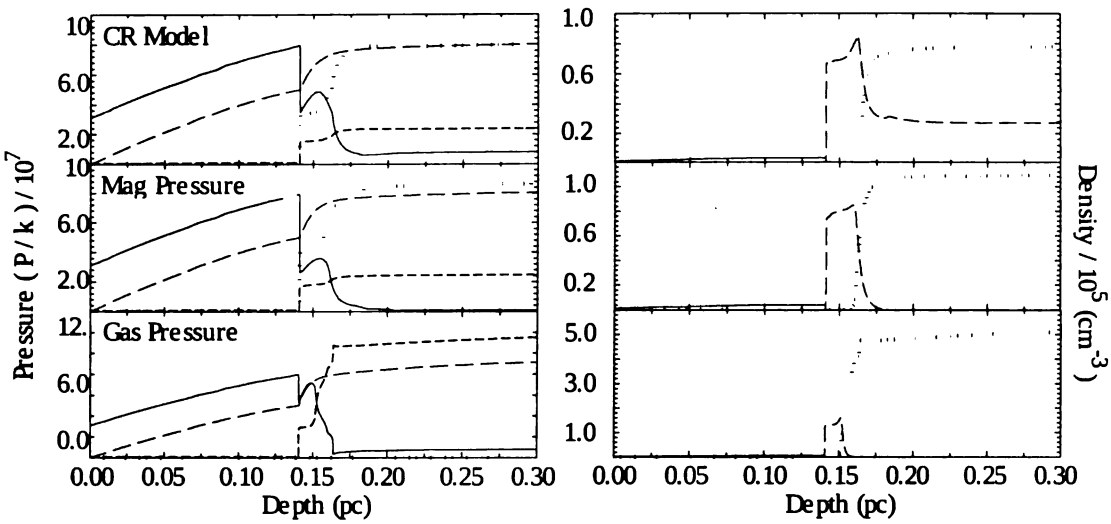


**Figure** 1.4. Pressure and density results from the three basic models developed here. The left-hand column **shows** the various pressure components (gas, magnetic, absorbed radiation from stars, turbulence) as a **function** of depth into the cloud from its illuminated front surface. The gas, magnetic, integrated starlight **and** turbulent pressures are shown as a solid, long dash, dotted and short dashed lines. The right-hand **column** shows the number density of H atoms in the $H^+$, $H^0$ and $H_2$ zones, as a function of depth, so that **the** pressures shown on the left can easily be related to specific zones in the model. The densities are shown **using** solid, dashed and dotted lines, respectively.

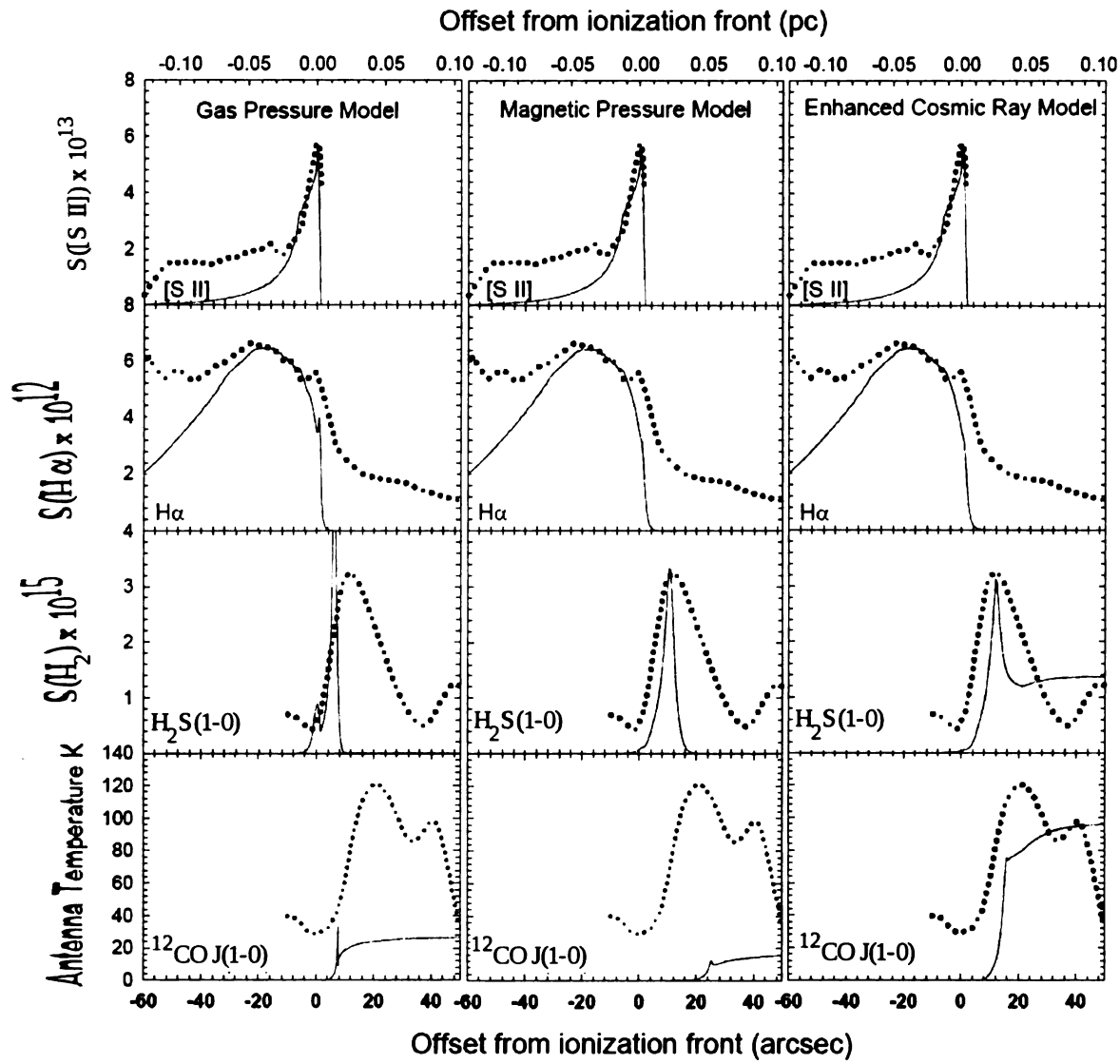


**Figure** 1.5.The surface brightness distributions in key emission lines, in units of erg $s^{-1}$ $cm^{-2}$ $arcsec^{-2}$ or **antenna** temperature, as computed for the three basic models (solid lines), compared to the observed **distributions** (dotted lines).

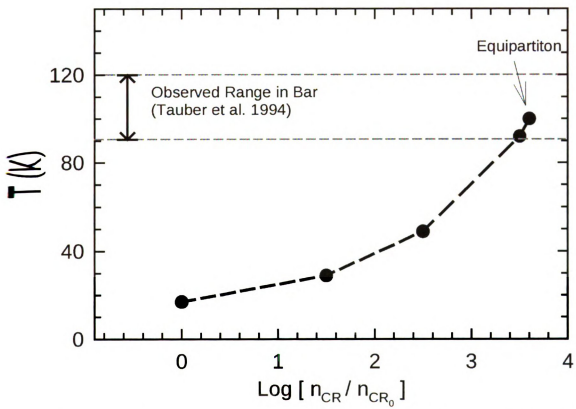


**Figure** 1.6. Predicted $^{12}CO$ brightness temperature as a function of cosmic ray density normalized by the **Galactic** background cosmic ray density $n_{CR0}$.

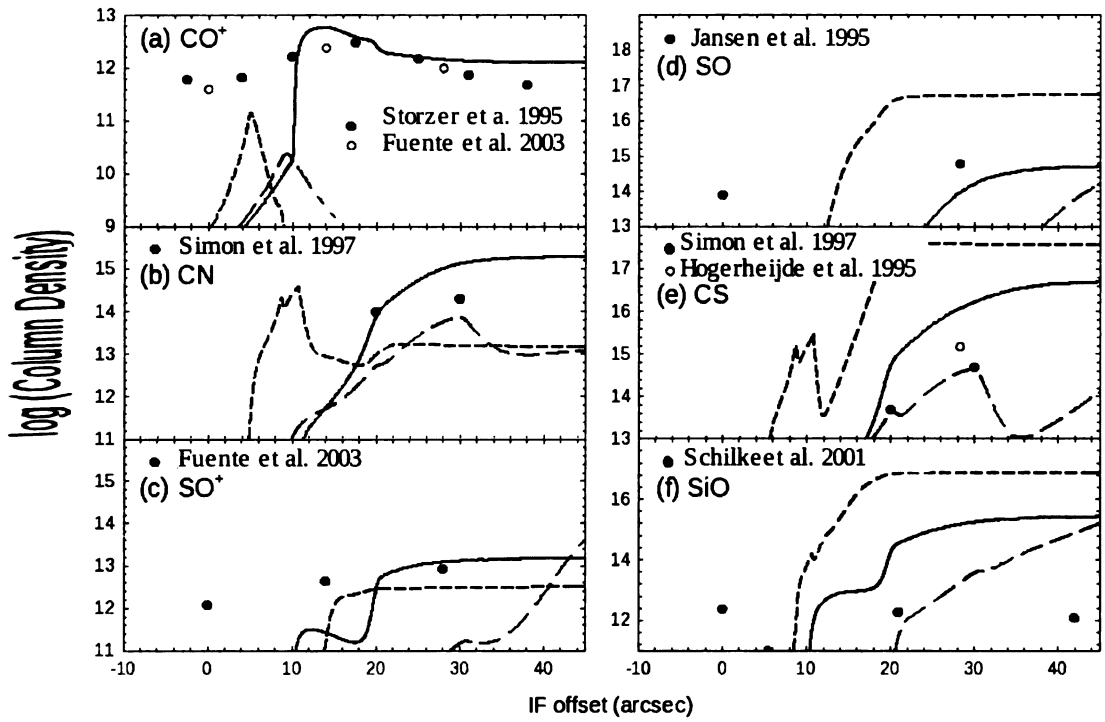


**Figure** 1.7. Diatomic molecular column densities (in $cm^{-2}$) for (a) $CO^+$, (b) CN, (c) $SO^+$, (d) SO, (e) CS, **and** (f) SiO. Modeled and observed values in $cm^{-2}$ as a function of angular projection from the ionization **front**. Shown with a short dash, long dash and solid lines are the gas pressure, magnetic pressure and **enhanced** cosmic ray models. Dots show the various observations of each molecular species.

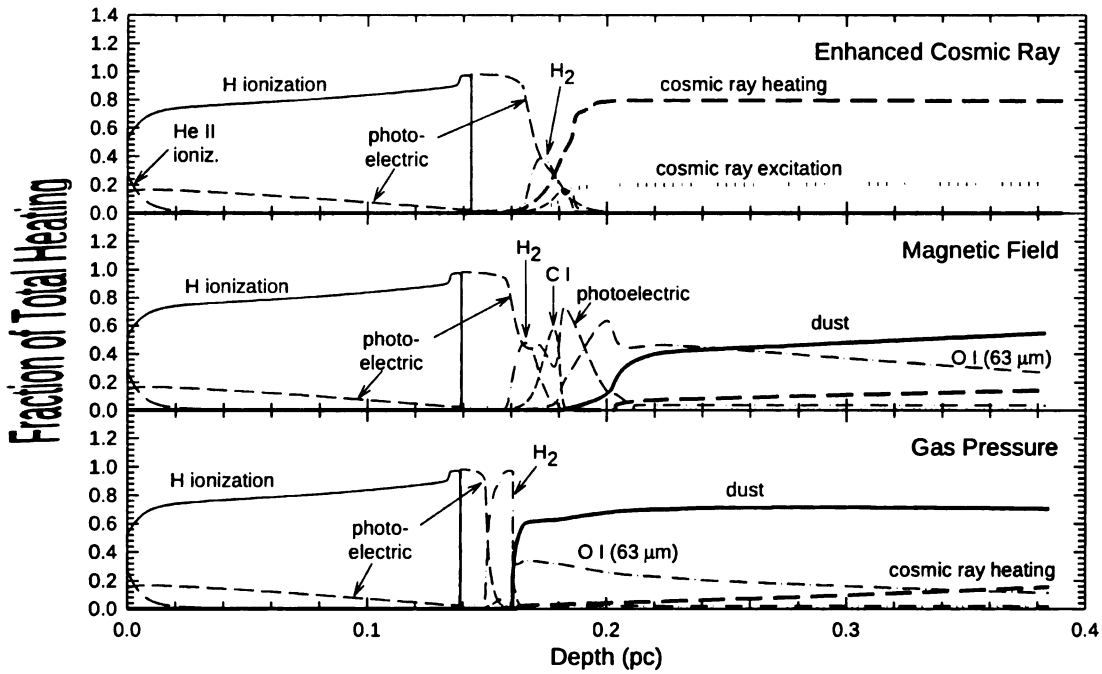


**Figure 1.8.** Heating mechanisms in the three models. The line styles indicating each mechanism are the same in each panel. Photoelectric, $H_2$, C I, dust and O I (63 μm) heating are as defined by Tielens & Hollenbach (1985). We also show heating by H I and He II photoionization in the $H^+$ region, and heating of the molecular gas by direct cosmic ray heating and also by cosmic ray excitation of permitted FUV lines.

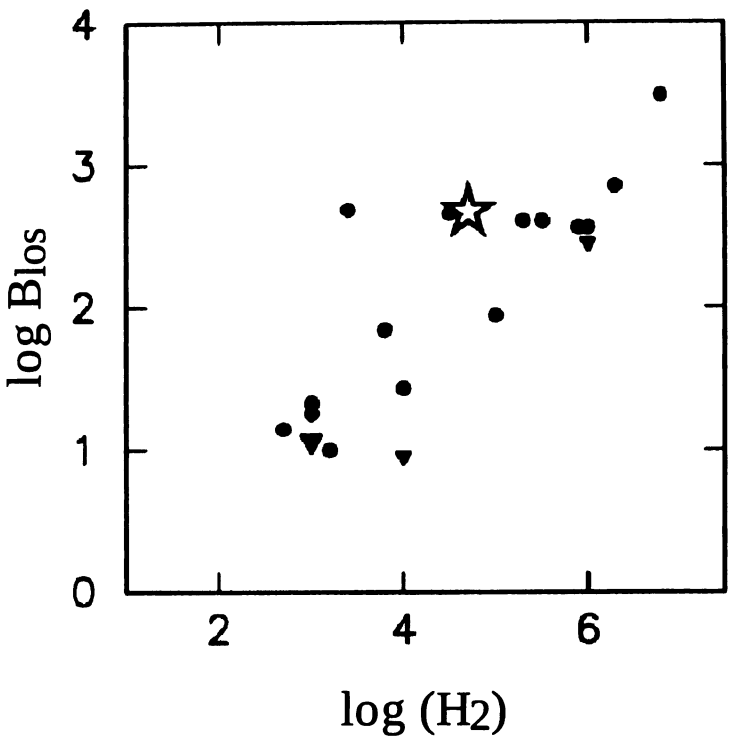


Figure 1.9. Magnetic field strength vs. $H_2$ gas density, adopted from Crutcher (1999). The star indicates our new result for the Orion Bar. The filled circles are other systems for which $B_{los}$ measurements are available, and the triangles are other systems for which upper limits on $B_{los}$ are available.

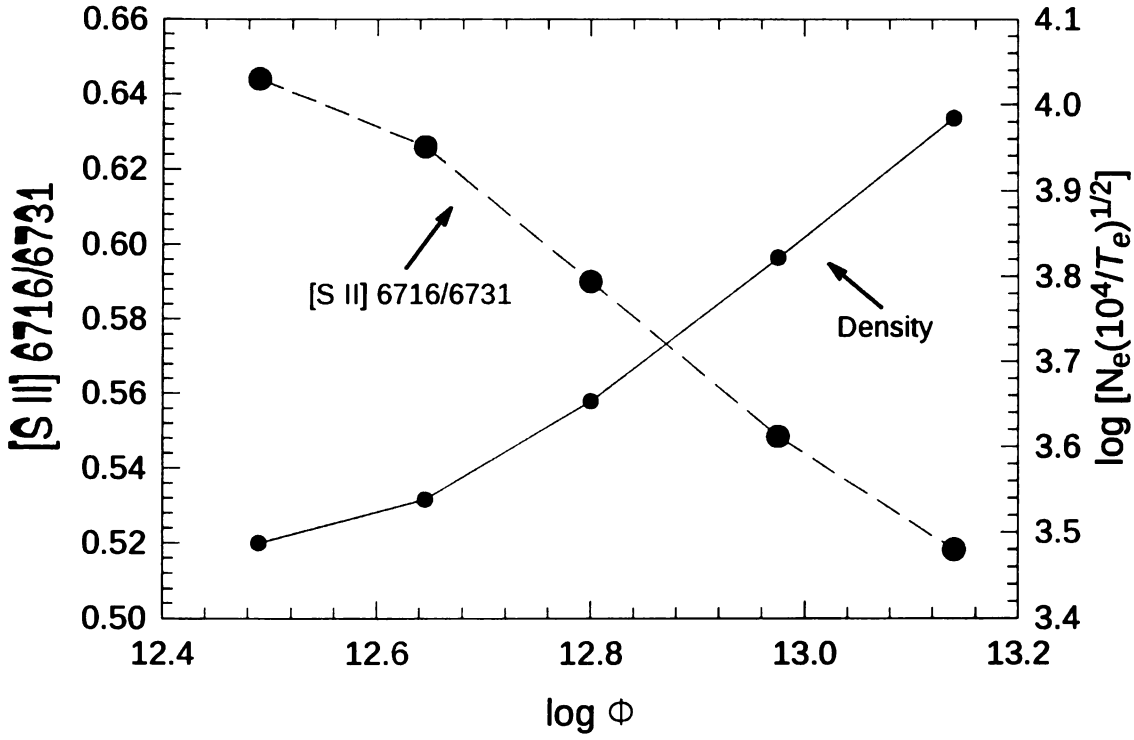


Figure 1.10. Predicted [S II] ratio and density vs. the incident ionizing photon flux $\Phi$(H).

## References


Abel, N.P., Brogan, C.L., Ferland, G.J., O'Dell, C.R., Shaw, G. & Troland, T.H. 2004, ApJ, 609, 247

Abel, N.P., Ferland, G.J., Shaw, G. & van Hoof, P.A.M. 2005, ApJS, 161, 65

Abel, N.P., Ferland, G.J., O'Dell, C.R., Shaw, G. & Troland, T.H. 2006, ApJ, 644, 344

Abel, N.P. & Ferland, G.J. 2006, ApJ, 647, 367

Allers, K. N., Jaffe, D. T., Lacy, J. H., Draine, B. T. & Richter, M. J. 2005, ApJ, 630, 368 (A05)

Bakes, E. L. O. & Tielens, A. G. G. M. 1994, ApJ, 427, 822

Baldwin, J. A., Ferland, G. J., Martin, P. G., Corbin, M. R., Cota, S. A., Peterson, B. M. & Slettebak, A. 1991, ApJ, 374, 580 (BFM91)

Balick, B., Gammon, R. H. & Hjellming, R. M. 1974, PASP, 86, 616

Black, J. H. & van Dishoeck, E. F., 1987, ApJ, 322 412

Bloemen, H. et al 1994, A&A, 281, L5

Bloemen, H. et al., 1999, ApJ, 521, L137

Brogan, C.L. & Troland, T.H. 2001, ApJ, 560, 821

Brogan, C. L., Troland, T. H., Abel, N. P., Goss, W. M. & Crutcher, R. M. 2005, ASP Conference Series, 343, 183

Brogan, C. L., Troland, T. H., Roberts, D. A., & Crutcher, R. M. 1999, ApJ, 515, 304

Castañeda, H.O, Vilchez, J.M. & Copetti, M.V.F 1992, A&A, 260, 370

Crutcher, R. M., 1999, ApJ, 520, 706

Copetti, M.V.F., Mallmann, J.A.H., Schmidt, A.A. & Castañeda, H.O. 2000, A&A, 357, 621

Draine, B. T. & Bertoldi, F. 1996, ApJ, 468, 269

Draine, B. T. 1978, ApJS, 36, 595

Draine, B. T. et al. 2007, ApJ, 663, 866

Feigelson, E. et al. 2005, ApJS, 160, 379

Felli, M., Churchwell, E., Wilson, T. L. & Taylor, G. B., 1993, A&AS, 98, 137

Ferland, G.J. 2001, PASP, 113, 41

Ferland, G. J. Korista, K.T. Verner, D.A. Ferguson, J. W. Kingdon, J.B. & Verner, E.M. 1998, PASP, 110, 761

Fuente, A., Rodriguez-Franco, A., Garcia-Burillo, S., Martin-Pintado, J. & Black, J. H 2003, A&A, 406, 899

García-Díaz, Ma. T. & Henney, W. J. 2007, AJ, 133, 952

Giammanco, C. & Beckman, J. E., 2005, A&A, 437, L11

Güdel, M., Briggs, K.R., Montmerle, T., Audard, M., Rebull, L. & Skinner, S.L. 2008, Science, 319, 309

Hanson, M. M., Howarth, I. D. & Conti, P.S. 1997, ApJ 489, 698

Hauschildt, P. H., Baron, E. & Allard, F. 1997, ApJ, 483, 390

Hayes, J. C., Norman, M. L., Fiedler, R. A., Borden, J. O., Li, P. S., Clark, S. E., ud-Doula, A. & Mac Low, M-M. 2006, ApJS, 165, 188

Henney, W. J. 2007, Diffuse Matter from Star Forming Regions to Active Galaxies, Hartquist, T.W., Pittard, J.M., Falle, S.A.E.G (Dordrecht : Springer), 103

Henney, W. J., Arthur, S. J. & García-Díaz, Ma. T. 2005a, ApJ, 627, 813

Henney, W. J., Arthur, S. J., Williams, R. J. R., Ferland, G. J. 2005b, ApJ, 621, 328

Hirota, T. et al. 2007, PASJ, 59, 897

Hogerheijde, M.R., Jansen, D.J. & van Dishoek, E. F. 1995, A&A, 294 792

Indriolo, N., Geballe, T.R., Oka, T. & McCall, B.J. 2007, ApJ, 671, 1736

Jansen, D. J., Spaans, M., Hogerheijde, M. R. & van Dishoeck, E. F. 1995, A&A, 303, 541

Kellerman, K.I. 1966 ApJ, 146,621

Kristensen, L.E., Ravkilde, T.L., Field, D., Lemaire, J. L. & Pineau Des Forêts, G. 2007, A&A, 469, 561

Krumholz, M.R., Stone, J.M. & Gardiner, T.A. 2007, ApJ, 671, 518

Kurucz, R. L., 2005, MSAIS, 8, 189

Kurucz, R. L., 1979, ApJS, 40, 1

Lazarian, A. & Beresnyak, A. 2006, MNRAS, 373, 1195

Lequeux, J. 2005, The interstellar medium, Translation from the French language edition of: Le Milieu Interstellaire by James Lequeux, EDP Sciences, 2003 Edited by J. Lequeux. Astronomy and Astrophysics Library, Berlin: Springer, 2005.

Leurini, S. et al. 2006, A&A, 454, L47

Miao, Y., Mehringer, D.M., Kuan, Y-J & Snyder, L.E 1995, ApJ, 445, L59

O'Dell, C.R. 2001, ARA&A, 39, 99

O'Dell, C. R & Doi, T. 1999, PASP, 111, 1316

O'Dell, C.R., Walter, D.K. & Dufour, R.J. 1992, ApJL, 399, L67.

Osterbrock, D.E. & Ferland, G.J. 2006, Astrophysics of Gaseous Nebulae and Active Galactic Nuclei, 2nd Edition, University Science Books, Sausalito (AGN3)

Osterbrock, D.E., Tran, H.D. & Veilleux, S. 1992, ApJ, 389, 196

Pellegrini, E. W. et al. 2007, ApJ, 658, 1119 (Paper I)

Pogge, R.W., Owen, J. M. & Atwood, B. 1992, ApJ, 399, 147

Ramaty, R. 1996, A&AS, 120, 373

Roshi, D.A. 2007, ApJ(Letters), 658, L41

Röllig, M., et al., 2007, A&A, 467, 187

Rybicki, G. B. & Lightman, A. P. 2004, Radiative Processes in Astrophysics, 1st edition, Wiley-Interscience,Weinheim

Rubin, R. H., Simpson, J. R., Haas, M. R., & Erickson, E. F. 1991, ApJ, 374, 564

Rubin, R.H., Dufour, R.J. & Walter, D.K. 1993, ApJ, 413, 242

Schilke, P., Pineau des Forêts, G., Walmsley, C. M. & Martín-Pintado, J. 2001, A&A, 372, 291

Schleuning, D.A., 1998, ApJ, 493, 811

Shaw, G., Ferland, G. J., Abel, N. P., Stancil, P. C., & van Hoof, P. A. M. 2005, ApJ, 624, 794

Shaw, G., Ferland, G. J., Henney, W. J., Stancil, P. C., Abel, N. P., Pellegrini, E.W., Baldwin, J.A. & van Hoof, P. A. M. 2008, ApJ, (submitted) (Paper III)

Simon, R., Stutzki, J., Sternberg, A., Winnewisser, G., 1997, A&A, 327, 12

Snodin, A.P., Brandenburg, A., Mee, A.J. & Shukurov, A. 2006, MNRAS, 373, 643

Smith, L.J., Norris, R.P.F. & Crowther, P.A. 2002, MNRAS, 337, 1309

Springel, V., 2005, MNRAS, 364, 1105

Sternberg, A., Hoffmann, T.L. & Pauldrach, A.W.A. 2003, ApJ, 599, 1333.

Störzer, H., Stutzki, J. &; Sternberg, A. 1995, A&A, 296, L9

Tauber J. A., Tielens, A. G. G. M., Meixner, M. & Goldsmith, P. 1994, ApJ, 422, 136

Tielens A. G. G.M. & Hollenbach, D. 1985, ApJ, 291, 722

Tielens, A. G. G. M., Meixner, M. M., van der Werf, P. P., Bregman, J., Tauber, J. A., Stutzki, J., & Rank, D., 1993, Science, 262, 86

Vacca, W. D., Garmany, C. D. & Shull, J. M. 1996, ApJ, 460, 914

van der Tak, F.F.S. et al. 2006, A&A, 454L, 99

van der Werf, P. P., Stutzki, J., Sternberg, A., Krabbe, A., 1996, A&A, 313, 633

Wade, G.A., Fullerton, A.W., Donati, J.-F., Landstreet, J.D., Petit, P. & Strasser, S. 2006, A&A, 451, 195

Walmsley, C. M., Natta, A., Olivia, E., & Testi, L. 2000, A&A, 364, 301

Webber, W.R. 1998, ApJ, 506, 329

Wen, Z. & O'Dell, C. R. 1995, ApJ, 438, 784

Williams, J. P., Bergin, E.A., Caselli, P., Myers, P. C. & Plume. R. 1998, ApJ, 503, 689

Wilson, T.L. & Rood, R. 1994, ARA&A, 32, 191

Young Owl, R.C., Meixner, M.M., Wolfire, M., Tielens, A. G. G. M. & Tauber, J. 2000, ApJ, 540, 886

Yusef-Zadeh, F., Wardle, M. & Roy, S., 2007 ApJL, 665, 123

Zuckerman, B. 1973, ApJ, 183, 863

## Chapter 2

## Deconstructing the Structure and Physical Processes of 30 Doradus


### Abstract

We have completed a study of a 140 x 80 pc region of 30 Doradus centered on R136 based on a new optical imaging and spectrophotometric survey covering key diagnostic emission lines, together with photoionization modeling with CLOUDY. We focus on the physical conditions, geometry and importance of radiation pressure on a point by point basis to replace with constraints some of the assumptions that go into modeling and interpreting distant sites of star formation. The observed survey is a compromise between spatial density of the grid and areal coverage. The final science quality data products are available to the public via the NVO. While stellar winds and supernovae undoubtedly produce shocks, we find no spectral signature to indicate shocks are currently important for driving the large scale structure. We conclude that the considerable region covered by our survey is well described by photoionization from the central cluster where the ionizing continuum is dominated by the most massive O stars. The completeness of our survey allows us to create a composite spectrum of 30 Doradus, simulating the observable spectrum of a spatially unresolved, distant HII region. Using this spatially integrated spectrum we confront various strong line abundance techniques, which are typically applied to an entire HII region or galaxy, against abundance estimates using spatially resolved observations of 30 Doradus. We find that despite averaging over more than an order of magnitude in ionization parameter and density, the abundances estimated using the diagnostic lines of the composite spectrum are in agreement with spatially resolved abundance studies.

## 1 Introduction

Star formation is a fundamental step in the continuous chemical and structural evolution of the universe. Intense star formation is an ongoing process of cloud collapse, stellar birth and the inevitable enrichment and destruction of natal clouds. Light and winds from a newly-formed star cluster interact with the parent molecular cloud. This sculpts the geometry of the regions, produces the observed emission-line spectrum, and most importantly throttles the rate of star formation. This ongoing process is tracked in other galaxies throughout the universe via strong emission lines that are characteristic of H II regions. Because of the distances between galaxies, resolving all but the largest spatial structures of most extragalactic H II regions is not possible. Therefore our understanding of star formation in distant parts of the universe is largely based on models of the ISM and extrapolation of nearby systems to explain the observed emission lines.

To determine *how* massive clusters throttle star formation, we are making detailed studies of a succession of larger and larger local star-forming regions, so far of the Orion Nebula and M17 and now 30 Doradus (30 Dor). These nearby objects offer high spatial resolution of the many structural details that in more distant objects would be blended together and thus confuse the physical interpretation. The Orion Nebula is dominated by a single O star and is the smallest scale we will consider. The O star forms a blister H II region on the surface of a background molecular cloud. Multiple studies have explored the correlation between photon flux and gas density. In Pellegrini et al. (2009; hereafter P09), we showed that the detailed physical conditions of a bright IF called the Orion Bar were set by the absorbed energy and momentum of stellar radiation. A similar situation was realized in the larger H II region of M17 (Pellegrini et al. 2008; P08) where the

physical conditions were in part determined by the integrated momentum in starlight. In both regions we found a magnetic field of plausible strength was likely supporting the molecular gas against collapse from the integrated starlight's pressure.

To move these calibrations up to a scale more like that of distant giant star forming regions, we turn here to 30 Doradus. At a distance of 48.5 kpc (Marci 2006) it is the only giant H II region in the local group we are capable of studying on a sub-parsec scale using ground based observations.

30 Dor is the largest star-forming region in Local Group, with almost 500 times more ionizing photons than the Orion Nebula. Other nearby large H II regions include NGC3603, the largest optically visible star forming region in the Milky Way. This very young system is found in the plane of the galaxy and suffered significant extinction. The cluster in NGC3603 is very compact, containing more than 50 O-stars within a 2 parsec diameter, generating at least $10^{51}$ ionizing photons $s^{-1}$. NGC 604 the second largest star forming region in the Local Group, is approximately 1/4 the size of 30 Doradus, but is 20 times farther from the Sun.

30 Doradus stands out in any wide-scale optical image of LMC. and is nearly visible to the naked eye as a smudge in dark skies. The central 13 pc contain most of the approximately 2400 massive O and B stars (Parker 1993) ranging in age from 1-10 Myr. This includes the dense star cluster known as R136 which includes more O4 and O3 stars with masses in excess of 100 $M_{\odot}$, among the highest luminosity stars that are known. The total cluster mass is of the order $10^4 - 10^5$ $M_{\odot}$ with 2-3 times more ionizing stars than any cluster in the Milky Way.

The violent history of the region has led to vast cavities and shell like structures around R136. These structures are visible in optical and IR ionization-front tracers like [S II] and 8μm PAH emission. Many of these structures have Hα velocity profiles which show them to be expanding shells. Filling these cavities is a $10^6$ K gas visible in X-ray emission. The correlation between this emission and the expanding shells lead to the conclusion that the SNe were likely the cause of the current dynamics (Chu & Kennicutt 1994). These shells have typical kinetic energies equal to $10^{51}$ erg. The total kinetic energy in the vicinity of R136 is $10^{52}$ ergs. Within reasonable estimates about the timescale for injecting energy from stellar winds into the ISM it is equally likely that stellar winds are the energy source. These types of kinematic arguments suggest SNe or stellar winds are a likely source of energy.

The remaining molecular gas cloud has been observed in optically thick CO emission (Poglitsch 1995). This molecular cloud runs NE-SW through R136. The brightest arcs appear to trace the surface of this molecular cloud, and are bright because of their high density. 30 Dor has been named the "Tarantula Nebula" because images showing emission lines are dominated by the interwoven pattern of these bright arcs. However the majority of the line emission originates in the extended regions of low surface brightness, which tend to be associated with X-ray emission.

Through the use of modeling, we test the assumption that 30 Doradus can be explained as a scaled up version of smaller H II regions. Specifically we test whether the optical emission-line spectrum can be explained by a nebula with a constant metal and dust abundance, as determined by deep spectroscopic studies, being ionized by a single young

stellar central cluster. If not, the nebula may be too chaotic to be adequately described by just a few global parameters, as is commonly done for distant GEHRs. We will conclude by considering what we could tell about 30 Doradus if it were at a distance such that it could only be observed via an integrated spectrum.

The modeling process of such distant H II regions has been refined to eliminate as many free parameters as possible (Dopita et al. 2006). The energy injected into a system can by modeled with the stellar synthesis code Starburst99 (Leitherer et al. 1999). This provides the time dependent evolution of a stellar population of a given metallicity, including the spectral energy distribution (SED), the total number of ionizing photons, and mechanical energy released by stellar winds and supernova. Other necessary input parameters include an initial mass function (IMF), and either total cluster mass for an instantaneous burst of star-formation, or a stellar formation rate if continuous. With the assumption of pressure balance between the H II region and surrounding material, the radius and density of the nebula at any given time are described by a shell, swept up by the mechanical energy of the supernova and winds (Dopita et al. 2006b). These assumptions uniquely determine the instantaneous ionization parameter $U$ of the idealized H II region, where U is defined as is the flux of photons per hydrogen atom defined as

$$U = \frac{Q_0}{4\pi c r^2 n_H} \qquad (1)$$

where $Q_0$ is the number of ionizing photons from the ionizing source, $r$ is the distance from the ionizing source to the cloud and $n_H$ is the density of hydrogen. In a typical H II region the fraction of neutral hydrogen is very low and $n_H = n_e$.

Finally, the emission line spectrum as a function of metallicity can be modeled with

plasma simulation codes such as CLOUDY or MAPPINGS to determine the gas abundances. This paper will test how well this procedure works in the case of a single, resolvable Giant Extragalactic H II Region (GEHR).

## 2 Observations

### 2.1 Existing optical passband data sets

Most of the strong optical emission lines from star-forming regions trace ionized gas at electron temperatures $T_e \sim 10^4$ K. A few key lines from O I, O II, N II and S II form in the interface region at the edge of ionization-bounded clouds. The elements S, O, N, Ar have transitions visible from the ground that are sensitive to both $T_e$ and the electron density $n_e$, and also to gas phase abundances. Even though 30 Dor is a key example of a GEHR, the available measurements of it in the emission lines of these elements, using either direct imaging or especially spectroscopy, are surprisingly limited.

The best existing publicly available narrow-band optical image data sets are the Magellanic Cloud Emission Line Survey (MCELS), and archival HST images. The MCELS survey (Smith 2005) covers the central 8×8 degrees$^2$ of the LMC including 30 Dor, in Hα + [N II], [O III] and [S II] (using many of the same emission line and continuum filters listed below in Table 2.1). However, the data were taken with the 0.9m Schmidt telescope at CTIO and have a spatial scale of 2.3 arcsec pixel$^{-1}$ with a resolution closer to 5 arcsec FWHM. This means that structures smaller than 1.2 pc are unresolved, blurring fine details in the ionization structure that otherwise could be used to remove ambiguities in the interpretation of emission line spectra.

The HST archival data covers the central 4.5 by 3 arcmin of 30 Dor with at least 0.1

arcsec resolution (Scowen 1998, Walborn et al. 2001) in Hα, [O III] and [S II], revealing vastly more detail. However the HST data are limited to the brighter central region around R136. Since the brighter nebula accounts for only 25 percent of the total nebular emission in Hα the limited spatial coverage of HST misses the bulk of the emission that would be detected if 30 Dor were viewed from a much greater distance.

Turning to the available spectroscopy, Krabbe & Copetti (2002) obtained a set of long-slit observations which covered Hβ, [O III] λ4363 and [O III] λ5007 at 135 points along three slit positions. The sensitivity of these spectra is comparable to our Blanco survey described below, and the data were used to measure temperature fluctuations (see Section 4.4, below).

Mathis, Chu & Peterson (1985) had previously obtained spectra covering a similar wavelength range at four other slit positions. They presented line strengths measured for 22 extracted regions covering typically 30 to 60 arcsec each along the slit.

Chu & Kennicutt (1994) used the CTIO echelle spectrograph in a single order to obtain a sparse grid of long-slit spectra that covered the Hα and [N II] λλ 6548, 6584 emission lines with high (20 km $sec^{-1}$) velocity resolution. They found that about half of the kinetic energy in 30 Dor is contained in shells in the central regions which are expanding with characteristic velocities $v \sim$ 20-200 km $sec^{-1}$, and that the kinetic energy contained in this expansion greatly exceeds the gravitational binding energy.

There has also been a limited amount of deep echelle spectroscopy covering a much wider wavelength range (Tsamis et al. 2003; Peimbert 2003). These spectra measured hundreds of emission lines that can be used for detailed chemical abundance analysis,

and also cleanly resolve the density sensitive [O II] λλ3726,3729 doublet and many other lines which are blended at lower spectral resolution. However, they require relatively long exposures and very short slit lengths, so have only very small areal coverage on 30 Dor.

Each of these existing measurements will be discussed below as needed.

### 2.2 New Narrow-Band Images

To the existing data sets we added a new set of narrow-band images taken with the SOAR Optical Imager (SOI) on the 4.1m SOAR Telescope[5]. We used the Hα 6563×75, [S II] 6738×50, [O III] 5019×15 emission-line filters and the 6850 ×100 and 5130×155 continuum filters from the CTIO 3×3 and 4×4 $in^2$ filter sets, where the filter names refer to the approximate central wavelengths and FWHM bandpasses. A summary of the SOI observations is given in Table 2.1.

In each passband we took grids of 5×5 $arcmin^2$ SOI images, overlapping them to give a 12×13 $arcmin^2$ field of view with a scale of 0.15 arcsec $pixel^{-1}$. The individual images were then combined to create final mosaic images in each passband. Due to the significant spatial overlap of the individual images, the total integration time in a given filter varies across the mosaic. Table 2.1 includes for each filter the resulting minimum and maximum integration times at any point in the mosaic. The data are seeing-limited, with full width at half maximum intensity FWHM = 0.5–0.9 arcsec, much better than the 5 arcsec FWHM in the MCELS survey, and are three times more sensitive to diffuse

[5]The Southern Astrophysical Research (SOAR) Telescope is a joint project of Michigan State University,Ministério da Ciência e Tecnologia-Brazil, the University of North Carolina at Chapel Hill, and the National Optical Astronomy Observatory. Further information about SOAR and its instruments may be found at www.soartelescope.org.

nebular emission than the HST data set.

As an example of the results, Figure 2.1a shows the mosaic image made with the Hα + [N II] filter, prior to continuum subtraction. The central cluster R136 is marked with a white cross. The 1 arcmin scale bar is equivalent to 14.1 pc for an LMC distance of 48.5 kpc (Marci 2006). Figure 2.1b shows, on the same image, the slit positions used in the Blanco spectroscopic survey described below.

The two continuum filters were used to measure the emission from point sources (stars), together with the nebular continuum and starlight scattered off dust. The continuum image count rates were scaled and subtracted from the emission line image to give a nebular count rate $R_{line}$ in each filter, according to

$$R_{line} = R_{narrow} - R_{cont} \times \frac{W_{narrow}}{W_{cont}}, \qquad (2)$$

where $R_{narrow}$ and $R_{cont}$ are equal to the atmospheric-extinction corrected count rate for the narrow band and continuum filters, respectively, and the effective filter width $W_i$ in the $i^{th}$ filter is

$$W_i = \int T_{i\lambda}\, d\lambda \qquad (3)$$

where the transmission curve $T_\lambda$ was measured by the SOAR staff before the beginning of the program.

Changes in stellar scattered light, seeing or sky brightness between the time the emission lines were measured and the continuum was measured were found to be a limiting factor in the quality of the continuum-subtracted images, so the observations with the continuum and emission filters were made sequentially one after the other before

offsetting the telescope to each new point in the mosaic grid.

## 2.3 Spectrophotometry

### 2.3.1 The Blanco Telescope Spectral Grid

In Feb 2008 we obtained a grid of long-slit spectra of 30 Dor using the RC spectrograph on the 4m Blanco telescope at CTIO. The spectrograph slit was 5 arcmin in length, and was positioned at a total of 37 different locations spanning the nebula (Figure 2.1b). Two sets of spectra were taken at orthogonal angles. The slit position angles PA = 13 deg and PA = 103 deg were chosen to maximize the number of key ionization fronts that could be covered with the slit either crossing the ionization fronts at an approximately perpendicular angle or running directly along them. The Blanco telescope uses an equatorial mount, which results in a constant position angle of the slit once the instrument has been rotated to the correct PA. We minimized the uncertainty in the PA by rotating the slit only once each night, after all observations at the initial PA were completed. As a result we have a high degree of confidence in our stated position angles, and therefore of the mapping onto the sky of individual points along the slit.

Table 2.2 lists for each slit position the identifying position number, the RA and Dec of the slit center in J2000 coordinates, the PA, and the total exposure time. For simplicity, slit positions with PA = 13 deg are numbered beginning at 1 at the easternmost position and incrementing up through 17 increasing toward the west, including the two most extreme north and south slit positions (position numbers 16 and 17, respectively). Numbering of slit positions with PA =103 deg then begins at 20 and increases towards the south, with even numbered slit positions centered to the east of R136 and odd numbered ones to the west. The only exception is position 31 which has a PA equal to 98

degrees. Positions 40-44 were taken with the SOAR Telescope and are described in the following sub-section.

The Blanco Telescope observations were taken under photometric conditions with a slit width of 3.5 arcsec. Accurate offsetting was achieved by moving the autoguider probe by known amounts, and fiducial stars of known coordinates were placed in the slit at most of the slit positions in order to internally calibrate the position on the sky. An autoguider maintained the position to better than 1 arcsec.

The standard IRAF 'LONGSLIT' package was used to generate bias and flat-field corrected, flux calibrated long-slit spectra, rectified to remove optical distortions and to convert to a linear wavelength scale. The wavelength solution had an RMS uncertainty of 0.06 Å. After performing the distortion correction using the wavelength calibration, any additional wavelength shifts due to flexure within the spectrograph were corrected by shifting each spectrum so that the [O I] λ5577.33 Å night sky line fell at the correct wavelength. The spectrophotometric standard stars LTT 2415, Hiltner 600 and CD32 from Hamuy et al. (1994) were observed on each night, through a 7 arcsec slit, to obtain an absolute flux calibration.

### 2.3.2 Additional SOAR Telescope Spectroscopy

Six additional locations in 30 Dor were observed with the Goodman High-Throughput Spectrograph on the SOAR telescope, on 5 Feb 2009. The instrument was used with a single slit 3.9 arcmin long and 0.46 arcsec wide, with its 300 line/mm grating. The wavelength range was 3950 Å to 9335 Å with 1.32 Å pixel$^{-1}$ sampling and a spectral resolution of 4.9 Å FWHM at H$\alpha$ . This setup easily resolved the [S II] doublet near

6720 Å and the [O II] lines at λλ7320, 7330 Å.

Calibration of the data was performed with the spectroscopic packages in IRAF in a fashion similar to the method described above for the Blanco data, with a few notable exceptions. The spectrophotometric standard stars LTT 2415 and LTT 4816 were observed, without a slit, to obtain an absolute flux calibration. There is second order contamination in the spectra beyond 7700Å, with the sensitivity in second order below 3850 Å being about 36 per cent of that in first order at the same wavelength. This is not a major problem for measurements of the the nebular emission lines in the red (observed in first order), because at the positions of these lines the contaminating second-order light is mostly continuum emission. But the second-order contamination does strongly affect the flux calibration. This was accounted for by observing the standard stars through two different second-order blocking filters, GG385 and GG495, which cut off light blueward of 3850 and 4950 Å, respectively. The GG385 filter was used for the nebular observations and for the flux calibration for wavelengths lower than 7000 Å, while the GG495 filter was used only for the flux calibration beyond 7000 Å. To stitch together a flux calibration combined over the full wavelength range, a sensitivity response curve was generated separately for each filter, using the IRAF 2D spectroscopic reduction package. A final response curve was made using the GG 385 curve below 7000 Å and the GG495 curve at longer wavelengths.

Fringing with the current CCD is severe, reaching 32 percent at 9000 Å. To calibrate this, an internal quartz lamp was observed immediately after the series of nebular exposures at each slit position, before moving the telescope. In spite of this precaution, flexure within the instrument still caused significant, obvious offsets between the fringes in the nebular

data and in the quartz calibration frame. We used the fringe pattern seen in the spectra of fiducial stars that fell in the slit as a guide for shifting and scaling in amplitude the quartz fringe frames before dividing out the fringe pattern. This procedure decreased the amplitude of the residual fringing to 10 percent.

The SOAR spectra sample an area of very low [S II]/Hα intensity ratio, lying to the east of R136. Figure 2.2 shows the SOAR slit positions superimposed on a map of the [S II]/ Hα intensity ratio made from our SOAR images. The orientation and spatial coverage of Figure 2.2 is the same as that of Figure 2.1. At the time of the observations the SOAR Telescope lacked an atmospheric dispersion corrector, which is important with our broad wavelength coverage and narrow slit. As a result our observations were restricted to nearly the parallactic angle, resulting in the pattern shown in Figure 2.2. The positions of the Goodman spectra are numbered beginning at 40, to minimize confusion between the two spectroscopic data sets.

To remove night sky contamination we obtained a spectrum of the sky 2 deg north and 2.687 deg east of R136. The sky spectrum was smoothed with a median filter spanning 15 arcsec along the slit, to decrease noise and remove stars along the slit. The intensity in the night sky lines was then scaled to match the object frames and subtracted. The redshift of the LMC helps to separate night sky forbidden lines from the same lines from 30 Dor. For example, in the case of the [O I] λ6300 line, the nebular emission line is redshifted to 6306 Å. Figure 2.3 shows a typical spectrum before and after night sky subtraction, in the regions around 6300 Å and 7330 Å.

The instrument setup used includes the low ionization species [O I] λ6300, [O II] λλ7320, 7330 as well as the highly ionized [S III] λ9068 line and offers a clean

unblended measurement of [S III] λ6312 redshifted to 6318Å. All of these lines except for [S III] λ9069 are also within the wavelength range of the Blanco spectra but in that case are heavily blended with night sky lines and/or nebular emission and so were not measured. The region east of R136 was re-observed with SOAR because of the additional constraints which these lines provide when determining the ionization parameter *U*, the energy distribution of the ionizing radiation, and the O/H and S/H abundances.

## 3 The spectroscopic 'data cube'

### 3.1 Emission Line Flux Measurements

Table 2.3 lists the emission lines measured from the Blanco and SOAR spectra. Columns 1 through 3 indicate the observed and rest wavelengths and ionic species. The fourth column lists the extinction coefficient used to deredden the observations, using a standard Galactic extinction curve with a ratio of total to selective extinction $R$=3.1 (Cardelli et al. 1989). The final column indicates which data sets include the emission line.

We wrote a FORTRAN program which extracted 1D spectra binned over successive 2.5 arcsec increments along the slit in the 2D spectra. The 2.5 arcsec width of the extraction window along the slit was chosen so that the in the fainter regions the line flux equaled the noise in the continuum. The program then automatically measured, in each extracted 1D spectrum, the emission line fluxes and their uncertainty. This produced a 'data cube' of emission-line intensity measurements at 4238 points on the 30 Dor nebula.

We needed to use a summation approach to measure the flux in each emission line profile because of the often complicated shape of the profiles. For the Blanco spectra, a slit width of 3.5 arcsec was chosen to maximize the signal of the faintest lines while still

separating the [S II] doublet. However, with such a wide slit, spatial variability of the surface brightness of the nebula is imprinted onto the line profile in the spectrum, as is seen in Figure 2.4. Figure 2.4a shows an enlarged portion of the SOAR [O III] image at the position of a ring-like structure, and Figure 2.4b shows the [O III] λ4959 line in the 2D image of the Blanco spectrum crossing this same location. The black dashed lines on Figure 2.4a indicate the region over which the spectrum in Figure 2.4b was extracted. The resulting profiles in Figure 2.4b clearly reflect the spatial structure rather than the velocity structure of the gas. This resulted in often-ragged line profiles which were better measured by summing the total flux above a fitted continuum rather than by fitting a Gaussian. Figure 2.4c shows the extracted line profile at the location marked in Figure 2.4, with a best-fitting Gaussian shape superimposed to demonstrate that line shape is not well represented by a simple Gaussian.

The wavelength windows used in the automated line-measuring procedure were manually set in advance, using the brightest regions of the nebula. Two examples of wavelength windows are presented in Figure 2.5. In the case of an isolated line like He I λ6678, two 'wing' boundaries are chosen to include all of the line flux shown by the vertical dashed lines. The continuum regions (indicated by horizontal dashed lines) are separately defined on either side of the emission line, avoiding other emission lines. In the case of mildly blended lines like the [S II] λλ6716, 6731 doublet, the wings are defined to include the total flux from both lines. A search for the minimum flux over the width of the solid horizontal bar shown in Figure 2.5 is is used to define the point of separation between the extraction windows of the two lines. This does not perfectly deblend the two lines, but since the ratio of [S II] λ6716/ λ6731 is always of order unity

the error is negligible. This procedure for measuring the line strengths works well even in the cases where stars are present in the extraction region so long as the star is not extremely bright or the nebula extremely faint. Possible problem cases were identified using the continuum bins, and were checked manually and for a few cases all emission lines at that position were left out of analysis. In the case of bright stars with strong absorption features the surface brightness of Hβ will be underestimated. Star clusters were intentionally avoided and the number of regions affected by stellar absorption are small.

### 3.2 Noise Estimates

We estimated the uncertainties in the measured line strengths by assuming Poisson statistics in the original photon count rate and then carrying parallel noise images all the way through the same reduction process as the data images. At the beginning of the data reduction the measured counts were converted to photons using the known detector gain. An initial noise image was then created according to

$$\sigma = (N_{photons} + gain \times ReadNoise^2_{electrons})^{1/2} \quad (4)$$

All multiplicative factors to the data such as flat fields, illumination corrections and the flux calibration were applied to the the noise image by multiplying the values in the noise image. In the step where the spectra were linearized and distortion was corrected, there was a re-binning of the data. In this case the variance of the noise was formed and rebinned in the same way so that the noise in each pixel was summed in quadrature. We manually inspected a random set of extracted spectra and verified that these estimated errors do in fact reasonably measure the observed pixel-to-pixel scatter in the continuum

points. An exception to this is [O III] λ4363, where uncertainties in the continuum level and blending with the wings of H I λ4340 cause special problems, as is discussed below.

### 3.3 Detector Saturation

The large range in the surface brightness of the nebula meant that the 5 arcmin long slit included both bright and faint regions. In order to get a sufficiently high signal/noise ratio in the faint regions, long exposures were used and the [O III] λ5007 and/or Hα lines were often saturated at various places along the slit. Where necessary additional short exposures were made to correct for saturation. All repeated observations of a single position, long and short, were gray-shifted to the highest value according to the total flux of the [O III] λ4959 line summed over the full 300 arcsec length of the slit. The λ4959 line was used because it is a moderately strong line but is never saturated. Summing along the slit minimizes any effects of variable seeing or telescope drift. As a final check to the data, line ratios of extracted regions were compared wherever two slits intersected. While the extracted regions at these points overlap, they do not sample completely identical parts of the nebula. The normalized histogram shown in Figure 2.6 demonstrates the repeatability of [O III] λ5007/Hβ and ([S II] λ6716+λ6731)/Hα measured for these overlapping observations. The histogram shows that the data do repeat to within the typical range of differences due to the mismatch between the areas sampled on th sky by the two slits , with especially good repeatability in the [O III]/Hβ ratio.

### 3.4 Reddening Correction

The reddening was determined separately for each extracted 1D spectrum, using the

observed Hα/Hβ intensity ratio and assuming an intrinsic ratio of 2.87 appropriate for Case B and a gas temperature $10^4$ K (Osterbrock and Ferland 2006) and $R$=3.1. This is adequate even though 30 Dor is in the LMC because (1) although the LMC extinction curve departs considerably from the Galactic curve in the ultraviolet, the two are very similar in the optical passband, and (2) some considerable part of the reddening is in any case due to foreground material within our own Galaxy. We then applied the reddening to each measured line from the same extracted 1D spectrum, using the wavelength-dependent extinction coefficients $f_\lambda$ from Table 2.3. A check on the validity of this procedure is that the dereddened Hγ/Hβ ratios agree with the predicted Case B values to within an average of 3 percent, with a 1σ scatter of 4 percent which is consistent with the observational errors.

### 3.5 Electron Density and Temperature

At each position along each spectrograph slit we determined the electron density $n_e$ from the dereddened [S II] λ6716/λ6731 line ratio. The IRAF/STSDAS task nebular was used to derive the electron densities using a 5 level sulpher atom assuming a gas temperature of $10^4$ K. The errors in the density measurements were calculated using the 1 sigma uncertainty in the line ratio. The difference between the densities at these extremes and at the nominal value are the reported density uncertainties. If either the nominal or 1σ [S II] line ratio was greater than 1.41 the density was assumed to be $n_e \leq 10$ cm$^{-3}$ (the low-density limit).

The electron gas temperature $T_e$ was also calculated at each position, from the

dereddened [O III] (λ5007+λ4959) / λ4363 ratio again using the IRAF/STSDAS nebular task. The density used in the calculation is from the [S II] lines. Error bars were computed in the same way as for the density values.

### 3.6 A Publicly Available Data Set

The Blanco instrument setup was chosen to cover the strong optical nebular emission lines from 4100 to 7400 Å including Hβ, Hα and the [S II] doublet at λλ6716, 6731. The Blanco observations were made in the form of a grid with fairly regular spacing which allow the data to be turned into a 'data cube'.

Our Blanco slit positions were chosen to produce a relatively unbiased sample of the diffuse emission as well as to include discrete structures of interest. Post-observing verification of the location of each slit position on the sky was done using narrow band emission line and continuum images taken at the SOAR telescope by (1) comparing the extracted surface brightness profile of Hα along the slit to the Hα images, (2) using positions, measured from our narrow band continuum images, of stars purposely placed in the slit as references and (3) where necessary using 2D nebular features visible in both the spectra and images as seen in Figure 2.4.

Table 2.4 is a sample of the final data product from the Blanco spectra. It lists the dereddened line strengths and several additional parameters for each extraction window along each slit position, and their uncertainties. The whole table, which is available electronically, includes measurements at 4238 positions with one row per position. Column 1 lists the slit position number (as used in Figure 2.1 and Table 2.2). Columns 2-4 contain the RA and Dec offsets in arcsec from R136 and the central pixel row of the extraction window along the slit. Then columns 5-10 list the electron density and its 1σ

uncertainty limits, followed by the electron temperature with its 1σ uncertainties.

Column 11 is the reddening $A_V$ deduced from the Hα/Hβ ratio. These are followed in columns 12 and 13 by the dereddened Hβ surface brightness and its 1 uncertainty. The remaining 44 columns list, in pairs, the dereddened surface brightness of each measured emission line relative to Hβ and the corresponding uncertainty.

The last three rows of Table 2.4, collectively labeled position 38, list the average properties of 30 Doradus derived from the entire data set. Position 38 row 1 is the average of the dereddened fluxes, and the physical properties derived from those. Row 2 is the average of the observed values. Row 2 was then dereddened using the average Hβ and Hα fluxes to produce row 3. Rows 2 and 3 represent the global spectroscopic properties that would be measured for 30 Dor if it were spatially unresolved.

Table 2.5 is the similar data product from the SOAR spectra, computed in exactly the same way as for Table 2.4. The SOAR spectra are presented in a separate table because there are a different number of columns due to the additional emission lines which were measured, including [S III] λ 9069. The ratio [S III] λ9069 / λ6312 is sensitive to the gas temperature like ([O III] λ 5007 + λ4959 ) / λ4363. The temperatures measured from the [S III] lines are included in Table 2.5.

In addition to the tabulated data the fully reduced Blanco 2D spectra, noise and calibration frames are publicly available. They currently are posted on a permanent web site at the Michigan State University Department of Physics & Astronomy[6]. The complete version of Tables 2.4 and 2.5 will be available in electronic form at that site,

[6] http/www.pa.msu.edu/astro/thesis/pellegrini/30dor/

and on the publisher's web site when this current paper is published.

## 4 Observational Results

### 4.1 Overview

Figures 2.7a-f are maps of selected emission lines, nebular diagnostics, and physical conditions derived from those emission lines, interpolated in the spatial plane of the Blanco data cube. The two extreme slit positions, 16 and 17, are excluded from these maps. These maps are rotated 13 deg with respect to the N-S and E-W directions, and are labeled with offsets in that rotated coordinate system. An outline of the area covered by these maps is shown on Figure 2.1.

Figure 2.7a shows the dereddened Hα surface brightness and demonstrates the effective resolution of the grid interpolated from the 'data cube'. It can be compared with the SOAR Hα image in Figure 2.1. Most features, including the bright arcs centered around R136, are visible. To the east the cavity-like region of low surface brightness as well as the bright rim on its eastern edge are clearly seen.

Figure 2.7b maps the reddening $A_V$ as measured using the observed Hα/Hβ intensity ratio. As noted above, we used a simple Galactic reddening law to describe what is a really a more complicated situation in which the line of sight to 30 Dor passes through both the LMC and the Milky Way. With the exception of the region 80 arcsec south of R136, the overall smoothness in $A_V$ over the nebula suggests there are no large scale obstructions along the line of sight.

The ionization level of the gas is traced by intensity ratios which include ([O III] λ5007)/Hβ (Figure 2.7c) , ([N II] λ6584)/Hα (Figure 2.7d), ([S III] λ6312)/([S II] λ6716 + λ6731) (Figure 2.7e), and [S II]/Hα (Figure 2.7f). Figure 2.7f, shows the ratio derived

from the Blanco spectra, as opposed to the ratio made from the SOAR images that is shown in Figure 2.2. These line ratios all show a rough circular symmetry around a point about 40 arcsec E of R136. The same distribution was identified by Indebetouw et al. (2009; I09) using a Spitzer Space Telescope survey of 30 Dor using higher ionization lines. This will be discussed further below.

Figure 2.7g plots the electron density measured from the [S II] λ6717/λ6731 doublet ratio. In this plot various structures seen in emission lines are also detected. The brightness enhancement to the east of R136 $\Delta RA$ = +200 arcsec is visible a density enhancement. The region around the central cluster has a density almost an order of magnitude higher than the bulk of the nebula. Using the published contour plots of log $n_e$ derived from [S III] in I09 we compared the electron densities measured from [S II] and [S II]. We find they agree to 0.1 to 0.2 in log $n_e$, noting that the increments in the density contours of I09 are 0.1 in log $n_e$.

### 4.2 The [O III] Gas Temperature

The electron gas temperature is mapped in Figure 2.7h. It is computed from the [O III] (λ5007+λ4959) / λ4363 ratio . We find the nebula to be fairly isothermal within a few thousand degrees, in the range 9,000 ≤ $T_e$ ≤ 12,000 K for the cases with error bars smaller than 10 percent. The regions of hotter emission tend to be of lower density, as is expected since the the cooling rate of a plasma is proportional to square of the density. The accuracy of the overall scale for the gas temperature will be an important point in our analysis. Here we compare our mean [O III] temperature to that found by Krabbe & Copetti (2002), who used three long-slit spectra which criss-crossed the central region of

*30* Dor with much of their length falling on the bright arcs.

There are a number of valid ways to calculate an average temperature $<T_e>$ for 30 Dor. For the most direct comparison to distant, unresolved GEHRs, we should spatially integrate, over the whole nebula, all of the light in each emission line, then apply a single reddening correction based on the ratio of the spatially integrated Hα and Hβ fluxes. From those reddening-corrected line strengths we can then find $<T_e>$ using the observed [O III] (λ4959 + λ5007) / λ4363 ratio $R_{OIII}$ given by

$$R_{OIII}=\frac{\int F(4959\,\mathring{A}+5007\,\mathring{A})\,d\Omega}{\int F(4363\,\mathring{A})\,d\Omega} \quad . \tag{5}$$

This method uses the total line fluxes listed for Position 18, row 3 in Table 2.4, and yields an equivalent temperature of $<T_e>$ = 10,680 K +/- 5.0 ($R_{OIII}$ = 172).

An alternative is to use [O III] line fluxes that have first been individually dereddened at each point on the nebula and then spatially integrated. That method leads to $<T_e>$ = 10,760K +/- 8.0 ($R_{OIII}$ = 167.5). This corresponds to the values listed for Position 18, row 1 in Table 2.4. While the 1% difference between the results of these two methods is statistically significant, it is much smaller than typical observational errors for more distant extragalactic H II regions with measured [OIII] λ4363.

When individual measurements of $T_e$ have been made at multiple locations in a nebula, as is the case here, another common approach is to compute

$$\langle T_e\rangle=\frac{\int T_e(\vec{r})\times F(H\beta)\,d\Omega}{\int F(H\beta)\,d\Omega} \quad , \tag{6}$$

*where* the $T_e$ is weighted by the Hβ flux at each position. Using this method we find $<T_e>$ = 10,680K +/- 8.0, equivalent to $R_{OIII}$ = 172.

For comparison, using this last method, Krabbe & Copetti (2002) found $<T_e>$ = 10,270K +/- 46.7 ( $R_{OIII}$ = 194.5) using measurements along all three of their slit positions. An even lower $<T_e>$ = 9990K was found by Tsamis (2003) who summed over the length of a 160 arcsec slit.

To explore the source of the discrepancy between these values from other others and our measurement of $<T_e>$, we coadded all of our Blanco spectra to produce a single 1D composite spectrum, excluding only the regions containing the brightest stars. The entire spectrum was then dereddened as in the first of the averaging methods described above. We then measured $R_{OIII}$ and computed the associated $<T_e>$ from this high signal/noise ratio spectrum in several ways. Using our automated line measuring software on this spectrum produced $<T_e>$ = 10,565 K ($R_{OIII}$ = 179), in reasonable agreement with the value $<T_e>$ = 10,680 K obtained from the first of the averaging methods described above. The automated software fit the continuum in windows covering the wavelength ranges λλ4280-4325Å (blueward of Hγ) and λλ4410-4150 (redward of [O III] λ4363). A manual measurement of the [O III] line strengths using the IRAF *splot* routine and similar continuum levels produced essentially the same $R_{OIII}$ and $<T_e>$, verifying that our automated routine works correctly. However, inspection of the coadded spectrum showed that the region between Hγ and [O III] λ4363 is partly filled in by a faint plateau due to line wings or weak emission, and that the continuum also has complications in the

region around [O III] λ4959 and λ5007. We tried various choices of how to draw in the continuum and were able to measure line strengths corresponding to a temperature as low as $<T_e>$ = 10,280K ($R_{OIII}$ = 194). We surmise that the value $<T_e>$ = 10,270K found by Krabbe & Copetti (2001) agrees with our corresponding value $<T_e>$ = 10,673K to within these measurement uncertainties. Our automated process is an objective and repeatable technique, and we conclude that it returns temperature measurements that are as accurate as the data allow.

### 4.3 Ionization Mechanism

The observed gas temperature provides an important constraint to the energy sources that ionize the gas. The violent history of 30 Doradus is evident in the diffuse X-ray emission that is present throughout the nebula (Townsley et al. 2006), as well as in the high velocity expansion features with speeds up to 200 km $s^{-1}$ seen in Hα emission (Chu & Kennicutt 1994). These show that supernovae and strong winds from massive O and WR stars have combined to heat gas to the observed 3.5 – 7×$10^6$ K temperatures derived from Chandra X-ray spectra. Despite these indications of high-velocity flows, the moderate $10^4$ K temperatures in the ionized gas do not indicate shock heating as the current source of ionization. Additionally there is no detection of O IV or Ar V emission lines (Lebouttler et al. 2008), nor are there any significant detections of nebular He II emission which would indicate strong shocks being responsible for the ionization structure in 30 Doradus.

Instead, photoionization is implied as the energy input mechanism. This is assumed in our further analysis in this paper.

### 4.4 Temperature Fluctuations

Temperature fluctuations in nebulae are usually invoked to explain the observed differences in chemical abundances determined empirically from collisionally excited lines, and those measured using emission lines formed by recombination (Peimbert, 2003; P03) and also those found using the strong-line techniques discussed below. 30 Doradus is a nearby, resolved example in which temperature variations can be directly measured, as a point of comparison for what may happen in distant unresolved GEHRs. The 1D spatial profiles of $T_e$ and $n_e$ along each of our slit positions are shown in Figure 2.8. For clarity only every fourth error bar is shown. The electron temperature is presented on a linear scale and the density measurements on a $\log_{10}$ scale. For slit positions 1–17 positive displacement is toward the North, and for 18–37 it is to the East. An artificial lower limit of $\log_{10}(n_e) = 1$ was used as a lower limit to the density measurements. It can be seen that in many places where the error bars are small there are obvious 1000+ K fluctuations in $T_e$ over distances of tens of arcsec along the slit. Krabbe & Copetti (2002) used their long-slit spectra to measure the [O III] temperature fluctuations $t^2$, formally defined as

$$t^2 = \frac{\int (T_e - \langle T_e \rangle)^2 n_i n_e dV}{\langle T_e \rangle^2 \int n_i n_e dV} \quad . \tag{7}$$

They reported $t^2 = 0.0025$, using the approximation

$$t^2 \leq \frac{\int (T - \langle T_e \rangle)^2 F(H\beta) d\Omega}{\langle T_e \rangle^2 \int F(H\beta) d\Omega} \quad . \tag{8}$$

with $<T_e>$ as defined in Eq. 7 and after correcting the observed value for their

observational uncertainties. Working backwards from the information in their paper, we find $t^2 = 0.0035$ before their correction for observational errors.

The directly measured value from the Blanco data set, using Eq. 8, is $t^2 \leq 0.024$. After accounting for our error bars, this becomes $t^2 \leq 0.014$. This is considerably larger than the Krabbe & Copetti result. The Krabbe & Copetti slit positions sampled a much smaller area of 30 Dor than our data set and covered regions dominated by the bright arcs, which we find to be fairly isothermal. The fluctuations in temperature become much more significant when the distant lower density regions are included, as in our data set. However, we also note that in these fainter regions we have likely underestimated the error in our measurements because of the difficulty in measuring the [O III] λ4363 line. The large $t^2$ value that we measure here is very close to the value needed to bring abundances measured from collisionally excited lines into agreement with those measured from recombination lines. Unfortunately, we cannot be confident of this result due to the possibility of systematic errors in the continuum placement that might change with position along the slit.

### 4.5 Structural Details

The geometry and ionization structure of 30 Dor is quite complex. The SOAR direct images provide a powerful tool for distinguishing edge-on ionization fronts, regions ionized by localized sources of radiation besides R136, edge-on IFs, optically thick pillars like those found in M16 (Hester 1996), and line-emitting foreground structures. In particular, the nearly reddening-free [S II]/Hα image (Figure 2.2), formed from the ratio of the SOAR images in those two passbands, offers considerable insight into the

*ion*ization structure on many scales.

### 4.5.1 Embedded ionizing stars

A key question is the degree to which R136 dominates the ionizing radiation field at different positions in the nebula. This will depend on the extent to which additional, isolated O stars provide local contributions to the radiation field. Such stars can be recognized by localized, circular variations in the ionization level as indicated in the [S II]/Hα maps, in combination with brightness enhancements in the Hα emission. We carefully searched the SOAR images for such features, and located the 49 isolated ionizing stars listed in Table 2.6. Some percentage of these are likely to have been selected by chance, so this estimate should represent an upper limit to the number of locally ionizing stars. The area of the nebula in which the ionization level is significantly affected by the radiation field of these stars, as projected on the sky, covers only 2% of the full nebula, so is unimportant in our analysis below of the overall properties of the nebula.

### 4.5.2 Edge-on ionization fronts

Edge-on ionization fronts stand out in the [S II]/Hα image as narrow lines of high [S II]/Hα ratio butted up against regions of low [S II]/Hα For an edge-on IF to be detected in this way, the ionization parameter *U* must be high enough that the thickness of the ionized gas is spatially resolvable, and the density must be high enough that the optically thin Hα emission is distinguishable from background emission. Where this is true, the Hα emission is separated from the [S II] emission and the edge-on IF is detected as an inversion in the [S II]/Hα ratio, with lower values found on the side toward the ionized

gas and higher values toward the IF.

Table 2.7 lists prominent, isolated, edge-on ionization fronts found in both our [S II]/Hα image and the Spitzer 8μm PAH mosaic. These unobstructed IFs are perfectly suited for detailed, high angular resolution (e.g. with HST and/or ALMA) studies of the neutral and molecular gas beyond the IF, commonly called the Photon Dominated Region (PDR). A finding chart with the all IFs listed in Table 2.7 is shown in Figure 2.9. Two examples of such features, IF1 and IF2, are shown in an inset in the upper corner of Figure 2.9, which is a blow-up of a portion of the [S II]/Hα image shown in Figure 2.2. Visible in both IF1 and IF2 is the spatially resolved layer of $H^+$.

IF1 and IF2 are likely to be similar in geometry to the Orion Bar (see P09), and enough information can be measured about them to provide a test of whether or not they are likely to be photoionized by R136. The thickness *dr* of the ionized gas depends on the density and distance $r_0$ from the source of ionizing radiation according to

$$dr \propto Q_0/(4\pi\,\alpha\, n_e n_p r_0^2) \quad . \qquad (9)$$

where $\alpha = 2.59\times10^{-13}$ cm$^{-3}$ s is the $H^+$ recombination rate.

There is a line of stars coincident with IF1 that could be an alternative to R136 as the source of ionization, or which could be stars formed in a region of gas that was compressed by radiation and wind pressure from R136, or which could simply be foreground stars. Most of these stars fell in one or another of our slit positions. We have examined their spectra and found them to lack any absorption features that would indicate they are massive stars. With the exception of one star, they do not appear to be particularly reddened, suggesting they are not embedded in or around the IF.

Additionally, we note that the overall structure of IF1 is oriented almost exactly perpendicular to the direction to R136. There are also many prominent pillars in this region (see below), all pointing back up to R136, suggesting the nearby stars are unimportant to the structure.

Our SOAR spectrographic slit position number 40 cuts directly across the large ionization front IF1, avoiding the pillars noted by Scowen (1998) and targeting the larger structure. The emission line strengths in the region of IF1 were measured as described above, but were extracted in smaller (0.75 arcsec) windows along the slit to better resolve the detailed structure. Figure 2.10 shows the profile of IF1. In the top panel are the relative intensities of Hα, [O III] λ5007 and [S III] λ9069 which trace highly ionized gas. The middle panel shows the same for [S II], [O II] and [N II], all tracers of the IF. The bottom panel shows the linear density profile of the structure in $cm^{-3}$. At the illuminated face the structure has an electron density $n_e \leq 100$ $cm^{-3}$, increasing to 800 $cm^{-3}$ at the peak of the [S II] emission, and then decreasing to a minimum of 200 $cm^{-3}$.

There is a bright knot in the [S II] images at the location of the peak density. Excluding this point, the density at the IF is likely to be 560 $cm^{-3}$. Using this density, and assuming that R136 is the ionizing source, that the 13.6 pc (58 arcsec) projected distance from R136 is the true three-dimensional distance and that the 1.18 pc projected thickness of the $H^+$ zone is the true thickness, Eq. 9 requires $Q_0 = 5.9 \times 10^{51}$ $s^{-1}$. In addition to the uncertainties in projected vs. true distances, this value does not include the effects of absorption by He and neglects the effect the observed gradient will have in lowering the measured average $n_e$, so the derived $Q_0$ could be either too low or too high. However, it is

still interesting to compare this estimate based on our measurements of IF2, to $Q_0$ estimates for other edge-on ionization fronts at varying distances from R136, as a test of the hypothesis that R136 is the predominant source of ionizing radiation.

IF2 is the inner edge of one of the most prominent bright arcs, located at a projected distance of 17 pc (70 arcsec) NE of R136 (see Figure 2.1) . The thickness of the $H^+$ layer perpendicular to the direction to R136 is approximately 0.94 pc. Within the observational error the density at the IF along a ray from R136 into IF1 is $n_e = 280$ cm$^{-3}$. Applying Eq. 9 with the same assumption used with IF1, we find $Q_0 = 2.0 \times 10^{51}$ s$^{-1}$.

IF4 is a bright rim lying much further out in the nebula, 220 arcsec (53 pc) to the east of R136 on the far side of the large faint low-density region that is easily seen in figures 2.7a-e. This large wall is remarkably homogeneous in density and has a thickness between 3.5 and 4 arcsec all along its length of 140 arcsec (33 pc). The limb shows up as a density enhancement in Figure 2.7c, with $n_e = 125$ cm$^{-3}$. It has a nearly constant projected distance from R136. Using the previous technique we find $Q_0 = 4.58 \times 10^{51}$ s$^{-1}$. We will return to this particular IF in the Discussion section below.

The above estimates of $Q_0$ for R136 are all in reasonable agreement with each other and also with $Q_0 = 4.2 \times 10^{51}$ s$^{-1}$ estimated by Crowther and Dessart (1998) from adding up the contributions expected from the individual stars in the cluster. These results support the conclusion that R136 dominates the ionizing radiation field throughout most of the volume of 30 Dor that is included in this present study.

However, there is at least one counter example, to the SW of R136 where the observed structure indicates a different ionization source. IFs 1*-5* show PAH emission *closer* to

R136 than the [S II] emission. Forming an elongated shell structure with a diameter of 15 pc around another star cluster, thes IFs and likely to be ionized by it.

### 4.5.3 Dense pillars

There are numerous bright fingers and protruding IFs scattered over the face of the nebula, but particularly concentrated in the region SW of R136. Many of these are probably elephant trunks similar to the famous "Pillars of Creation" in M16. A small number of these have been commented on by Scowen et al. (1998). 106 of the brightest such features are cataloged here in Table 2.8 with RA and Dec positions, projected length and PA, but there are hundreds more that blend together as one looks on finer and finer scales, until they are indistinguishable from small examples of the edge-on ionization fronts discussed above. Almost all of these point back to R136, again showing that the central cluster is the dominant source of ionizing radiation.

Many of these features are clearly connected to larger bodies of molecular gas, as can be seen by comparing our [S II]/Hα ratio image to the 8μm image from the Spitzer Space Telescope archives, which shows PAH emission (Figure 2.11). However, some of them do appear to be isolated tubes or blobs of gas rather than protrusions from background walls of molecular material. Scowen (1998) have commented on one bright structure of this latter type. Some of these might correspond to the expanding shells seen in Hα emission in the high-resolution echelle spectra of Chu & Kennicutt (1994).

## 5 Photoionization Simulations

### 5.1 Rationale and Purpose

As discussed above, the observed emission line intensity ratios and morphology indicate photoionization from a central source as the dominate process energy source. The general

radial symmetry of these ratios around a point on the sky near R136 (Figs 2.7a-g) strongly suggest that central cluster is the major source of this photoionization. The center of these circular patterns is offset to the east of R136, but that can be immediately understood as being the result of a blowout into the lower density gas toward the east (fig 2.7g), very similar to what is seen on a smaller scale in M17 (P08) The identification of R136 as the source of ionization is supported by the lack of strong competition to the stars within 15 pc of R136 from local ionizing stars (Sect. 4.5.1), by the thickness of edge-on ionization fronts as a function of distance from R136 (Section 4.5.2), and by the large numbers of elephant trunks pointing back towards R136 from points all over 30 Dor.

In order to estimate $U$ at different locations within 30 Dor, we computed a grid of photoionization simulations as a tool for using the observed emission line strengths to determine $U$ and other physical conditions in the gas on a point-by-point basis across the nebula. The purposes of this grid of photoionization simulations are (1) to determine the shape of the ionizing continuum radiation field assuming that most of the gas is photoionized by the same source (R136); (2) to fix the global chemical abundances, as averaged over the full nebula; and (3) to provide a look up table that can be used to determine $U$ and $n_e$ at each point in the extended nebula.

### 5.2 Basic Simulation Parameters

We used the plasma simulation code Cloudy (Ferland et al. 1998). All of the models described below begin at the illuminated face of a plane parallel cloud, externally illuminated by a source of ionizing radiation with an incident flux $Q_0/(4\pi\, r_0^2)$.

For simplicity, we assumed a constant-density equation of state (EOS). The EOS may be

approximated by equation A2 in P09. The constant density assumption used here affects the relative densities of the $H^+$, $H^0$ and $H_2$ regions. When only considering the $H^+$ region the gas temperature is nearly constant and the differences between equations of state become minimal. As a result, the relative strength of the emission lines formed in the H II region are largely unaltered by the EOS.

All of our models assume the physical thickness of the gas cloud to be 10 pc (which projects to 43 arcsec at the distance of 30 Dor). The physical thickness of the $H^+$ zone will change as described by Eq. 9 in response to changes in density and ionizing flux. In cases where the ionized layer extends to a depth greater than 10 pc, the cloud was treated as matter bounded (the 'optically thin' case). In the model fitting described below, this happened only in a few regions close to R136. Elsewhere, the ionized layer is radiation bounded ('optically thick'), in which case the models were stopped when their temperature reached 500 K. At this temperature the ionization front has fully formed, but the models have not gone into the PDR.

For the optically thick models, the computed emission line strengths correspond to what would be seen if the ionized cloud were viewed face-on, so that the emission coming from all depths into the $H^+$ zone was added together. This would simulate either gas seen on the ionized back surfaces of a large bubble (similar to our view of the main part of the Orion Nebula, for instance), or what would be seen for a more edge-on IF with a sufficiently small ionized thickness so that the full depth of the $H^+$ zone fit into one of our 1D spectral extraction windows. For the Blanco spectra the extraction window was 2.5×3.5 arcsec, corresponding to 0.6×0.8 pc. The ionized layer in gas with a typical

density $n_H = n_e = 200$ cm$^{-3}$ and lying more than 50 pc (200 arcsec) from R136 would fit within one of these extraction windows.

For the optically thin case the models do not reflect a particular geometry. Instead they represent a fully ionized zone which is matter bounded. These are indicated by regions with very weak emission from IF tracers like [N II] λ6584 and [S II] (λ6716+λ6731) relative to H recombination lines. For matter bounded nebulae the strengths of these IF tracers are typically 1/10 Hα. Line ratios characterizing a fully ionized plasma with no IF are an order of magnitude lower than this. Our models of these regions follow the radiation transfer through a 10 pc thick region. However, these models assume illumination by an unfiltered ionizing spectrum, which would not be realistic if the observed gas is part of an ionized region larger than the area taken in by the slit. To deal with this additional complication we would need prior knowledge about the geometry to reconstruct the entire $H^+$zone, which is what we are trying to work out. Despite the lack of total realism, the optically thin models are still useful since the line ratios are most sensitive to ionization parameter and not thickness.

We estimated the numbers by spectral type of massive O and WR stars in the central cluster by using SIMBAD to find all stars within 45 arcsec of R136 with spectral types (Table 2.9). Using the conversions from spectral type to ionizing flux and effective temperature $T_{eff}$ given by Vacca et al. (1996) for the O-stars and Crowther (2007) for the WR stars, the corresponding luminosity of ionizing photons generated by the central cluster is $Q_0 = 7\times10^{51}$ s$^{-1}$ . This is slightly above the value $4.2\times10^{51}$ s$^{-1}$ estimated by Crowther and Dessart (1998) for all of R136. Using the stellar atmosphere parameters

given by Heap, Lanz & Hubeny (2006) would reduce our computed $Q_0$ by about a factor of two. Fixing $Q_0$ means that in our models the incident ionizing flux was determined by $r$, the distance from R136.

The global X-ray emission in 30 Dor is well studied (Townsley et al. 2006) and found to show considerable surface brightness structure and to have plasma temperatures between 3 – 9 million deg. However, the X-rays are unlikely to significantly affect the ionized gas, since the X-ray luminosity is three orders of magnitude lower than the UV ionizing luminosity $Q_0$ from the stars. We have compared models with and without likely X-ray fluxes and conclude that for models of the $H^+$ region the X-rays can be ignored.

The models include silicate and graphite dust using the average LMC size distribution from Weingartner and Draine (2001). We have assumed a quite small dust/gas ratio. To first order the gas to dust ratio is expected to scale with metallicity, where the gas to dust ratio in the LMC is equal to the gas to dust ratio near the Sun times the ratio of metallicity of the LMC to the Sun, $Z/Z_\odot$. We have adopted a lower gas to dust ratio is equal to 0.1 $Z/Z_\odot$. This choice is motivated by the lack of correlation between FIR emission and $A_V$ (Chu et al 1985). The hypothesis that the extinction is caused by foreground dust is further supported by the similarity of $A_V$ shown in Figure 2.8b to that measured along the line of sight to the stars. Recently a study of the dust to gas ratio in the LMC was carried out in the IR, using heavily extinguished lines of sight though molecular clouds (Dobashi et al. 2008). IR colors of stars behind molecular clouds were used to measure $A_V$. $A_V$ was compared to the hydrogen column density $N$(H) of the

molecular clouds, where $N$(H) is the sum of neutral H traced by H I 21-cm maps (Kim et al. 2003) and $H_2$ traced by $^{12}CO$ maps using a common conversion factor between $N($ $^{12}CO$ ) and $N(H_2)$. Using the ratio of $A_V/N$(H), the relative amount of dust in the LMC was found to vary between 8.5 and 2 times smaller than the solar value. There is a trend toward 30 Dor for the ratio to increase, but this may be the result of an undetected gas component in that direction. As a result the gas to dust ratio we have assumed for our HII region is about half the lower value found in the molecular clouds in the LMC. This is not to say that there is no significant amount of dust outside the highly ionized region. In the Spitzer images the correlation between the more easily destroyed PAHs and the H$\alpha$ emission is very strong, but separated spatially as in more quiescent H II regions. Since PAHs are more fragile than dust, the dust must also be present in significant quantities outside the H II region. We only suggest a lower dust abundance in the $H^+$ zone itself due to the extreme nature of the cluster.

We have assumed a constant turbulent velocity of 5km $s^{-1}$ .This does not affect the pressure and is included only for a realistic treatment of the radiation transfer.

### 5.3 Initial Chemical Abundance Set

The chemical abundances in 30 Dor have been studied extensively. Historically this has been done using optical spectroscopy, which has access to a great number of elements and is easily obtained from the ground. Empirical total gas phase abundances are determined by using either a recombination or collisionally excited emission line relative to a hydrogen recombination line, often using the ($\lambda$4959+ $\lambda$5007)) / ([O III] $\lambda$4363) ratio to estimate the gas temperature. The relative intensities of emission from a given ion

provide an accurate measure of the relative ionic abundances. The total abundance is measured by observing emission from all the dominant ionization states or by making an ionization completeness correction to account for ionization states not observed. Some key studies of this type are by Vermeij et al 2002 (V02), Mathis, Chu & Peimbert 1985; Rosa & Mathis 1987; Tsamis et al. 2003; and P03).

A more complicated, model-dependent alternative is to use photoionization codes to account for emission from all ionization states simultaneously. There is significant difficulty in breaking the degeneracy of models with different *U*, abundances and SED. Studies of this type have been carried out by Tsamis & Pequignot (TP05) and Lebouteiller et al. 2008.

As a starting point for our simulations, we drew on the results of TP05. They assembled a set of observed emission line strengths by combining published results from UV (V02), optical (P03) and IR Spitzer (V02) spectroscopy, and then used exceptionally detailed photoionization simulations to determine the total gas-phase abundances of 30 Dor. They concluded that at the spot in the nebula they were studying, a multiple component model is required, in which two gas components with different chemical abundances, densities and temperatures are in pressure equilibrium. One component represented low-temperature high-density filaments that are H and He poor, consistent with wind-blown material from pre-SN winds. We adopt here the abundances from their other component, representing the homogeneous surrounding material, because the filaments would contribute less than 10 percent of the total emission in most of the emission lines that we are studying. The abundances for the homogeneous component of TP05, their model D2, are listed in Table 2.10, along with other empirical and model-based abundances. The

abundances quoted from P03 are those derived assuming a mean square temperature fluctuation $t^2$ =0.003. We take the scatter between these methods to represent the range of uncertainty in the abundances in 30 Dor. The last line of Table 2.10 lists the abundances which we determine here, as described below.

Our initial set of simulations used CLOUDY with the same abundances and the same COSTAR (Schaerer et al. 1996) stellar atmosphere (an atmosphere with half-solar metal abundances and an effective temperature of 38,000 K) that was used by TP05 in their model D2, to compute a grid of models in which we varied the incident ionizing flux and the gas density. We then iterated to a final choice of ionizing continuum shape and chemical abundances as described below.

### 5.4 The Ionizing Continuum Shape

We first explored the degree to which the ionizing continuum shape is constrained by the observed emission line intensity ratios and by their variation across the nebula.

Figures 2.12a-d show a set of diagnostic diagrams which compare observed emission line intensity ratios to the predicted ratios using COSTAR models of different $T_{eff}$. The assumption that the gas throughout 30 Dor is to first order all illuminated by the same continuum source gives these diagrams great leverage in identifying the shape of the ionizing continuum. In these figures, predictions and observations are shown only for cases with $100 \leq n_e \leq 200$ cm$^{-3}$. In Figures 2.12a, 2.12c and 2.12d, only SOAR observations could be used because not all of the necessary emission lines could be measured in the Blanco data set. The solid lines show results for CLOUDY grids with the density was fixed at $10^2$ cm$^{-3}$, and with an ionizing flux corresponding to distances

from the central cluster between $13 \leq r \leq 140$ pc. Multiple SEDs are a shown using the COSTAR continuum shapes ranging from $T_{eff}$ = 37,000 K to 41,000 K in 1,000 K steps, increasing in temperature in the direction of the arrow shown on each panel.

Figure 2.12a (top left) shows ([S II] λ6716+λ6731)/([S III] λ9069) vs ([O II] λ7320+λ7330)/([O III] λ5007), which is very similar to the radiation softness parameter originally defined by Vilchez & Pagel (1998). It is also nearly equivalent to the ratio of *S23/R23* where S23 and R23 are two widely used ratios to indicate abundances of O and S. R23 was originally purposed by Pagel et al. (1997) and is often used in strong line abundance measurements because it includes the strongest lines from the most abundance phases of O. This diagnostic is strongly dependent on the shape of the spectral energy distribution (SED) and on *U*, and is only weakly dependent on abundance and density. As the effective temperature of the modeled SED increases, the emission from the low ionization species relative to those with higher ionization potential decreases. It was demonstrated by Oey et al. (2000) that these line ratios are sensitive to effective stellar temperatures less than 40,000 K. As a result, the observational scatter in Figure 2.9a may be the result of observational error such as imperfect night sky subtraction of the [O II] lines or improperly corrected fringing in the [S III] line, or it may indicate real variability in the shape of the ionizing radiation reaching some points.

Figure 2.12b shows [S II]/Hα vs [O III]/Hβ and is often used to study large samples of different H II regions or emission-line galaxies. It was first proposed by Veilleux & Osterbrock (1987) as an additional way of separating H II regions from active galactic nuclei using emission lines, to supplement BPT diagrams (Baldwin et al. 1981). This diagnostic depends on the O/S abundance ratio as well as on the gas temperature and *U*.

Both the SOAR and Blanco data sets are used on this diagram.

Figure 2.12c is a diagnostic that includes the [O I] λ6300 line that comes from deep within the $H^+$-$H^0$ boundary zone and hence is a stringent test on how well our constant density models are fitting at the point of transition into the Partial Dissociation Region (PDR). Figure 2.12d is similar to Figure 2.12b except that it uses only O/H line ratios, thus removing the uncertainties concerning the O/S abundance ratio.

From the four diagnostic diagrams in Figure 2.12, we found that the best-fitting models using COSTAR atmospheres lie between the $T_{eff}$ = 38,000 and 39,000 K curves, so we ran a final grid using $T_{eff}$ = 38,500 K. The results for that grid, which is our best-fitting case using the TP05 abundances, are shown on Figure 2.12 as a heavy dashed line. The fit to the ridge line of the observations is good except that the [O II]/[O I] ratio is under-predicted, meaning that [O I] is too strong in the models since other line ratios involving [O II] give good fits. It is important to note that the [O II] line strength used on these diagrams is λ7320+λ7330, *not* the much more commonly-used λ3726+λ3729.

We also tried fitting a grid of WMBASIC models (Pauldrach 2001) of different temperatures. These stellar atmosphere treat the radiation transfer including line absorption by metals, and as a result produce a significantly softer continuum shape. They gave poor fits on to the [S III]/ [ SII] data from the SOAR observations and were dropped from further consideration. As a further possible continuum shape, we constructed a composite continuum made by adding together WMBASIC models at different temperatures weighted by an the number of stars of each spectral type as listed in Table 2.9.

### 5.5 Revised Chemical Abundances

The above exercise led us to adopt a COSTAR $T_{eff}$ = 38,500 K model as a reasonable approximation to the ionizing continuum shape produced by R136. This model gave an acceptable fit to the line ratios shown on Figure 2.12.

However, the resulting CLOUDY models significantly under-predict the observed electron temperatures $T_e$. This can be seen by comparing the predicted [O III] λ4363/ λ5007 ratio to the observations, as is shown in Figure 2.13. TP05 computed the average model temperature weighted by the $H^+$ density to be $<T(n(H^+))>$ = 9895 K. Using the same initial conditions our typical model produces $<T(n(H^+))>$ = 9310 K with the same weighting. Both of these temperatures are significantly lower than our measured $<T_e>$ = 10,270-10,760 K weighted by $F(H\beta)$ as in Eq. 6.

Since the temperature of an H II region is largely regulated by cooling through forbidden metal lines, and a harder SED is already ruled out, we conclude that the overall metal abundances found by TP05 are too high. Oxygen lines account for about 25% of the cooling in the various models described here, so the gas temperature is essentially set by the O/H abundance ratio. To arrive at a final set of models we first decreased the O/H abundance until the model temperatures increased to the observed value, leaving the other abundances unchanged (i.e. with the values used in TP05 model D02). The resulting O abundance is log(N(O)/N(H)) = -3.75, as shown in the bottom row of Table 2.10.

Since N, S and Ar do not dominate the cooling, their emission varies almost linearly with abundance. The abundances of these elements were adjusted so the models again

matched the emission line diagnostics used in Fig 2.12. The resulting adopted abundances for these elements are also listed in Table 2.10.

This model-based method of determining the global abundances in 30 Dor should be reasonably accurate for elements for which the atomic parameters are well known (i.e. elements from the 2$^{nd}$ row of the periodic table, including O and N from Table 2.10) and also for elements for which lines from more than one important ionization state are observed (O and S from Table 2.10). However, our abundance estimate for Ar is based on only one pair of emission lines from a single ionization state of this 3$^{rd}$ row element, and therefore is quite uncertain.

Finally, we also adjusted the He abundance to match the observed He I emission line strengths. The He I lines are due to recombination of $He^+$ which has well-known atomic data. The observations provide tight constraints on $N(He^+)/N(H^+)$. This should be nearly identical to N(He)/N(H). Our new observations do not detect any significant $He^{++}$ $\lambda$4686 nebular emission. This rules out a significant fraction of $He^{++}$. There exist many arguments (Pagel 1992, AGN3) that there should also be no $He^0$ coexisting with $H^+$. This is confirmed in all of our models, where a typical place in the nebula with $n_H = 10^2$ cm$^{-3}$ at a distance of 50 pc has an $He^0/He^+$ fraction of 0.009.

A comparison of the observations to the predicted intensity ratios from this final set of models, with the revised abundances, is shown in Figures 2.14-2.17. Figure 2.14 shows the much improved predictions of [O III] $\lambda$4363/$\lambda$5007 relative to observed values. Figure 2.15a-d is a repeat of Figure 2.12a-d, showing that the models fit just as well with

the revised abundances as with the TP05 abundances. Figure 2.16 shows the fit to He I λ6678/Hα, and Figure 2.17 shows the commonly used [N II]/Hα vs. [O III]/Hβ diagram. Agreement between the predictions and the observations is now good in all cases.

The final adopted abundances $\log_{10}$(N(X)/N(H)) are (H:He:C:N:O:Ne:Si:S:Cl:Ar:Fe) = (0:-1.08:-4.3:-4.91:-3.75:-4.36:-5.51:-5.32:-7.16:-5.99:-5.95). Here the abundances of all elements for which we did not measure line strengths were left unchanged from the values used in TP05 model D02. An alternative strategy might have been to alter the abundances of the unobserved elements in lockstep with the O/H abundance ratio. We verified that making that change did not alter any of the predicted intensity ratios shown in Figures 2.14- 2.17, or the values of *U* found in the following section, by more than 1%.

### 5.6 The Physical Parameters at Each Point in the Nebula

With the SED and chemical abundances now fixed, we fit the observations to a full grid of 987 CLOUDY models with varying distance $r_0$ from R136 and density $n_H$. The [S II] λ6716/λ6731 ratio, *S2r*, is primarily dependent on the gas density and offers a strong observational constraint in this procedure. We began with a grid spacing in density such that *S2r* varied by 1%. For each point in the nebula *S2r* was used to eliminate any model where

$$\left|S2r_{obs} - S2r_{model}\right| > 3\sigma_{obs} \quad . \tag{10}$$

This sub-grid of $n$, $r_0$ is like the original, but with fewer possible $n_H$. For each $n_H$ in the *S2r* selected sub-sample, we compared the models with different $r_0$ by a convergence criteria $\chi^2$ defined as

$$\chi^2(r_0, n_H) = \sum_i \left( \frac{R_{i\,obs} - R_{i\,model}}{\sigma_{obs}\, min\{R_{i\,obs}, R_{i\,model}\}} \right)^2 , \qquad (11)$$

where $R_{i\,obs}$ and $R_{i\,model}$ is the observed and modeled dereddened ratio of emission lines relative to Hβ. The emission lines with an asterisk in Table 2.3, as well as *S2r*, were used in the fitting. They were chosen because of their brightness, dependence on ionization parameter and the absence of contamination by night sky lines.

The $R_0(n)$ with the lowest $\chi^2$ was then used as the starting point for a search between neighboring models. Using linear interpolation along $r$ we found the $r_0$ which minimized $\chi^2$ for each n. Finally, the $n$, $r_0(n)$ pair with the lowest $\chi^2$ was selected as the best model for that particular data point. Over almost all of the nebula good fits were achieved w/ optically thick models. However, we do not claim that we have accurately described the relatively small region fitted by our optically-thin models – there is obviously some radiation transfer left out of that part of the fitting and there is a bright, obviously embedded star in this region which is very prominent at infrared wavelengths, which may be locally ionizing this relatively small part of the larger nebula.

The final result of this procedure was a grid of values of the fitted ionization parameter $U$ and electron density $n_e$ measured at every point along our slit positions. The resulting map of $U$ over the face of 30 Dor is shown in Figure 2.18.

## 6 Discussion

### 6.1 Photoionization by R136 vs. Other Sources of Excitation

We have fitted photoionization models to the measured emission-line intensity ratios at a large number of points across the surface of 30 Dor. This produces a point-by-point

estimate of the ionization parameter all across the nebula. This is very similar in outline to the recent study of a somewhat smaller region of 30 Dor by Indebetouw et al. (2009; I09), who used the strengths of emission lines measured with the Spitzer Space Telescope. A goal of I09 was to use variations in the shape of the SED photoionizing each part of the nebula to disentangle the relative contribution from local ionizing sources compared to the central cluster. The SOAR spectroscopic data used here allows us to estimate the effective stellar temperature using [O II]/[O III] and [S II]/[S III] ratios for a selected portions of the nebula, similar to way in which I09 used [Ne IV] /[Ne III] and [Ar III]/[Ar II].

I09 analyzed their infrared line intensity ratios using "one zone" Cloudy models, which we take to mean that they stopped the Cloudy integration through the ionized layer after the first zone, so did not include the effects of radiative transfer inside the gas cloud and instead fit all line ratios as if the gas were fully ionized. Such models cannot be expected to correctly reproduce the strengths of the low-ionization lines that are included in our observations. They allowed the SED in their one zone models to vary on a point-by-point basis, which presumably represents some combination of true variations in the intrinsic shape of the ionizing continuum, correction for the missing radiation transfer calculation within each gas cloud, and noise.

Here we have used more complete Cloudy models which properly predict lines from lower ionization species like [N II], [S II] and [O II] along with $H^+$, [O III] and [Ar III] so that the entire H II region is used as a constraint. We have also assumed that all gas clouds in 30 Dor see the same ionizing continuum source, and have neglected any filtering of that radiation by any intervening gas within the 30 Dor nebula. We deduce

from the derived parameters that this is a reasonable approximation in most parts of the nebula. A quantitative comparison of our results to the ionization parameters found by I09 is not possible because their published results are only descriptive. Qualitatively, the the ionization parameter maps determined here from our optical data are in reasonable agreement with the results I09 derived using their IR data.

The dominance of the X-ray emitting gas in the equation of state is a validation of our constant density/models, which show the integrated radiation pressure to be negligible on global scales. This is in contrast to the results for the smaller H II regions M17 and the Orion bar which we have previously studied in detail (P08, P09). While the radiation pressure from the stars is negligible over much of 30 Dor, we find excellent agreement between photoionization models and our observations for the entire region. Within the constraints of our data we find the emission line spectrum is set by photoionization from the central cluster. We have identified regions that are suitable for follow up that may be locally ionized, but they are quite limited in number. The additional constraints provided by further optical [S III] and [O II] observations should in the future allow the nature of those regions to be firmly established. By considering the entire system, we conclude that the approximation of a single ionizing source is a sufficient description for the complicated 30 Dor region, and hence of similar regions that may be unresolved in distance galaxies.

### 6.2 The Current Geometry of 30 Dor

The projected structure of 30 Dor as seen on an Hα image such as Figure 2.1 is dominated first of all by the very bright arcs near R136, and after that by the extensive regions of low surface brightness which have the appearance of large cavities and are

often referred to by terms such as "merged supernova remnants".

Our Cloudy model fitting shows that all of the regions of higher Hα surface brightness are optically thick to ionizing radiation; this is determined most clearly by the observed [S II]/Hα intensity ratio but all of the other measured lines bolster the result. Spitzer images (Meixner 2006) show that there are extensive regions of PAH emission associated with most of these same regions, verifying that a transition zone into molecular gas is associated with them.

CO maps (Poglitsch 1995) show that the main bulk of the molecular gas falls in a broad N-S swathe that includes the region of the bright arcs. Direct near-infrared narrowband images (Rubio & Probst, unpublished) and also long-slit infrared K-band spectra that we have obtained with the SOAR Telescope show emission in the $H_2$ 2.12 μm line coming from extensive regions on the opposite sides of the bright arcs from R136. This all combines together to very clearly show that the bright arcs are edge-on walls of molecular clouds whose faces are being photoionized by R136.

In Section 4.5.2 we have cataloged a number of other examples of similar walls, but at greater distances, which also are photoionized primarily by R136.

The remainder of the surface area on 30 Dor that our model-fitting identified as optically thick gas is a mix of smaller, often blended edge-on ionization fronts (Figure 2.2), along with broad surfaces of optically-thick gas seen more nearly face-on. This latter gas must lie further away from us than R136 if it is indeed photoionized by direct radiation from R136.

Turning to the "cavities", Townsley et al. (2006) showed from Chandra Space Telescope maps that there is a correlation between X-ray emission and these regions of low Hα

surface brightness, and argued that the correlation between these structures implies that the cavities are supported by the pressure of the hot X-ray gas. We explored the possibility that the optical emission lines in these directions were coming from optically thin inclusions of warm ($10^4$ K) gas somehow surviving within these cavities. However, we find that the optical emission from only a fairly small portion of only one of these regions is actually fitted by optically thin models. Over most of the regions of low H$\alpha$ surface brightness the optical emission lines are from optically thick gas, which we interpret as coming from an optically thick back wall.

This all shows that, as has long been realized, the optical emission from 30 Dor traces a very layered, three-dimensional structure. We know the projection on the sky (the $x$, $y$ coordinates) of the observed features. We now use the results from our photoionization model fits to quantify as much as possible the shape and positions of these structures in the line-of-sight ($z$) direction.

The model-fitting returns a three-dimensional distance $R_{model}$ between the ionizing source R136 and the gas cloud in question. We can compare this to the projected distance $r_{projected}$ to estimate $z$, the difference between the line-of-sight distance to the gas cloud and the line-of-sight distance to R136. We use

$$|z| = (R_{model}^2 - r_{projected}^2)^{1/2} \quad . \qquad (12)$$

Our Slit Position 8 passes very near to R136 and through the bright arcs associated with IFs 2 and 3, which are to the NE and SW of R136 (see Figure 2.9). Figure 2.19 a map of the fitted z in units of pc at the top. The bottom of Figure 2.19 shows z along Position 8, plotted vs. the declination offset in pc from R136. Equation 12 does not constrain $z$ to be

positive or negative, but in the vicinity of R136 we can safely assume a face-on geometry where $z$ is positive (i.e. the gas is behind the cluster). This places the background gas 40 pc behind the central cluster. The sharp increase in $z$ at zero declination offset is an artifact due to contamination from the light of R136 at that point. The bright IFs 2 and 3, situated to either side of R136 at a projected distance of approximately 9 pc (40 arcsec), have $z \sim 0$. If the assumed $Q_0$ were 10 percent smaller they would have $z$ exactly equal to 0. Thus, within the uncertainty of $Q_0$, the IFs are at the same line-of-sight depth as R136.

A region N of R136 was identified by I09 to be of especially high excitation, and is also shown by our spectra to have a very high ionization parameter. This region is part of the bright arc to the NE of R136. I09 concluded that the high excitation was the result of local photoionization by a group of three WR stars which lie close to the IF at least in projection. If this were the case then the measurement of $z$ would be decreased due to enhanced flux from the WR stars. Our Slit Position 6 samples the IF part of the region of interest, but at a different location further from the possible influence of the WR stars mentioned by I09. At this position there are no obvious stars that might be local ionization sources. The $z$ values found along this slit position are very close to zero, similar to those found along Position 8. The simplest explanation is that despite the presence of the WR stars, R136 is still the dominant ionization source along the IF, including at the position identified by I08.

The two most eastern slit positions, 1 and 2, sample the cavity to the east of R136. In the top panel of Figure 2.20, as in Figure 2.19, we plot $z$ as a function of the offset along the slit in pc, with the location closest to R136 being the zero point in offset. There is considerable scatter in the $z$ values. To explore the possibility that this scatter is caused

by uncertainties in the electron density, we recomputed $z$ using

$$z_{corr} = \pm\left(\frac{n_{model}}{n_{avg}} R_{model}^2 - r_{projected}^2\right)^{1/2} \quad (13)$$

where $n_{avg}$ is an assumed average density in the local part of 30 Dor and $n_{model}$ is the density from the best fitting model. For the low-density or very faint regions of the nebula, where the density is poorly constrained (as is the case for this position), it would have been desirable to add an additional term to the goodness of fit parameter which included a comparison of the modeled density to the local density averaged over some area. To show the effect this would have we use equation 13 with a typical $n_{avg} = 10^{1.75}$ for the background wall in this region. The bottom panel of Figure 2.20 shows that assuming a constant typical density decreases the noise in $z$ significantly. This would be valid so long as there are no significant density gradients effecting $n_{avg}$ and the modeled $U$ is correct.

The inclination of the ionized face to the line of sight back to R136 is also a major source of uncertainty. It is assumed that the gas forms a plane parallel slab at a distance $r$ from the ionizing source, but the inclination relative to the ionizing source modifies the derived distance $R_{model}$ from R136 such that the true distance to the illuminated face $R_{true}$ would be

$$R_{true} = R_{model}(\cos\theta)^{1/2} \quad , \quad (14)$$

where $\theta$ is the inclination angle of the illuminated face relative to the direction to the ionizing source. There are at least three special cases of the modeled $R_{model}$ which should be considered in connection with possible inclination effects. The first is where $R_{model}$

equals the projected distance $r$ on the sky. If $Q_0$ is correct, this indicates that the $z$ coordinate of the ionized gas along the line of sight is zero. This also implies $\theta$ is equal to zero and the ionization front is being viewed nearly edge on. Another special case is when $R_0 < r$, which means that the ionizing source(s) must be closer than the model indicates. This requires a different or additional ionization source than R136.

The third case of special interest is an abrupt, discontinuous change in in the derived $R_{model}$. This could be due to a discontinuity in either or $R_{true}$. Sudden changes in the inclination angle (where = 0 is equivalent to a plane-parallel slab oriented perpendicular to the direction back to the ionizing source) occur at the lip of a tilted ionization front, as in the example labeled "a" in Figure 2.21. The horizontal face at the far left in the figure would receive a much lower ionizing flux than the tilted, face-on portion. A situation like this occurs with the Orion Bar (see P09).

There is significant evidence throughout 30 Dor that such changes in $\theta$ exist. Take for example the eastern limb that includes IF4, or the limb near the molecular gas corresponding to IF3. Both of these IFs border the central region of high ionization parameter discussed in Section 4. In both cases there is a strong, large-scale increase in the [S II]/H$\alpha$ ratio just beyond the peak in the [S II] emission, typical of all the other edge-on IFs, which indicates a decrease in $U$. This occurs despite a lowered gas density and similar projected distance from the central cluster. The simplest explanation for this is a geometry similar to that shown in example "a" of Figure 2.21.

An alternative explanation for a discontinuity in $\theta$ is a true geometric discontinuity in $R_{true}$, such as a free-floating filament or an optically thick overlapping shell which blocks

our line of sight to the background gas, as sketched in example "b" in Figure 2.21. If such an effect were important, the reddening free 3 cm and 6 cm radio continuum images from Lazendic et al. (2003) that trace the ionized gas would show a different structure than the optical data. On a large scale such a geometry is ruled out by comparing the $A_V$ measured with optical observations to those that are made with optical-radio data. We conclude that with the exception of the regions 190 arcsec south and approximately 190 arc north of R136 covered by slit positions 16 and 17, the observed H II region all across the face of 30 Dor is largely a continuous, unobstructed structure.

## 6.3 What Determined the Structure of 30 Dor?

The gas component of 30 Dor has a very complex distribution in space which is seen in all wavelengths from the IR to the X-ray. The gas got where it is today in response to pressure forces that have moved it there. To try to understand better why it has taken on its current distribution, we take an inventory of the various kinds of pressure currently at work in the nebula, and of their relative strengths at different points in the gas.

### 6.3.1 Thermal gas pressure in the $H^+$ zone

As a first step, we consider the thermal gas pressure observed at the IF at each point in the nebula. This is mapped in Figure 2.22, where the [S II] density and [O III] temperature measurements have been used to compute $P_{gas} = 2\ n_e k T_e$. There is very little change in $T_e$ from the illuminated face of a cloud to the ionization front (the IF). Therefore the reported pressure is equal to the gas pressure at the IF. We want to see if $P_{gas}$ is in equilibrium with the the sum of all the external pressures acting on the ionized layer.

The region of highest pressure shown in Figure 2.22 forms circular ring around the central cluster, reflecting the circular regions of high excitation and high density shown in Figs. 2.7c-g. Immediately outside this region (RA +/- 100 arcsec ) the gas pressure declines by a factor of 3, with the exception of the pressure in IFs 4 and 6.

### 6.3.2 Magnetic fields

In Orion (P08) and M17 (P09) we have explored the effect of pressure due to the compression of tangled magnetic fields, in relation to other pressure sources included in the overall equation of state. With no magnetic field measurements available for 30 Dor like those available for M17, nor highly resolved ionization fronts like in Orion, we cannot constrain the magnetic pressure. As is the case in Orion and M17, magnetic pressure may be important inside the PDRs and molecular regions of the clouds in 30 Dor, as part of the mechanism by which the cooler regions of the clouds push back against the gas pressure exerted by the $H^+$ zones. The only observational evidence for a structured magnetic field in 30 Doradus come from dust polarization (Nakajima et al. 2007) which should follow a local magnetic field (Davis & Greenstein 1951). These polarization maps do not provide constraints to B but show shell like structures 2.5' north of R136 between the bright arcs and the region 24 identified by Townsley et al. 2006. In the expanding shell to the east of R136 including IF 4 the field also seems to form a shell with the B vector perpendicular to a ray toward R136. However based on arguments below, the expected stellar radiation pressure is low, and the expected gradient in the $H^+$ region density profile will be small. This will prevent the amplification of any magnetic fields present in the HII region constant until the PDR. Therefore the presence of a magnetic field should not affect our conclusions derived from our spectroscopic data for

the $H^+$, but the existence of a magnetic field and it's effects should be considered in future studies of the PDR.

### 6.3.3 Radiation pressure from the ionizing stars

While there is significant uncertainty in the true geometry of 30 Dor, there is much less uncertainty in the ionization parameter *U*. Accounting for the inclination angle, *U* is given by

$$U = \frac{Q_0}{4\pi R_{ill}^2 c\, n_H} \cos\theta \qquad (15)$$

or in terms of the model parameter $R_0$

$$U = \frac{Q_0}{4\pi R_0^2 c\, n_H} \quad , \qquad (16)$$

recovering Equation 1. While the degeneracy between the distance to the illuminated face and the inclination angle remain unresolved, the solution for the ionization parameter is unique.

The pressure associated with the momentum absorbed from the incident photons can be approximated in terms of *U* by

$$P_{stars} = U \times n_H \langle h\nu \rangle \qquad (17)$$

where $\langle h\nu \rangle \sim 20$eV is the average energy per photon of the SED. This approximation is valid if the optical depth to ionizing radiation is greater than unity. Using this approximation we compare the observed thermal pressure to the derived radiation pressure, as in Figure 2.23 which shows a map of $\log_{10}(P_{stars}/P_{gas})$. There is a very strong correlation between the gas pressure and the radiation pressure within the highly ionized

region, indicating that the radiation pressure is having a strong effect. Here, the radiation pressure is approximately 1/3 of the total gas pressure gas pressure. Outside of the highly ionized region around R136, this ratio drops to below 1/10. For example, in the outlying IF 4 and IF 6, the radiation pressure is equal to 0.05 of the gas pressure.

From this it is clear that while in the high-pressure ring the effect of direct radiation pressure is likely to be quite important, it is negligible outside of that region ( i.e. for $r >$ 30 pc). This dichotomy can be seen in the plot of electron density vs. $U$ in Figure 2.24. In such a plot two populations are evident. The first shows a correlation between $n_e$ and $U$ in the region near the cluster. This is a scaled up and more complicated form of the scaling between density and $U$ found in the Orion Nebula by Baldwin et al. (1991) and by Wen & O'Dell (1995). The second population has no correlation between density and radiation pressure suggestive of another important physical process.

### 6.3.4 Pressure from the hot X-ray-emitting gas

In the cases of M17 and Orion, the O-stars contribute to the dynamics via stellar winds which thermalize with a preexisting $10^6$ - $10^7$ K plasma. This hot plasma will either escape into the ISM or be confined by the surrounding molecular cloud. In the later case, the pressure associated with this gas is thought to form the bubbles and cavities which characterize the central parts of many H II regions.

In 30 Dor, this situation is made much more complicated because of the many SNe that presumably also have contributed to the hot gas. The definitive study of the diffuse X-ray emitting structures in 30 Dor is by Townsley et al. (2006), who identified 17 unique X-ray emitting regions that lie within the area covered by our spectroscopic maps. For each region, Townsley et al. gave the temperature, the absorption-corrected luminosity, and

the area on the sky. If we make the working assumption that the volume containing each region is spherical, we can compute a volume density and then a gas pressure $P_{X\text{-}ray}$ for the X-ray emitting gas in each region. $P_{X\text{-}ray}$ will be the sum of the mechanical energy input from stellar winds and SNe. $P_{X\text{-}ray}$ is shown in Figure 2.25 in cgs units and listed in table 2.11.

The $P_{X\text{-}ray}$ in the different regions are all very similar to each other. This suggests that the X-ray emitting volumes are interlinked, an idea that has previously been put forth on other grounds by Townsley et al. (2006). Could the pressures have equalized within the lifetime of the existing star cluster? Using the densities to derive a sound speed, we find a sound crossing time of $10^5$ yr for the largest bubbles, much shorter than the lifetimes of the current generation of O stars.

The energy stored in the X-ray emitting gas is very large. The cooling time can be approximated by $t_{cool} = \Lambda\, n_e / kT$, where $\Lambda = 5 \times 10^{-23}$ erg cm$^{-3}$ is the estimated emissivity of an X-ray gas with $kT = 0.7$ keV ( Landi & Landini 1999 ). For the parameters for 30 Dor, it is of the order $t_{cool} \sim 15$ Myr, so a confined plasma will remain at X-ray emitting temperatures for the typical lifetime of a few million years for an H II region, at which time the molecular cloud will be dispersed. Therefore the heat energy currently stored in the X-ray emitting gas could have been accumulated over the livetime of the star cluster.

We also checked to make sure that the X-ray emitting gas does not prevent ionizing radiation from reaching the outer parts of the 30 Dor nebula. We used Cloudy to compute a coronal model of the X-ray plasma, and found a neutral H fraction $\log[n(H^0)/n(H)] =$

-7.41. Assuming a typical hydrogen density $n_H$ = 0.14 $cm^{-3}$ the optical depth to ionizing radiation over the distance $r$ = 50 pc to IF4 (on the far eastern wall of the large cavity) is $\tau = n(H_0) r \sigma = 5.1 \times 10^{-6}$, where $\sigma$ is the photoionization cross section of hydrogen equal to $6 \times 10^{-8}$ $cm^{-2}$. Although the X-ray emitting gas has a big effect on the dynamics of the H II region, it does not impede the stars from providing the ionization.

There is one region not identified by Townsley et al. (2006) that is especially interesting. North of their region 16 and east of their Region 24 is an area of very low emission at all wavelengths. Figure 2.26 shows this area in the SOAR [S II] (left) and Chandra 0.5-0.7keV (right) images of the region. The contours trace the X-ray surface brightness and outline the Townsely et al. 2006 Regions 16 and 24. Both Regions 16 and 24 are very bright in X-ray emission and are bounded by well-defined IFs seen in [S II]. The intervening region of low X-ray surface brightness is the only region within 30 Doradus where the optical morphology clearly suggests a large-scale outflow of gas. This manifests itself as long filaments all oriented parallel away from R136. It is understandable that this was not noticed before. This region was not covered by the HST observations and the filaments are completely unresolved at the resolution of the MCELS survey. This seems to be an example of a region where the the X-ray gas is *not* contained. The expected result is an outflow and low density. This region was not covered by the kinematic study by Chu and Kennicutt (1994). The lack of this type of structure anywhere else in 30 Dor supports our conclusions that the X-ray gas is for the most part confined by the molecular gas, resulting in a pressure equilibrium between it and the $10^4$ K gas in the IFs.

IF 4 seems to be a clear example of a place where the X-ray pressure is dominant. The gas pressure along the wall is $5.8 \times 10^{-10}$ dyne $cm^{-2}$. The expected contribution from stars in the form of radiation pressure at that distance is $2.8 \times 10^{-11}$ dyne $cm^{-2}$. The other observed pressure source in the region is the diffuse X-ray emitting gas (Townsely et al. 2006). X-ray Region 12 Townsley et al. (2006) seems to fill the cavity that is bounded by IF4. Using the observed surface brightness and assuming a spherical geometry we estimate the electron density of the hot gas to be equal to 0.14 $cm^{-3}$. Using the temperature reported for Region 12 the thermal X-ray pressure is equal to $5 \times 10^{-11}$ dyne $cm^{-2}$, in close agreement with the measured pressure in the wall. This also means the gas pressure at the illuminated face, where the H II region is in contact with the X-ray gas, is equal to the gas pressure at the IF, in close agreement with our constant density models. In Figure 2.27 we show the ratio of the X-ray to gas pressure. Aside from the IFs southwest and northeast of R136 which outline the molecular cloud, the ratio of $P_{X\text{-}ray}/P_{gas}$ is between 1 and 10 for the entire region. Given the uncertainty in the assumptions regarding the geometry of the X-ray-emitting gas and how it affects $P_{X\text{-}ray}$, the typical $P_{X\text{-}ray}/P_{gas}$ ratio is higher than 1. Except in the inner regions, the pressure in the $H^+$ zone clearly is set by $P_{X\text{-}ray}$ which dominates the equation of state by an order of magnitude, and is likely driving the current outflows, expansion and compression of the remaining molecular material.

### 6.4 The Global Abundances

The most reliable abundance measurements from this study are for He, O, N, and S

relative to H. Our He abundance is consistent with all values in the literature, which is reassuring since there is very little scatter in the reported values of the He/H ratio. As is shown in Table 2.10, there is much less agreement for O, N and S between different studies. The reported ranges in the (O/H) abundance ratio are $-3.75 \leq \log(O/H) \leq -3.5$. We find log(O/H) = -3.75, in agreement with the lower limit. Like O, our S abundance log(S/H) = -0.32 is within the range $-5.32 \leq \log(S/H) \leq -5.01$ found in other studies. The (S/O) ratio found here, log(S/O) = -1.57, is equal to the average of the (S/O) ratios found in other studies.

The place where we find significant discrepancies with previous work is in the resulting (N/O) and (N/S) ratios (Table 2.12). Although our measurement of log(N/H) = -4.91 falls within the range of previous measurements, our measured log(N/O) = -1.16 and log(N/S) = 0.41 are both 0.1 in the logarithm higher than in any other study. This could conceivably be an artifact of the of the SED adopted here, but it is fair to say that our abundances represent a much broader average over the full 30 Dor nebula than do the previous results, and the difference may be real.

It is well known that N can be enhanced due to secondary processing in the CNO cycle in stars more massive than the Sun (Pettini et al. 2002). N II and SII have very similar ionization potentials and trace the same physical conditions in the nebula. The ratio of the [N II] $\lambda$6584 to [S II] $\lambda$6716+$\lambda$6731 surface brightness, which is mapped in Figure 2.28, indicates changes in relative abundances of N/S. Using this ratio as an indicator we find two regions with a possible enhancement of the (N/S) abundance, one around R136 and the bright rim to its east, and the other around Hodge 301. Hodge 301 is a 25 Myr old cluster which lies 190 arcsec NW of R136, and its vicinity has likely been polluted by

SNe.

These results seem to correlate with the surface brightness of the nebula. To check for any systematic errors in the line measurements due to changes in surface brightness, we measured line ratios by hand (using the IRAF SPLOT routine) at five locations with low surface brightness and five locations with high surface brightness. We found that uncertainties in placing the continuum could lead to a 5 percent increase over the uncertainties returned by our automated measuring routine, but that there is no evidence of systematic errors. We conclude that the line measurements are accurate and that real variations in elemental abundances and/or unaccounted-for physical processes are causing the ([N II] λ6584 )/ [S II] (λ6716+λ6731) intensity ratio to change across the nebula.

### 6.5 Abundance Comparison With Other Methods

The technique for determining abundances used here has not, to our knowledge, been used previously for a single H II region. It is similar to the strong line methods developed by Pagel et al. 1992; Tremonti et al. 2004; Kewley & Doptia 2002; Pettini & Pagel 2004 and others, which are used to study the spatially integrated spectra of distant H II regions and galaxies. Our technique improves on the strong-line approach because it includes direct empirical measurements of $T_e$ and $n_e$. It also removes the need to describe an entire, complex nebula by a single ionization parameter and density, and instead examines many small regions with many different densities and ionizing fluxes. Using the observed correlations between ([O III] λ5007)/Hβ, ([N II] λ6584)/Hα, ([S III] λ6312)/([S II] λ6716 + λ6731) and [S II]/Hα in conjunction with Cloudy models and

temperature constraints, we can measure the ionization parameter and total gas phase abundances using relatively few emission lines.

Our approach has certainly glossed over many of the finer details often considered when doing a an empirical measurement at one place in the nebula, but averages over a much greater fraction of the full nebula and returns results within the range of reported empirical measurements except for the unusually high (N/O) and (N/S) abundance ratios. The next question is: *What would the result be if 30 Dor were instead observed from a much larger distance so that only the strong-line methods could be used?* It is important to make this test because the strong-line technique is now routinely being applied to very large samples of objects seen out to large look back times, and many big-picture results are being deduced from the resulting abundance measurements based on the integrated spectrum of entire HII regions and galaxies. These include a survey of over 500 galaxies from z = 0 – 1 ( Hu et al. 2009), as well as single galaxies at z = 1.7 (Yuan & Kewley 2009) .

There are a number of warning flags that there may be systematic errors in the strong-line abundances. The different strong-line methods do not agree among themselves, although calibrations can transform them all onto any one arbitrarily chosen scale (Kewley & Ellison 2008 ). The strong-line abundances also are known to disagree with purely empirical abundance measurements based on direct measurements of $T_e$, $n_e$ and the ionization fractions for different elements (Kennicutt et al. 2003; Tremonti et al. 2004; Kewley & Doptia 2002; Pettini & Pagel 2004). Bresolin et al. (2009) have recently determined the abundance gradient in the nearby spiral galaxy NGC 300 using empirical measurements of individual H II regions, and find that its slope and absolute value are in

good agreement with abundances determined from stars in the same galaxy, but systematically different than the strong-line results.

All of the comparisons of strong-line to empirical techniques made to date are for entire H II regions or entire galaxies each treated as a single idealized point. For example, the Bresolin et al. (2009) study uses data for 28 H II regions spread across the face of NGC 300. Each of those H II regions is a complex thing similar in size and nature to 30 Dor. Yin et al. (2007) also sought to calibrate strong line methods using the integrated spectra 695 galaxies with [O III] 4363 detections using mostly data from the SDSS-DR4.

For this reason, our study which takes into account the detailed structure within 30 Dor is a valuable complement to those earlier results for the HII regions. We first compare our 30 Dor abundance results to those that would be determined using the strong line method of Dopita et al. (2006). These authors developed a grid of models incorporating an assumed history of stellar evolution in the H II region, which in turn determines the current SED and mechanical energy input via SNe and stellar winds. The models are parametrized by three variables which determine the physical conditions and emission line spectrum. They are the age of the cluster *t*, the metallicity *Z*, and a (gravitating mass)/pressure ratio *R* defined as

$$R = \log_{10}[(M_{CLUSTER}/M_{\odot})/(P/k)] \qquad (18)$$

in cgs units.

To compare our results to strong line methods we will use line ratios, the [S II] density and the O III temperature measured from our globally integrated spectrum. For the observed cluster mass of the order $10^4$-$10^5$ $M_{\odot}$, $n_H = 10^2$, $T$=10,500K, $R$ is observed to be between -1 and -2. $Z$ is primarily characterized by the oxygen abundance and given in

units relative to solar abundances.

In the Dopita et al. models, $Z_{\odot}$ is defined as log(O/H) = -3.34 . On this scale our derived oxygen abundances becomes $Z = 0.41\ Z_{\odot}$. The available models cover the span $-6 \leq R \leq 2$ in increments of 2. The modeled ages range from 0.1 to 4.5 Myr in increments of 0.5 Myr beginning at 0.5 Myr. Finally the available abundances are 0.05, 0.2, 0.4, 1 and 2 in units of $Z/Z_{\odot}$.

We compared the line strengths predicted by each Dopita et al. (2006) model to the lines measured from our 30 Dor composite spectrum, and ranked them using Equation 11. We did this using the intensities of He I λ6678, [O III] λ5007, [O I] λ6300, ([O II] λ7320+λ7330), [N II] λ6584, and ([S II] λ6716 + λ6731) relative to Hβ and the [S II] λ6716/ λ6731 ratio. Identifying the initial best fit model, we interpolated the models between different values of $R$. We find the best agreement with the observations come from models with $Z = -0.4$, $-2 < R < -1.5$ and ages $0.5 < t < 2.0$ Myr. The ages are consistent with the youngest observed population of O stars in 30 Dor. For younger ages the difference between the observed and modeled ([O III] λ5007)/ Hβ ratio is less than 10 percent, but the lower ionization lines are under predicted by about a factor of two. The situation is reversed for older ages, when the models seem to be to be too weakly ionized, with the best fit at 2.0 Myr. We find that despite the complexities of the region, the assumptions and simplifications of this strong line method are sufficient to reproduce the known physical properties of 30 Dor derived from our more detailed treatment. In particular, the abundances $Z$ are in almost exact agreement.

A simpler abundance measurement can be made using the calibration involving only [N

II]/Hα (Pettini & Pagel 2004). This is an empirical measurement based on a sample of 137 extragalactic H II regions with well-constrained (O/H) and [N II]/Hα ratios.

Inserting the value of [N II]/Hα from our composite spectrum into Equation 1 from Pettini & Pagel (2004) gives a derived oxygen abundance [O/H] = -3.87 +/- 0.38. This is -0.12 dex lower than the value from our study or from the strong line method of Kewley and Dopita (2002) using the models from Dopita et al. (2006), but agree with those results to within the quoted uncertainty of the method.

In the comparisons between the strong-line methods and the purely empirical methods, the empirical results are often considered suspicious because temperature fluctuations can weight hotter vs. cooler regions of the gas in different ways in different emission lines. We have already described (Sect. 4.4) our measurement of the temperature fluctuation parameter $t^2$ in 30 Dor. We find a larger value than had been reported previously, one which would have a significant effect on the abundances determined from the empirical method, but we are not confident of that result because of the possibility of systematic errors.

In summary, the abundances derived from our point-by-point analysis of 30 Dor are in good agreement with those that would have been found with the strong-lined methods. This result in favor of the strong-lined abundance determinations is contrary to the conclusions reached by Bresolin et al. (2009) from their very different test of the strong-lined method.

## 7 Conclusions

We have obtained and are making publicly available a dense grid of long-slit optical

spectra which measure key emission lines in the λλ4100-7400Å wavelength region over a 140×80 $pc^2$ (10×6 $arcmin^2$) region of 30 Dor. These spectra were taken at 37 slit positions and then extracted and measured as 4238 individual 1D spectra. The resulting 'data cube' of emission line intensity measurements is also publicly available. Supplementary spectra at a few additional slit positions extended the coverage to a wider wavelength range.

We also obtained a set of subarcsec-resolution direct images in multiple narrow-band filters, covering a 170×180 $pc^2$ (12×13 $arcmin^2$) field of view, which we have used to identify and catalog a large number of structures of special interest. These include regions likely to be locally ionized by embedded stars, as well as edge-on ionization fronts seen in both the visible and infrared and 'elephant trunk' pillars. With JWST and ALMA on the horizon and the newly upgraded HST, these structures will provide important sites for further constraining the physical conditions in the PDRs of distant low-metallicity extragalactic H II regions through calibrating measurements in this closest example of such an object.

We find that the cluster of O stars centered around R136 is the dominate source of radiation for almost all of the nebula. We find no compelling evidence of large scale variations in *U* resulting from multiple, embedded ionization sources.

We have combined photoionization models with empirically determined nebular temperatures and densities to measure point-by-point variations in the ionization parameter in order to reconstruct the ionization structure of 30 Doradus. This technique provides us with a comprehensive measurement of the global abundances. We find an oxygen abundance 0.15 dex lower than that found in recent studies of the bright arcs, but

within the observed range of reported abundances. Attempts to use the SED and abundances used in the photoionization modeling of 30 Dor by TP05 failed. We found differences in the gas temperatures depending on the photoionization code used. This led us to adopt a new, lower oxygen abundance consistent with V02. We find systematically higher N/O and N/S ratios than previous studies, which may suggest we are more sensitive to secondary enhancement of N.

Despite a clear correlation between $n_e$ and $U$ in 30 Dor, the geometric dilution of radiation pressure over many tens of parsecs is significant. As has been suggested by other authors in previous papers, we have shown that the dynamics and large scale structure are set by a confined system of X-ray bubbles in rough pressure equilibrium with each other and with the confining molecular gas. The long cooling time of the X-ray emitting gas means that it will dominate the dynamics until it is no longer confined. This is unlike the the situations in the much smaller Orion and M17 H II regions which we have also studied in detail.

The often-studied bright arcs do not represent the average physical conditions in the nebula, nor do they account for the majority of the line emission. They are of higher density and ionization parameter than would characterize the whole nebula if viewed as a single point-like source at a great distance. Studies focusing on the fainter emission are likely to examine the physical conditions characterizing those observed in distant nebulae.

We use the results from our spatially resolved survey to test the accuracy of two strong-line abundance measurement methods. Despite the general complexity and large scale changes in $U$ across 30 Dor, there is excellent agreement between our measured

abundances and those determined using the strong-line method outlined by Kewley & Dopita. Their models representing entire H II regions and H II galaxies as being characterized by a single, time dependent ionization parameter accurately reproduce the global spectrum of 30 Dor. This includes correctly estimating the ratio of cluster mass to gas pressure, the cluster age and the oxygen abundance.

**Acknowledgements**

EWP gratefully acknowledges financial support from the National Science Foundation (grant AST-0305833), NASA (07-ATFP07-0124, STScI GO09736.02-A and STScI AR-10932) and Michigan State University's Center for the Study of Cosmic Evolution.

Table 2.1: Summary of imaging observations used in 30 Doradus optical mosaics.

| Table 2.1<br>DETAILS OF DECEMBER 2007 NARROWBAND OBSERVATIONS OF 30 DORADUS | | | | |
|---|---|---|---|---|
| Filter | No. of Exp x Duration at each position | No. Positions | FWHM (arcsec) | Min/Max Exposure(s) |
| 6563 | 3 x 150s | 6 | 0.9 | 300/1480 |
| 6738 | 3 x 450s | 6 | 1.04 | 900/5700 |
| 6850 | 3 x 450s | 6 | 0.8-1.0 | 900/5700 |
| 5019 | 3 x 225s | 5 | 1.01 | 450/2500 |
| 5130 | 3 x 225s | 5 | 1.04-1.1 | 450/2500 |

Table 2.2: Summary of Blanco and SOAR spectroscopic observations of 30 Doradus. Included in columns 1-5 are position number corresponding to Figures 2.1 and 2.2, RA and Declination of the slit center, PA and exposure time.

**Table 2.2**
**OBSERVATIONAL DETAILS FOR THE SPECTROSCOPIC SURVEY OF 30 DORADUS**

| Position No. | R.A. (2000) (slit center) | Dec. (2000) (slit center) | PA (deg E of N) | Exposure Time (s) |
|---|---|---|---|---|
| Blanco Telescope | | | | |
| 1 | 05:39:16.53 | -69:06:37.04 | 13 | 405 |
| 2 | 05:39:11.25 | -69:06:31.18 | 13 | 425 |
| 3 | 05:39:06.29 | -69:06:29.68 | 13 | 405 |
| 4 | 05:39:00.44 | -69:06:22.80 | 13 | 250 |
| 5 | 05:38:56..29 | -69:06:11.60 | 13 | 500 |
| 6 | 05:38:52.21 | -69:06:11.81 | 13 | 260 |
| 7 | 05:38:45.00 | -69:06:03.65 | 13 | 260 |
| 8 | 05:38:41.38 | -69:05:55.66 | 13 | 320 |
| 9 | 05:38:37.98 | -69:05:53.44 | 13 | 300 |
| 10 | 05:38:35.17 | -69:05:48.71 | 13 | 120 |
| 11 | 05:38:30.08 | -69:05:38.24 | 13 | 400 |
| 12 | 05:38:24.82 | -69:05:29.57 | 13 | 450 |
| 13 | 05:38:17.42 | -69:05:28.52 | 13 | 500 |
| 14 | 05:38:08.61 | -69:05:18.33 | 13 | 300 |
| 15 | 05:37:59.70 | -69:04:56.19 | 13 | 250 |
| 16 | 05:38:49.47 | -69:01:28.18 | 13 | 600 |
| 17 | 05:38:37.48 | -69:08:52.47 | 13 | 600 |
| 20 | 05:39:16.50 | -69:04:51.76 | 103 | 400 |
| 21 | 05:38:28.34 | -69:03:50.99 | 103 | 400 |
| 22 | 05:39:15.65 | -69:05:28.77 | 103 | 405 |
| 23 | 05:38:27.16 | -69:04:29.19 | 103 | 308 |
| 24 | 05:39:12.49 | -69:05:54.62 | 103 | 500 |
| 25 | 05:38:25.24 | -69:04:55.67 | 103 | 355 |
| 26 | 05:39:12.16 | -69:06:22.34 | 103 | 500 |
| 27 | 05:38:25.90 | -69:05:23.89 | 103 | 460 |
| 28 | 05:39:06.04 | -69:06:36.65 | 103 | 600 |
| 29 | 05:38:22.74 | -69:05:43.05 | 103 | 520 |
| 30 | 05:39:07.60 | -69:07:05.02 | 103 | 700 |
| 31 | 05:38:24.16 | -69:06:13.86 | 98 | 450 |

| Table 2.2 (cont'd). | | | | |
|---|---|---|---|---|
| 32 | 05:39:06.61 | -69:07:26.38 | 103 | 900 |
| 33 | 05:38:21.35 | -69:06:31.58 | 103 | 500 |
| 34 | 05:39:06.01 | -69:07:58.72 | 103 | 400 |
| 35 | 05:38:20.45 | -69:07:00.61 | 103 | 300 |
| 36 | 05:39:01.11 | -69:08:34.64 | 103 | 600 |
| 37 | 05:38:15.70 | -69:07:38.32 | 103 | 450 |
| SOAR Telescope | | | | |
| 40 | 05:38:46.430 | -69:05:35.06 | 10 | 1000 |
| 41 | 05:39:03.142 | -69:06:40.45 | 33.9 | 3000 |
| 42 | 05:39:02.763 | -69:06:45.82 | 61 | 2000 |
| 43 | 05:39:21.240 | -69:06:55.44 | 61 | 300 |
| 44 | 05:39:08.649 | -69:07:02.80 | 80 | 3000 |

**Table 2.3.** Line IDs and wavelengths. Measured strengths for each of these lines are listed in Table 2.4 and/or 2.5 at every extracted point in the nebula. Rest frame wavelengths with an asterisk indicate the lines used below to fit the Blanco data to models at each point in the nebula as described below.

**Table 2.3. Line IDs**

| $\lambda_{Obs}$ | $\lambda_0$ | ion | $f_\lambda(R = 3.1)$ | Data Set |
|---|---|---|---|---|
| 4106 | 4101 | H I | 1.43 | SOAR |
| 4344 | 4340 | H I | 1.35 | Blanco+SOAR |
| 4366 | 4363 | [O III] | 1.34 | Blanco+SOAR |
| 4476 | 4471 | He I | 1.30 | Blanco+SOAR |
| 4800 | 4800 | Continuum | 1.19 | Blanco+SOAR |
| 4866 | 4861* | H I | 1.16 | Blanco+SOAR |
| 4926 | 4922 | He I | 1.14 | SOAR |
| 4963 | 4959 | [O III] | 1.13 | Blanco+SOAR |
| 5012 | 5007* | [O III] | 1.12 | Blanco+SOAR |
| 5625 | 5625 | Continuum | 0.97 | Blanco+SOAR |
| 5880 | 5875* | He I | 0.93 | Blanco+SOAR |
| 6308 | 6300 | [O I] | 0.86 | SOAR |
| 6318 | 6312 | [S III] | 0.86 | Blanco+SOAR |
| 6364 | 6364 | NS [O I] | - | Blanco |
| 6552 | 6548 | [N II] | 0.82 | Blanco+SOAR |
| 6570 | 6563 | H I | 0.82 | Blanco+SOAR |
| 6590 | 6584* | [N II] | 0.81 | Blanco+SOAR |
| 6684 | 6678 | He I | 0.80 | Blanco+SOAR |
| 6721 | 6716* | [S II] | 0.79 | Blanco+SOAR |
| 6738 | 6731* | [S II] | 0.79 | Blanco+SOAR |
| 7072 | 7065* | He I | 0.74 | Blanco+SOAR |
| 7142 | 7135* | [Ar III] | 0.73 | Blanco+SOAR |
| 7288 | 7281 | He I | 0.71 | SOAR |
| 7325 | 7320 | [O II] | 0.7 | SOAR |
| 7337 | 7330 | [O II] | 0.7 | SOAR |
| 7758 | 7751 | [Ar III] | 0.63 | SOAR |
| 9075 | 9069 | [S III] | 0.48 | SOAR |

**Table 2.4.** A portion of the reddening-corrected Blanco spectroscopic data cube in table form as described in the text. The units of electron density and temperature are $cm^{-3}$ and K, respectively. The dereddened Hβ surface brightness are reported in units of erg $s^{-1}$ $cm^{-2}$ $arcsec^{-2}$. The other emission lines are reported as 100×*S*(line)/*S*(Hλ). The entries for position number 38 are average values for the whole data set, as described in the text.

**TABLE 2.4**
**EXAMPLE OF PUBLICLY AVAILABLE SCIENCE PRODUCT FROM Blanco SPECTROPHOTOMETRIC SURVEY OF 30 DORADUS**

| Pos | ΔRA | □Dec | row | log $n_e$ | -err | +err | T(O3) | -err | +err | $A_V$ | F(Hβ) | err |
|---|---|---|---|---|---|---|---|---|---|---|---|---|
| 1 | 2 | 3 | 4 | 5 | 6 | 7 | 8 | 9 | 10 | 11 | 12 | 13 |
| 1 | 148.1 | -181.6 | 3 | 1.41 | 0.41 | 0.27 | 13600 | 1010 | 1500 | 1.12 | 6.56E-15 | 5.65E-17 |
| 1 | 148.6 | -179.1 | 8 | 1.70 | 0.24 | 0.16 | 10900 | 1280 | 3210 | 1.13 | 6.38E-15 | 6.38E-15 |
| 1 | 149.2 | -176.7 | 13 | 1.01 | 0.01 | 0.51 | 9690 | 1360 | 6450 | 1.21 | 6.80E-15 | 6.80E-15 |
| 1 | 149.8 | -174.2 | 18 | 1.73 | 0.22 | 0.15 | 12900 | 1270 | 2320 | 1.23 | 7.07E-15 | 7.07E-15 |
| | | | | | | | | | | | | |
| 37 | 1.4 | -128.0 | 598 | 2.01 | 0.09 | 0.08 | 19900 | 2040 | 3270 | 2.50 | 2.28E-14 | 3.86E-16 |
| 37 | 3.9 | -128.5 | 603 | 1.88 | 0.11 | 0.09 | 13900 | 1320 | 2280 | 2.86 | 3.03E-14 | 6.13E-16 |
| 38 | 0.0 | 0.0 | 1 | 2.11 | 0.001 | 0.001 | 10800 | 8 | 8 | 0.00 | 6.09E-14 | 4.09E-18 |
| 38 | 0.0 | 0.0 | 2 | 2.08 | 0.001 | 0.001 | 0 | 4 | 4 | 1.28 | 1.43E-14 | 7.96E-019 |
| 38 | 0.0 | 0.0 | 3 | 2.08 | 0.001 | 0.001 | 10700 | 5 | 5 | 0.00 | 5.75E-14 | 3.20E-18 |

**Table 2.5.** A portion of the reddening corrected SOAR data set, in the same format as Table 2.4 but with additional columns because more emission lines are measured. These include [S III] λ9069 which was used with [S III] λ6312 to measure the gas temperature using [S III] in a manner identical to that described using [O III].

| **Table 2.5. A portion of the dereddened SOAR spectroscopy results** | | | | | | | | | | | | |
|---|---|---|---|---|---|---|---|---|---|---|---|---|
| Pos | RA | De | row | log(ne) | T(O3) K | -err | +err | [S3]T | -err | +err | Av | F(Hβ) |
| 1 | 2 | 3 | 4 | 5 | 6 | 7 | 8 | 9 | 10 | 11 | 12 | 13 |
| 40 | 4.65 | -72.58 | 260 | 2.34 | 13112 | 579 | 724 | 11960 | 43 | 43 | 1.49 | 1.07E-13 |
| 40 | 5.03 | -70.42 | 275 | 2.43 | 14065 | 1116 | 1706 | 9875 | 66 | 68 | 1.89 | 7.86E-14 |
| 40 | 5.41 | -68.26 | 290 | 2.67 | 11542 | 1048 | 1884 | 11792 | 68 | 70 | 1.88 | 8.76E-14 |
| 40 | 5.79 | -66.09 | 305 | 2.55 | 13248 | 968 | 1443 | 11673 | 57 | 58 | 1.93 | 9.77E-14 |
| 40 | 6.18 | -63.93 | 320 | 2.7 | 11483 | 578 | 766 | 11972 | 34 | 34 | 1.67 | 1.40E-13 |
| 40 | 6.56 | -61.77 | 335 | 2.8 | 11915 | 448 | 547 | 11648 | 26 | 26 | 1.48 | 1.67E-13 |

Table 2.6: Possible regions with a locally enhanced ionization parameter due to nearby massive stars. Columns 1-6 correspond to a unique ID, RA and Dec, RA and Dec offsets from R136 of theionizing star and radius of obvious influence visible in the [S II]/Hα image.

| Table 2.6 Possible Regions of Enhanced Flux Due to Nearby Stars | | | | | |
|---|---|---|---|---|---|
| Object ID | RA | Dec | RA | Dec | radius (arcsec) |
| 1 | 05:39:03.44 | -69:06:35.72 | 113 | -32 | 3.97 |
| 2 | 05:39:10.17 | -69:06:22.63 | 149 | -19 | 3.97 |
| 3 | 05:38:57.10 | -69:06:06.62 | 79 | -3 | 1.43 |
| 4 | 05:39:05.43 | -69:04:16.27 | 124 | 108 | 2.85 |
| 5 | 05:39:05.51 | -69:04:31.61 | 124 | 92 | 2.77 |
| 6 | 05:38:24.46 | -69:07:57.28 | -97 | -113 | 2.78 |
| 7 | 05:38:38.86 | -69:08:16.05 | -19 | -132 | 4.76 |
| 8 | 05:38:01.61 | -69:04:50.49 | -219 | 73 | 1.69 |
| 9 | 05:38:01.31 | -69:04:50.25 | -221 | 74 | 1.35 |
| 10 | 05:38:41.19 | -69:02:57.75 | -7 | 186 | 3.07 |
| 11 | 05:38:45.39 | -69:02:50.84 | 16 | 193 | 3.83 |
| 12 | 05:38:13.98 | -69:07:47.63 | -153 | -104 | 10.11 |
| 13 | 05:39:20.55 | -69:06:54.42 | 205 | -51 | 4.06 |
| 14 | 05:39:03.36 | -69:09:33.58 | 113 | -210 | 3.02 |
| 15 | 05:38:45.08 | -69:08:08.06 | 14 | -124 | 6.26 |
| 16 | 05:38:52.82 | -69:06:12.01 | 56 | -8 | 3.81 |
| 17 | 05:38:55.79 | -69:05:24.90 | 72 | 39 | 2.41 |
| 18 | 05:38:04.84 | -69:07:34.84 | -202 | -91 | 3.54 |
| 19 | 05:38:31.75 | -69:02:14.28 | -57 | 230 | 3.59 |
| 20 | 05:38:41.76 | -69:01:58.79 | -4 | 245 | 4.27 |
| 21 | 05:38:53.54 | -69:02:00.56 | 60 | 243 | 2.43 |
| 22 | 05:39:11.63 | -69:02:01.02 | 157 | 243 | 3.07 |
| 23 | 05:38:15.64 | -69:04:37.64 | -144 | 86 | 9.94 |
| 24 | 05:38:54.94 | -69:08:45.76 | 67 | -162 | 3.77 |
| 25 | 05:38:56.83 | -69:08:42.47 | 77 | -159 | 4.25 |
| 26 | 05:38:54.70 | -69:07:45.81 | 66 | -102 | 5.29 |
| 27 | 05:38:36.43 | -69:06:58.70 | -32 | -55 | 2.98 |
| 28 | 05:38:36.06 | -69:06:47.52 | -34 | -44 | 2.04 |
| 29 | 05:38:51.32 | -69:06:41.99 | 48 | -38 | 2.84 |
| 30 | 05:38:49.79 | -69:06:44.12 | 40 | -40 | 1.7 |
| 31 | 05:38:57.40 | -69:07:10.75 | 81 | -67 | 2.73 |
| 32 | 05:38:46.60 | -69:04:28.07 | 22 | 96 | 2.3 |
| 33 | 05:38:36.91 | -69:05:08.19 | -30 | 56 | 5.97 |
| 34 | 05:39:01.05 | -69:06:30.16 | 100 | -26 | 2.44 |
| 35 | 05:38:58.80 | -69:05:24.55 | 88 | 39 | 2.46 |
| 36 | 05:38:17.62 | -69:05:42.83 | -133 | 21 | 13.67 |
| 37 | 05:39:22.86 | -69:07:46.88 | 217 | -103 | 3.39 |
| 38 | 05:39:12.35 | -69:06:02.74 | 161 | 1 | 4.78 |
| 39 | 05:38:14.88 | -69:04:31.80 | -148 | 92 | 2.31 |
| 40 | 05:38:08.53 | -69:05:44.36 | -182 | 19 | 15.11 |
| 41 | 05:38:10.64 | -69:06:17.52 | -171 | -14 | 3.69 |
| 42 | 05:38:09.46 | -69:06:22.26 | -177 | -18 | 3.69 |
| 43 | 05:37:49.22 | -69:06:14.27 | -286 | -10 | 4.41 |
| 44 | 05:38:24.70 | -69:07:43.55 | -95 | -100 | 3.06 |
| 45 | 05:38:30.51 | -69:06:46.21 | -64 | -42 | 3.07 |
| 46 | 05:38:29.73 | -69:06:57.41 | -68 | -54 | 3.07 |
| 47 | 05:38:31.02 | -69:06:37.47 | -61 | -34 | 2.63 |

Table 2.7: Prominent IFs suitable for follow up study with multi-wavelength data. From left to right the columns are ID, RA, Dec, RA and DEC offsets from R136, IF length and PA. IDs with an asterisks identify IFs with PAH emission closer to R136 than the [S II] emission.

| **Table 2.7: Prominent Ionization Fronts Detected in IR and Optical Wavelengths** | | | | | | |
|---|---|---|---|---|---|---|
| IF id | RA (2000) | Dec (2000) | DRA | DDec | Length | PA |
| 1 | 05:38:44.15 | -69:06:59.71 | 9.3 | -55.9 | 31.0 | 257.7 |
| 2 | 05:38:55.02 | -69:05:42.02 | 67.7 | 21.8 | 39.8 | 317.9 |
| 3 | 05:38:36.07 | -69:06:27.99 | -34.1 | -24.2 | 92.2 | 349.1 |
| 4 | 05:39:22.75 | -69:07:17.56 | 216.8 | -73.8 | 87.3 | 34.7 |
| 5 | 05:39:11.80 | -69:08:14.33 | 157.9 | -130.5 | 49.0 | 68.9 |
| 6 | 05:38:59.15 | -69:05:14.79 | 89.9 | 49.0 | 38.2 | 120.0 |
| 7 | 05:38:51.70 | -69:05:06.06 | 49.9 | 57.7 | 38.2 | 70.0 |
| 8 | 05:37:55.71 | -69:05:43.70 | -251.1 | 20.1 | 75.2 | 321.9 |
| 9 | 05:38:58.56 | -69:08:43.34 | 86.8 | -159.5 | 2.4 | 324.7 |
| 9 | 05:37:54.88 | -69:05:11.42 | -255.6 | 52.4 | 59.5 | 306.1 |
| 10 | 05:37:45.34 | -69:05:14.08 | -306.8 | 49.7 | 28.5 | 0.0 |
| 11 | 05:38:06.22 | -69:07:43.53 | -194.6 | -99.7 | 37.3 | 344.1 |
| 12 | 05:38:11.38 | -69:08:06.38 | -166.9 | -122.6 | 37.3 | 283.8 |
| 13 | 05:39:37.31 | -69:07:17.48 | 295.1 | -73.7 | 28.0 | 26.0 |
| 14 | 05:39:37.57 | -69:08:25.22 | 296.5 | -141.4 | 96.0 | 63.0 |
| 15 | 05:39:23.05 | -69:08:33.57 | 218.4 | -149.8 | 31.0 | 310.0 |
| 16 | 05:39:19.76 | -69:08:21.01 | 200.7 | -137.2 | 14.4 | 29.2 |
| 17 | 05:38:58.60 | -69:09:36.36 | 87.0 | -212.6 | 63.8 | 16.9 |
| 18 | 05:38:32.82 | -69:09:17.55 | -51.6 | -193.8 | 63.8 | 340.7 |
| 20 | 05:39:03.35 | -69:08:04.44 | 112.5 | -120.6 | 13.5 | 67.9 |
| 21 | 05:39:09.79 | -69:04:36.61 | 147.1 | 87.2 | 18.3 | 142.7 |
| 22 | 05:38:52.60 | -69:04:40.27 | 54.7 | 83.5 | 20.3 | 128.7 |
| 23 | 05:38:44.74 | -69:04:19.25 | 12.5 | 104.5 | 20.3 | 120.0 |
| 24 | 05:38:37.67 | -69:04:27.59 | -25.5 | 96.2 | 13.6 | 45.0 |
| 25 | 05:38:39.17 | -69:03:31.66 | -17.5 | 152.1 | 25.9 | 90.0 |
| 26 | 05:38:28.95 | -69:02:54.60 | -72.4 | 189.2 | 29.8 | 25.7 |
| 27 | 05:38:23.40 | -69:02:24.23 | -102.2 | 219.6 | 62.5 | 111.4 |
| 28 | 05:38:12.58 | -69:02:16.68 | -160.4 | 227.1 | 50.4 | 66.2 |
| 29 | 05:38:10.17 | -69:02:44.58 | -173.4 | 199.2 | 11.4 | 61.0 |
| 30 | 05:38:07.60 | -69:03:16.01 | -187.2 | 167.8 | 15.7 | 39.1 |
| 31 | 05:38:14.24 | -69:03:29.95 | -151.5 | 153.8 | 38.8 | 53.0 |
| 32 | 05:38:38.16 | -69:00:34.55 | -22.9 | 329.2 | 28.8 | 63.8 |

| Table 2.7 (cont'd). | | | | | | |
|---|---|---|---|---|---|---|
| 32 | 05:38:04.92 | -69:04:38.91 | -201.6 | 84.9 | 9.2 | 26.3 |
| 33 | 05:38:34.69 | -69:01:05.06 | -41.6 | 298.7 | 20.8 | 32.5 |
| 1* | 05:37:57.50 | -69:07:44.65 | -241.5 | -100.9 | 107.0 | 322.2 |
| 2* | 05:38:09.50 | -69:08:58.47 | -177.0 | -174.7 | 83.8 | 298.5 |
| 3* | 05:38:19.48 | -69:09:55.73 | -123.3 | -231.9 | 54.8 | 343.7 |
| 4* | 05:38:06.23 | -69:10:47.75 | -194.5 | -284.0 | 54.8 | 60.8 |
| 5* | 05:37:58.58 | -69:08:32.56 | -235.7 | -148.8 | 18.4 | 317.2 |

Table 2.8 - Catalog of bright dense pillars and protruding IFs. Each pillar has an ID, RA and Dec ( J2000), length and position angle.

| Table 2.8 – Catalog of Bright Dense Pillars and protruding IF | | | | | | |
|---|---|---|---|---|---|---|
| Piller ID | RA ( 2000) | Dec (2000) | Δ RA | δ Dec | Length | PA |
| 1 | 05:37:28.35 | -69:01:51.86 | -400 | 252 | 37 | 216 |
| 2 | 05:37:30.68 | -69:04:12.44 | -384 | 111 | 17 | 120 |
| 3 | 05:37:32.85 | -69:04:16.79 | -373 | 107 | 19 | 115 |
| 4 | 05:37:42.14 | -69:02:30.70 | -325 | 213 | 26 | 209 |
| 5 | 05:37:42.85 | -69:04:42.79 | -319 | 81 | 10 | 176 |
| 6 | 05:37:42.95 | -69:04:34.28 | -319 | 90 | 10 | 183 |
| 7 | 05:37:50.28 | -69:06:02.92 | -282 | 1 | 19 | 155 |
| 8 | 05:37:54.67 | -69:05:09.56 | -255 | 54 | 9 | 167 |
| 9 | 05:37:58.57 | -69:03:44.17 | -233 | 140 | 7 | 182 |
| 10 | 05:37:59.29 | -69:05:49.22 | -233 | 15 | 8 | 163 |
| 11 | 05:38:03.81 | -69:05:22.05 | -207 | 42 | 10 | 164 |
| 12 | 05:38:05.74 | -69:06:36.40 | -196 | -33 | 6 | 138 |
| 13 | 05:38:08.17 | -69:06:51.16 | -185 | -47 | 33 | 167 |
| 14 | 05:38:09.49 | -69:07:05.29 | -180 | -61 | 19 | 159 |
| 15 | 05:38:11.95 | -69:07:08.39 | -164 | -65 | 26 | 142 |
| 16 | 05:38:13.19 | -69:04:25.76 | -158 | 98 | 13 | 236 |
| 17 | 05:38:14.22 | -69:07:00.28 | -153 | -56 | 10 | 131 |
| 18 | 05:38:15.89 | -69:05:25.19 | -142 | 39 | 6 | 260 |
| 19 | 05:38:17.03 | -69:05:57.00 | -137 | 7 | 3 | 112 |
| 20 | 05:38:17.56 | -69:05:02.66 | -131 | 61 | 14 | 200 |
| 21 | 05:38:24.12 | -69:04:56.88 | -99 | 67 | 24 | 206 |
| 22 | 05:38:28.52 | -69:08:26.14 | -72 | -142 | 16 | 166 |
| 23 | 05:38:28.74 | -69:03:37.29 | -72 | 147 | 6 | 238 |
| 24 | 05:38:30.07 | -69:08:38.73 | -67 | -155 | 24 | 138 |
| 25 | 05:38:33.14 | -69:06:02.88 | -51 | 1 | 5 | 153 |
| 26 | 05:38:34.01 | -69:03:33.01 | -45 | 151 | 12 | 268 |
| 27 | 05:38:34.26 | -69:06:26.96 | -45 | -23 | 12 | 153 |
| 28 | 05:38:36.05 | -69:07:43.52 | -35 | -100 | 12 | 148 |
| 29 | 05:38:38.27 | -69:08:13.16 | -24 | -129 | 9 | 81 |
| 30 | 05:38:40.51 | -69:09:58.77 | -8 | -235 | 9 | 111 |
| 31 | 05:38:40.97 | -69:07:27.27 | -8 | -83 | 12 | 84 |
| 32 | 05:38:43.16 | -69:07:04.03 | 3 | -60 | 7 | 96 |
| 33 | 05:38:43.20 | -69:01:19.02 | 3 | 285 | 15 | 173 |
| 34 | 05:38:43.23 | -69:10:21.48 | 3 | -258 | 11 | 132 |
| 35 | 05:38:44.16 | -69:06:58.89 | 8 | -55 | 5 | 90 |
| 36 | 05:38:44.25 | -69:11:10.68 | 8 | -307 | 9 | 127 |
| 37 | 05:38:45.18 | -69:05:05.74 | 14 | 58 | 8 | 304 |
| 38 | 05:38:45.41 | -69:04:19.41 | 14 | 104 | 8 | 268 |
| 39 | 05:38:45.65 | -69:10:25.07 | 19 | -261 | 18 | 108 |
| 40 | 05:38:45.85 | -69:09:51.28 | 19 | -227 | 15 | 62 |
| 41 | 05:38:46.15 | -69:07:04.11 | 19 | -60 | 8 | 86 |
| 42 | 05:38:46.86 | -69:09:33.58 | 25 | -210 | 7 | 73 |
| 43 | 05:38:47.05 | -69:07:56.66 | 25 | -113 | 13 | 61 |
| 44 | 05:38:47.85 | -69:07:15.15 | 30 | -71 | 14 | 65 |
| 45 | 05:38:50.55 | -69:10:17.26 | 46 | -253 | 16 | 77 |
| 46 | 05:38:53.45 | -69:08:00.23 | 57 | -116 | 8 | 70 |
| 47 | 05:38:54.71 | -69:05:36.11 | 68 | 28 | 3 | 343 |
| 48 | 05:38:55.01 | -69:05:39.94 | 68 | 24 | 3 | 309 |
| 49 | 05:38:55.29 | -69:05:40.63 | 68 | 23 | 3 | 267 |

| Table 2.8 (cont'd). | | | | | | |
|---|---|---|---|---|---|---|
| 50 | 05:38:56.40 | -69:07:21.25 | 73 | -77 | 13 | 30 |
| 51 | 05:38:56.81 | -69:05:30.58 | 78 | 33 | 10 | 297 |
| 52 | 05:38:57.29 | -69:01:56.18 | 78 | 248 | 5 | 32 |
| 53 | 05:38:57.51 | -69:06:27.65 | 84 | -24 | 16 | 16 |
| 54 | 05:38:57.81 | -69:07:56.53 | 84 | -113 | 19 | 68 |
| 55 | 05:38:58.07 | -69:01:51.67 | 84 | 252 | 7 | 23 |
| 56 | 05:38:58.58 | -69:02:16.27 | 89 | 228 | 9 | 233 |
| 57 | 05:38:58.84 | -69:07:28.60 | 89 | -85 | 15 | 43 |
| 58 | 05:38:59.48 | -69:08:04.34 | 89 | -121 | 37 | 67 |
| 59 | 05:39:00.01 | -69:11:45.42 | 95 | -342 | 22 | 83 |
| 60 | 05:39:00.14 | -69:06:08.15 | 95 | -4 | 6 | 340 |
| 61 | 05:39:00.29 | -69:08:56.01 | 95 | -172 | 21 | 52 |
| 62 | 05:39:02.13 | -69:08:22.12 | 105 | -138 | 17 | 46 |
| 63 | 05:39:02.47 | -69:06:40.10 | 105 | -36 | 17 | 29 |
| 64 | 05:39:03.49 | -69:07:31.02 | 111 | -87 | 19 | 33 |
| 65 | 05:39:04.13 | -69:08:14.74 | 116 | -131 | 23 | 57 |
| 66 | 05:39:05.07 | -69:05:54.83 | 121 | 9 | 7 | 279 |
| 67 | 05:39:07.00 | -69:10:49.34 | 132 | -286 | 7 | 39 |
| 68 | 05:39:07.51 | -69:10:26.01 | 138 | -262 | 14 | 12 |
| 69 | 05:39:08.05 | -69:08:47.38 | 138 | -164 | 18 | 53 |
| 70 | 05:39:11.46 | -69:08:15.27 | 154 | -131 | 9 | 49 |
| 71 | 05:39:11.76 | -69:10:53.42 | 159 | -290 | 14 | 55 |
| 72 | 05:39:12.36 | -69:07:44.75 | 159 | -101 | 13 | 26 |
| 73 | 05:39:13.25 | -69:08:56.22 | 164 | -172 | 9 | 91 |
| 74 | 05:39:14.28 | -69:01:45.16 | 170 | 259 | 23 | 308 |
| 75 | 05:39:14.63 | -69:10:54.29 | 175 | -290 | 24 | 54 |
| 76 | 05:39:14.72 | -69:07:39.20 | 175 | -95 | 13 | 37 |
| 77 | 05:39:16.70 | -69:05:28.48 | 186 | 35 | 8 | 350 |
| 78 | 05:39:17.98 | -69:10:36.02 | 191 | -272 | 11 | 32 |
| 79 | 05:39:18.95 | -69:05:56.61 | 197 | 7 | 11 | 355 |
| 80 | 05:39:18.97 | -69:07:45.44 | 197 | -102 | 8 | 63 |
| 81 | 05:39:19.05 | -69:07:45.59 | 197 | -102 | 8 | 55 |
| 82 | 05:39:21.91 | -69:04:31.65 | 213 | 92 | 15 | 335 |
| 83 | 05:39:22.10 | -69:05:27.13 | 213 | 37 | 18 | 341 |
| 84 | 05:39:22.91 | -69:06:08.13 | 218 | -4 | 7 | 359 |
| 85 | 05:39:23.79 | -69:07:00.26 | 224 | -56 | 24 | 14 |
| 86 | 05:39:24.53 | -69:04:45.88 | 229 | 78 | 9 | 339 |
| 87 | 05:39:26.37 | -69:05:59.02 | 234 | 5 | 15 | 27 |
| 88 | 05:39:26.59 | -69:04:42.32 | 240 | 81 | 4 | 344 |
| 89 | 05:39:26.62 | -69:07:32.13 | 240 | -88 | 22 | 28 |
| 90 | 05:39:27.52 | -69:06:11.28 | 245 | -7 | 9 | 349 |
| 91 | 05:39:27.79 | -69:04:04.10 | 245 | 120 | 28 | 320 |
| 92 | 05:39:30.83 | -69:05:55.85 | 261 | 8 | 20 | 25 |
| 93 | 05:39:30.85 | -69:10:11.75 | 261 | -248 | 19 | 44 |
| 94 | 05:39:31.05 | -69:05:29.34 | 261 | 34 | 8 | 341 |
| 95 | 05:39:31.14 | -69:05:24.43 | 261 | 39 | 6 | 330 |
| 96 | 05:39:31.23 | -69:05:20.09 | 261 | 44 | 16 | 357 |
| 97 | 05:39:34.55 | -69:05:25.43 | 283 | 38 | 6 | 324 |
| 98 | 05:39:37.13 | -69:07:28.57 | 293 | -85 | 13 | 12 |
| 99 | 05:39:37.64 | -69:07:19.20 | 299 | -75 | 10 | 13 |
| 100 | 05:39:37.86 | -69:07:09.53 | 299 | -66 | 8 | 8 |
| 101 | 05:39:39.19 | -69:11:25.06 | 304 | -321 | 7 | 240 |
| 102 | 05:39:39.53 | -69:08:34.63 | 310 | -151 | 5 | 29 |

| Table 2.8 (cont'd). | | | | | | |
|---|---|---|---|---|---|---|
| 103 | 05:39:39.73 | -69:08:31.87 | 310 | -148 | 4 | 58 |
| 104 | 05:39:39.77 | -69:11:25.05 | 310 | -321 | 12 | 258 |
| 105 | 05:39:44.91 | -69:06:49.21 | 336 | -45 | 17 | 2 |
| 106 | 05:39:47.81 | -69:08:49.79 | 353 | -166 | 39 | 19 |

Table 2.9 - Cataloged massive stars in 30 Dor with spectral types.

| **Table 2.9: Ionizing Stars in 30 Dor** | | | |
|---|---|---|---|
| Spec Type | Number | Spec Type | Number |
| O3Ia | 3 | O7V | 16 |
| O3III | 12 | O8.5V | 26 |
| O3V | 22 | O8V | |
| O4V | 28 | O9V | 21 |
| O5V | 11 | | |
| O6V | 12 | WR | 19 |

Table 2.10. Abundaces of Selected Elements

| **Table 2.10**<br>**Abundances of Selected Elements** | | | | | |
|---|---|---|---|---|---|
| He | O | N | S | Ar | ref |
| ---- | -3.6 | -5.1 | -5.3 | -5.8 | Garnett (1999) (for full LMC) |
| -1.05 | -3.75 | -5.42 | -5.16 | -5.86 | Vermeij et al. 2002 |
| -1.07 | -3.5 | -4.79 | -5.01 | -5.74 | Peimbert (P03) |
| ---- | ---- | ---- | -5.23 | -5.68 | Lebouteiller et al. 2008 |
| ----- | -3.69 | -5.21 | -5.32 | -5.84 | Mathis, Chu & Peterson |
| -1.1 | -3.6 | -4.87 | -5.19 | -5.89 | Tsamis & Pequngnot (TP05) |
| -1.08 | -3.75 | -4.91 | -5.32 | -5.99 | Adopted Here |
| Units of $Log_{10}$ [N(X) / N(H)]. | | | | | |

Table. 2.11 X-ray pressures of selected regions in 30 Doradus. The region number corresponds to the regions identified in Townsley et al. 2006.

| **Table 2.11**<br>**X-ray Pressures of Selected Regions in 30 Doradus** | |
|---|---|
| Region Number<br>Townsley et al. 2006 | Pressure[1] × $10^{10}$ |
| 1 | 1.7 |
| 2 | 1.3 |
| 3 | 3.0 |
| 4 | 10.2 |
| 5 | 7.9 |
| 6 | 10.0 |
| 7 | 13.4 |
| 8 | 7.9 |
| 9 | 7.2 |
| 10 | 5.8 |
| 12 | 5.0 |
| 13 | 6.0 |
| 14 | 6.6 |
| 15 | 5.6 |
| 16 | 2.8 |
| 17 | 2.4 |
| 20 | 3.0 |
| 22 | 1.5 |
| 24 | 1.4 |
| [1]Units of dyne $cm^{-2}$ | |

Table 2.12 Abundance Ratios from Different Studies.

| **Table 2.12**<br>**Abundance Ratios from Different Studies** | | |
|---|---|---|
| N/O | N/S | Reference |
| -1.50 | 0.20 | Garnett (1999) (for full LMC) |
| -1.67 | -0.26 | Vermeij et al. 2002 |
| -1.29 | 0.22 | Peimbert (P03) |
| -1.52 | 0.11 | Mathis, Chu & Peterson |
| -1.27 | 0.32 | Tsamis & Pequngnot (TP05) |
| -1.16 | 0.41 | Adopted Here |

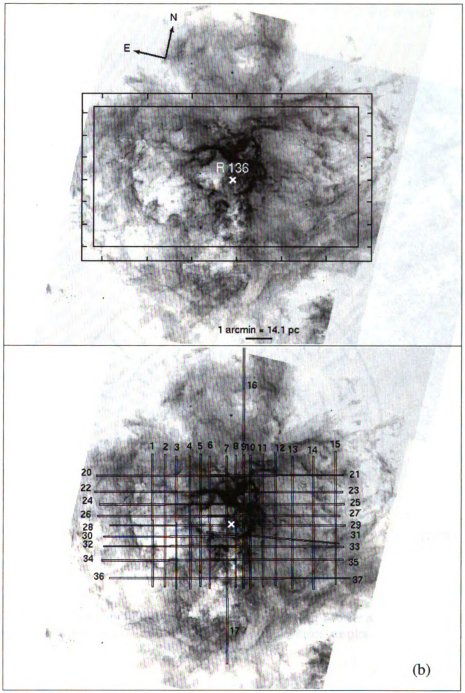


Figure 2.1. - New narrow band Ha image of 30 Dor from the SOAR telescope rotated 13 degrees. The center of R136 is marked as a white cross. a) the outline of the region covered by our maps made from the Blanco spectra; b): The individual slit positions of our Blaco spectroscopic data set.

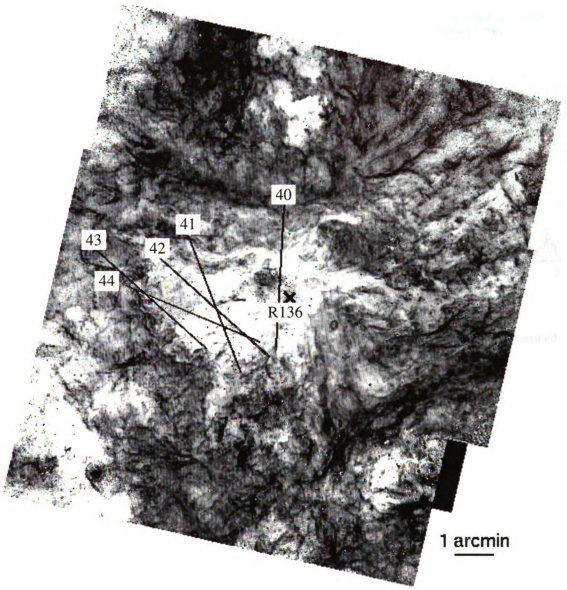


Figure 2.2. - Ratio of SOAR Hα / [S II] images where darker indicates a lower ratio. The orientation is the same as Figure 2.1. For reference the SOAR spectroscopic slit positions are plotted on top of the image.

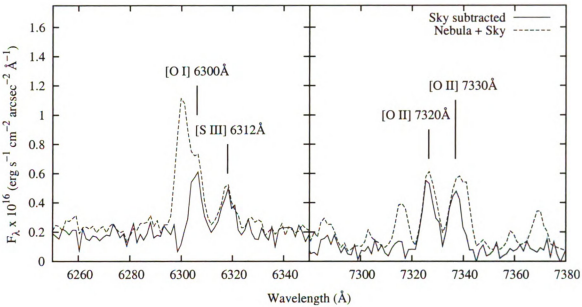


Figure 2.3. - A sample SOAR spectrum near [O I] λ6300 and [O II] λλ7320,7330. The solid and dashed lines respectively show the spectrum after and before sky subtraction.

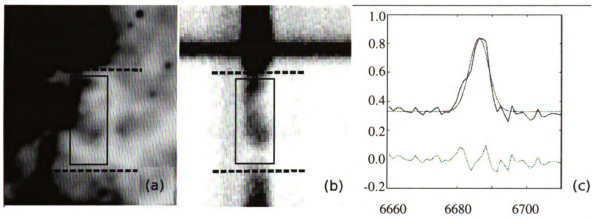


Figure 2.4. - A demonstration of the source of the line profile shapes with a wide slit width. Panel a is a 2D image of the sky in Hα emission. The box represents the region on the sky the spectrum in panel b was extracted. Panel b is the 2D spectrum at the same scale as panel a. Panel c is the line profile for the region extracted. The solid line shows the data of the He I λ6678 at the LMC redshift. The top dashed line is the best Gaussian fit and the bottom is the residual of that fit.

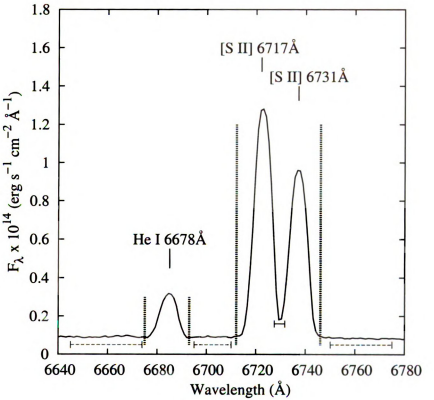


Figure 2.5. - Two examples of extraction windows used to measure line flux. He I λ6678 shows an isolated emission line. The [S II] doublet is slightly blended. Between the two peaks of the [S II] indicated by a horizontal bar, a search is performed for the minimum to define the wings of each emission line as described in the text.

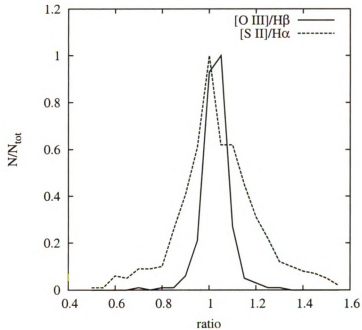


**Figure 2.6. - Repeatability of results at overlapping points along different Blanco slit positions. The curves are his**tograms of the distributions of ratios of intensity ratios; for example the [O III]/Hβ measured from **one sli**t position is divided by the [O III]/Hβ measure at the same position on the sky but from a different **slit po**sition.

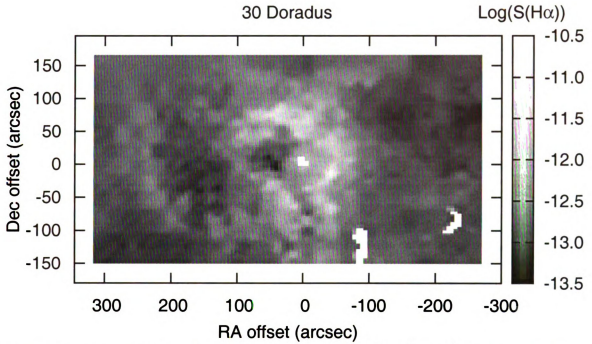


Figure 2.7a - Interpolated dereddened Ha surface brightness in erg $s^{-1}$ $cm^{-2}$ $arcsec^{-2}$. The region shown is the same as that outlined in Figure 2.1 and figures 7b – 7g.

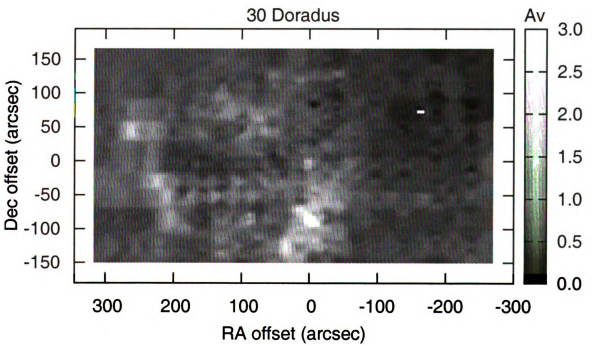


Figure 2.7b - Interpolated $A_V$.

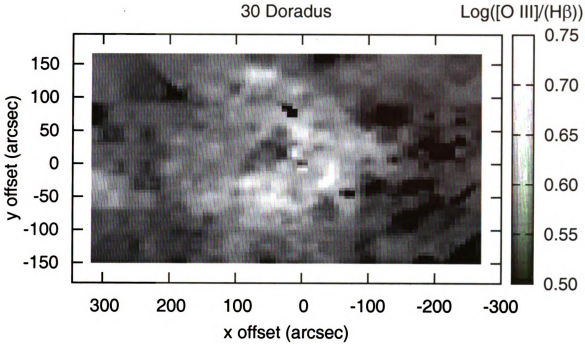


Figure 2.7c - Log([O III]/Hβ).

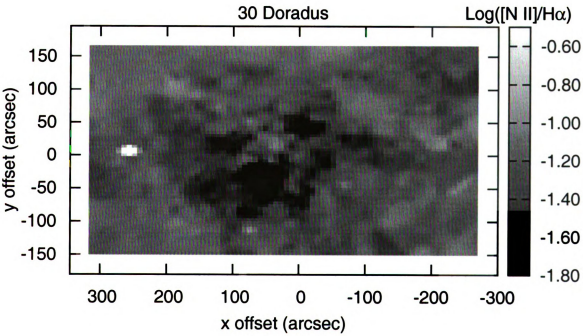


Figure 2.7d – Log([N II]/Hα)

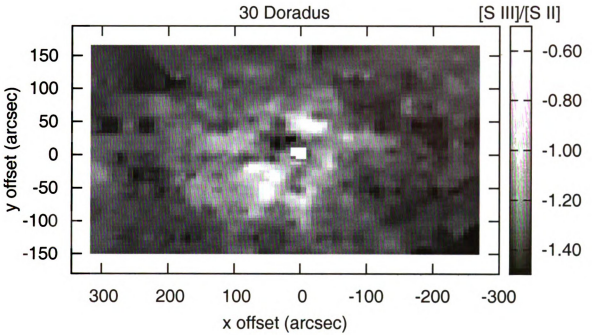


Figure 2.7e – Log ([S III] λ6312 / ([S II] λ6716+λ6731))

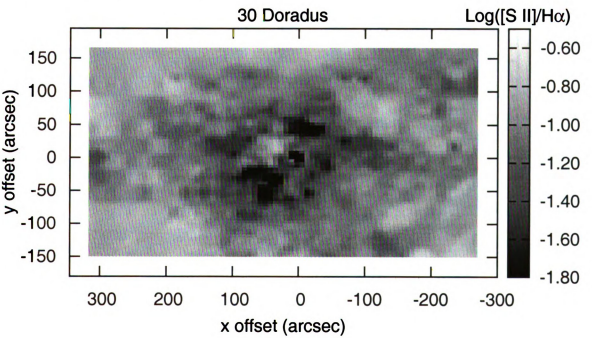


Figure 2.7f – Log ( ([S II] λ6716+λ6731) / Hα ).

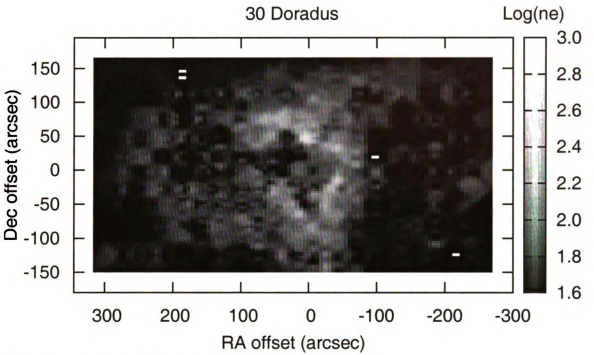


Figure 2.7g - Log $n_e$ in $cm^{-3}$ measured from the [S II] λ6716/λ6731 ratio.

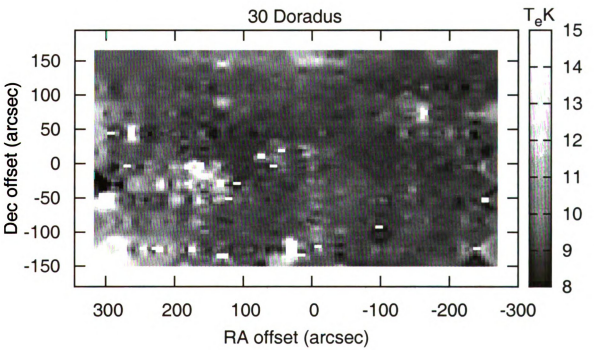


Figure 2.7h – Temperatures measured from *R* defined in equation 5. The scale is shown in increments of 1,000K.

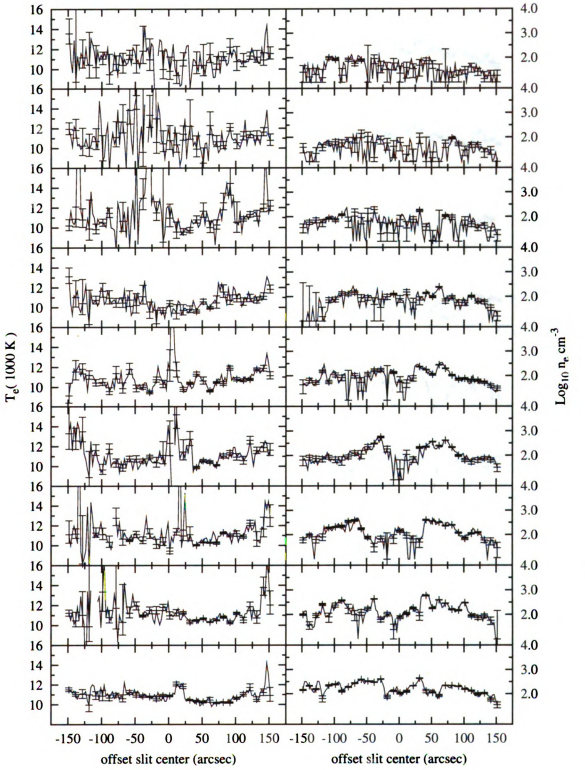


Figs. 2.8a – 2.8d – The temperature and density profiles for our Blanco slit positions. From top to bottom Figure 2.8a shows positions 1-9. These figures are further described in the text.

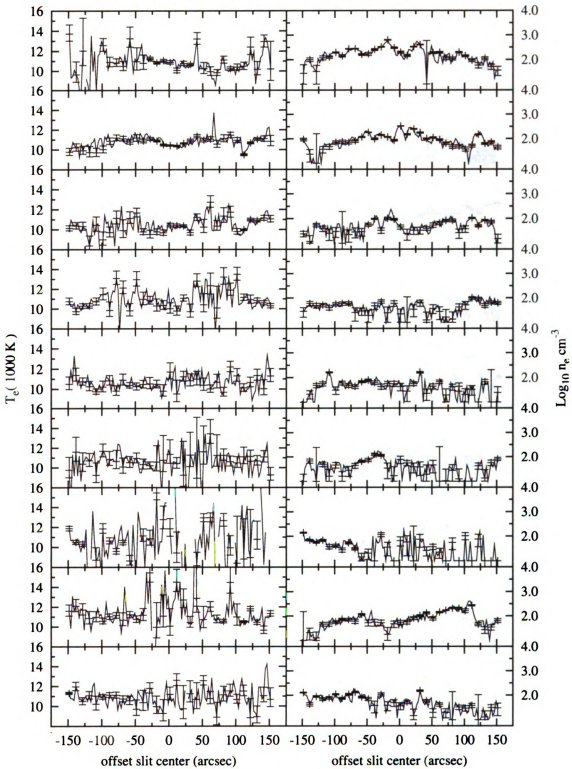


Figure 2.8b – Temperature and density along Blanco slit positions 10 – 17 and position 20.

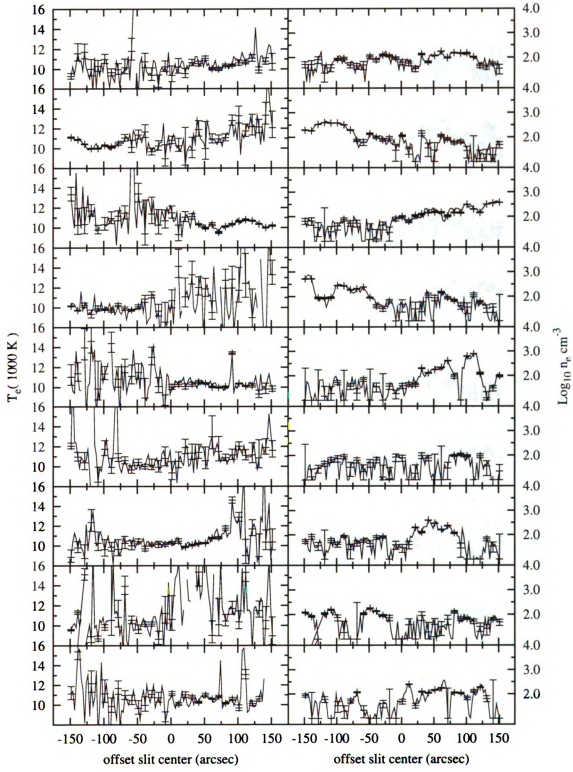


Figure 2.8c – Temperature and density along Blanco slit positions 21-29.

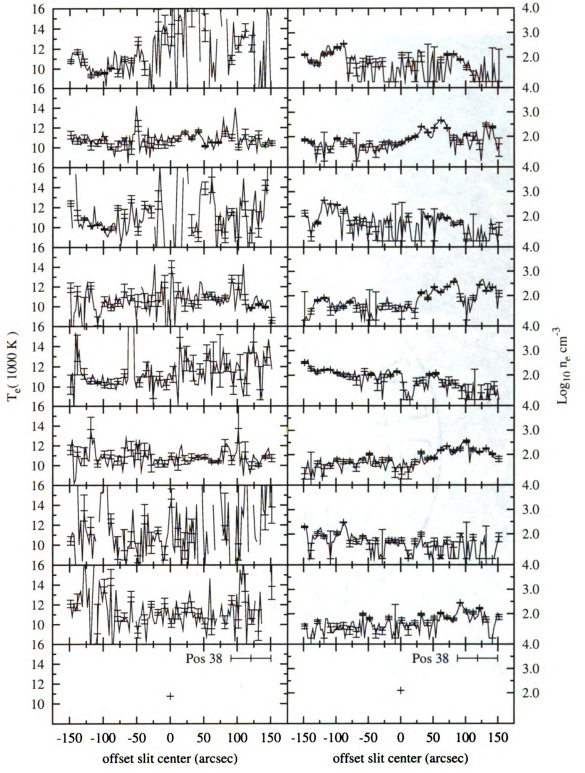


Figure 2.8d – Temperature and density along Blanco slit positions 30-38.

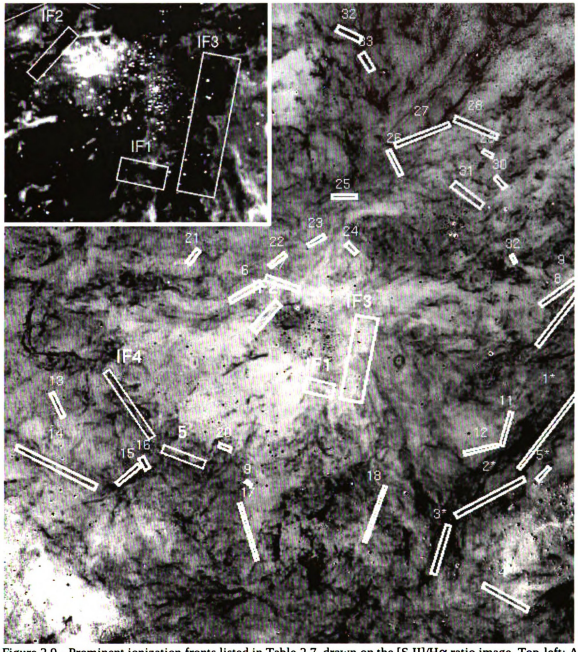


Figure 2.9 - Prominent ionization fronts listed in Table 2.7, drawn on the [S II]/Hα ratio image. Top-left: A blow up of the central region around R136 including IFs 1 and 2.

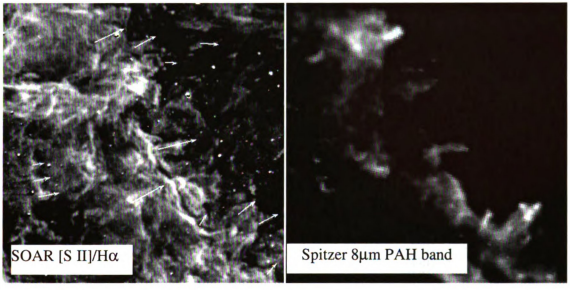


Figure 2.10 - Left SOAR [S II]/Hα; Right SPITZER 8μm PAH. A selection of bright pillars are shown with arrows indicating their location and direction. These Dense IF are detected in both optical and IR passbands and show a connection with the background molecular cloud.

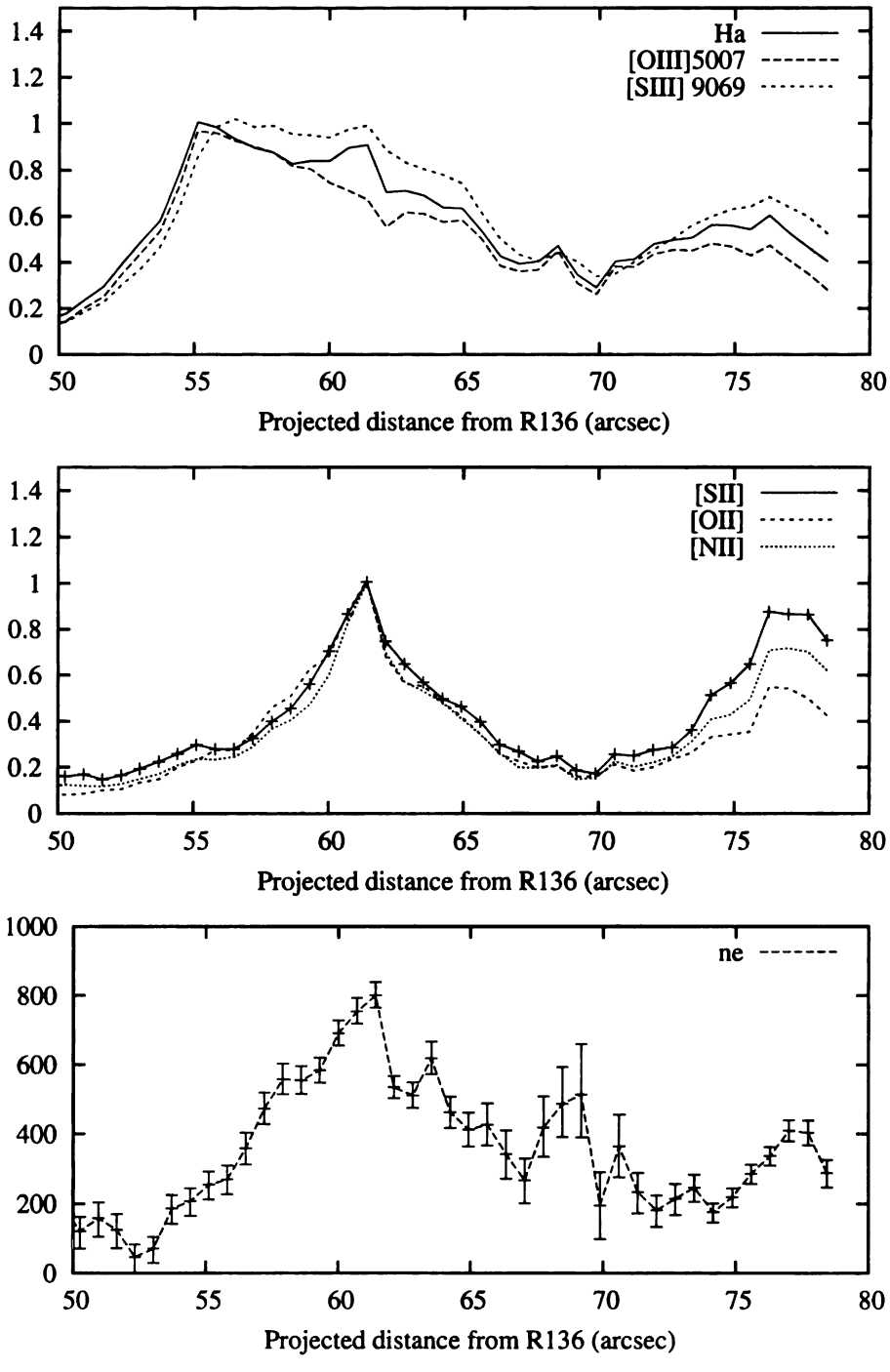


Figure 2.11 - The profile of IF1. Top: Ionized gas is traced by Hα, [OIII] and [S III] emission. Middle: The IF is traced by [S II], [N II] and [O II]. Bottom: The electron density profile measured from [S II] as described in the text.

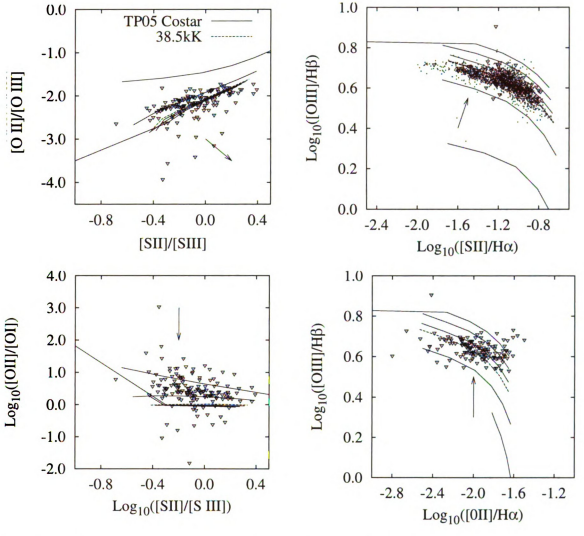


Figure 2.12 - Plots of diagnostic line ratios with observations from SOAR and Blanco spectra. Lines represent photoionization models with ne 200 $cm^{-3}$. Arrows indicate the effect increasing the modeled SED temperature has on the line ratios. From top left to bottom right: (a) [SII]/[ SIII] vs. [O II]/[O III]; (b) [SII]/Hα vs [OIII]/Hβ; (c) [SII]/[S III] vs. [OII]/[OI]; (d) [O II]/Hα vs [O III]/Hβ.

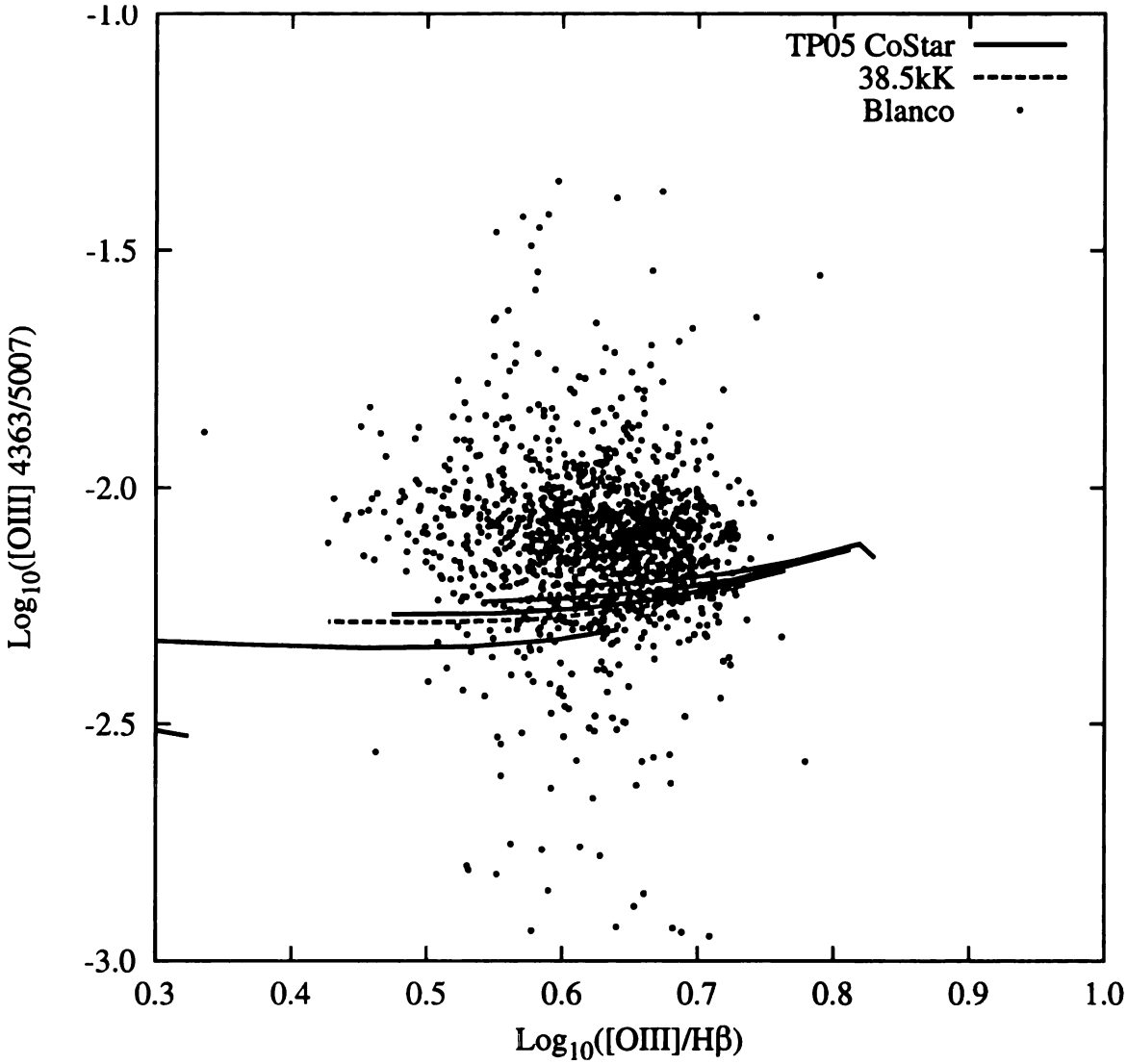


Figure 2.13 - Predicted and observed [O III] λ4363/λ5007 ratios for models with TP05 abundances.

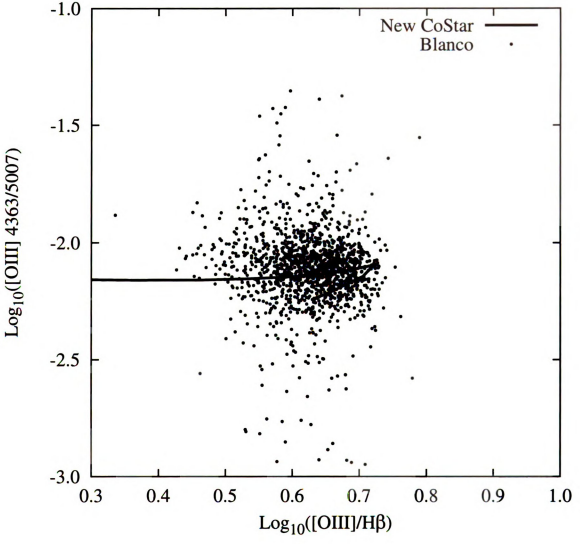


Figure 2.14 - Similar to Figure 2.13 but with modeled with our adopted abundances.

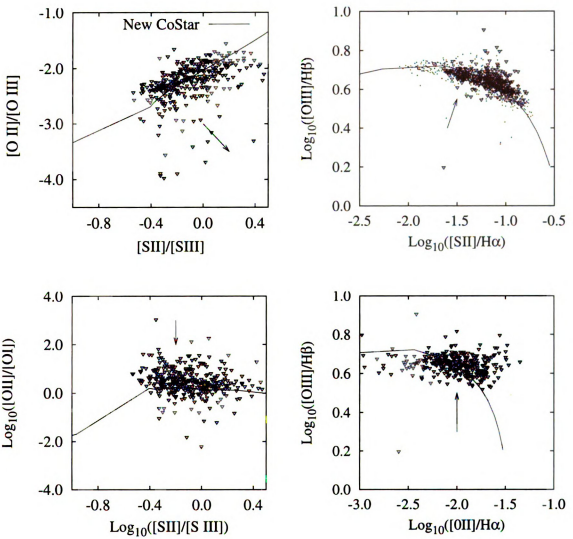


Figure 2.15 – Various predicted and Observed line ratios described as described in Figure 2.12 using our adopted abundances.

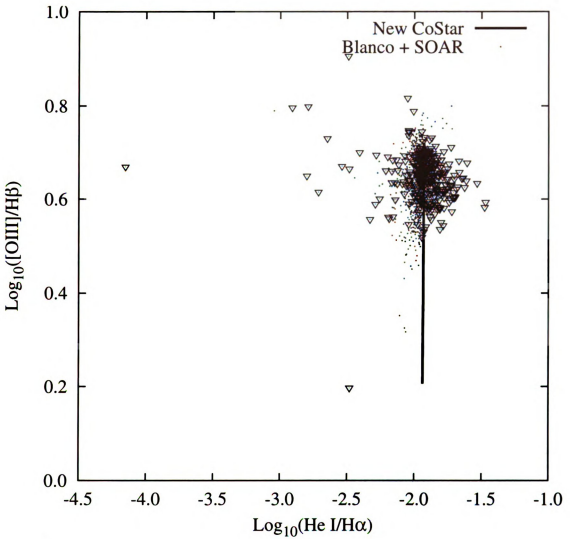


Figure 2.16 - Predicted and Observed intensity ratio of He I λ6678 / Hα.

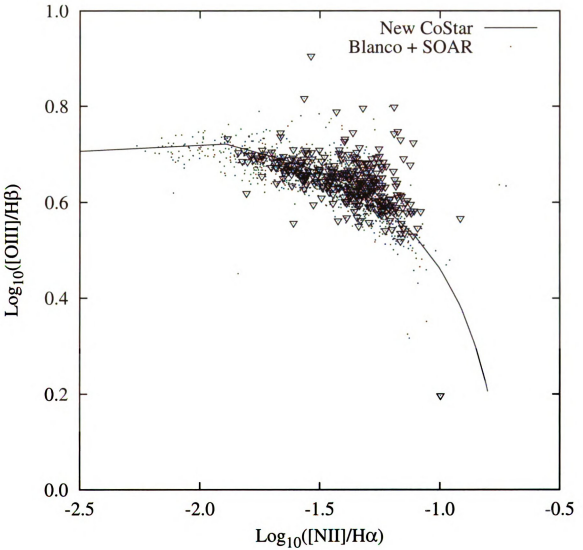


Figure 2.17 - Predicted and Observed intensity ratio of the commonly used [N II] λ6584/Hα diagnostic.

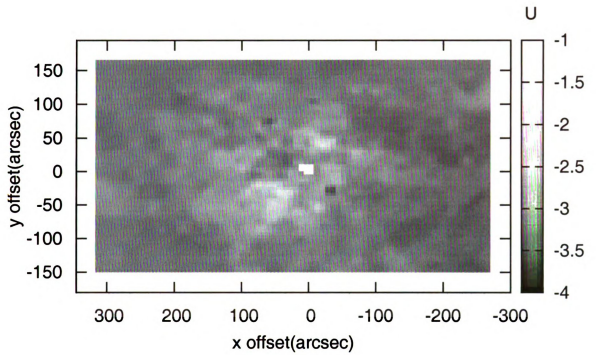


Figure 2.18 - An interpolated map of the dimensionless quantity *U*, derived from fitting models to our Blanco spectra. Region mapped is the same describing Figs. 2.7a – 2.7h.

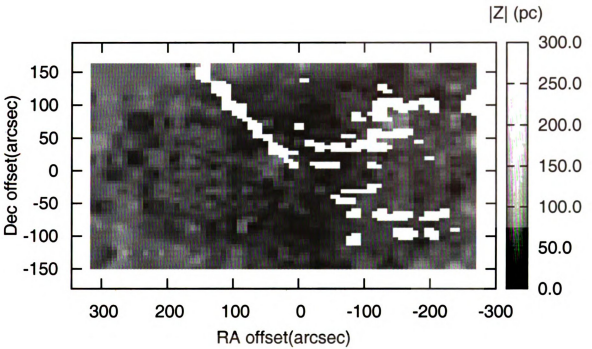


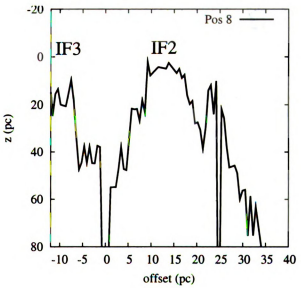


Figure 2.19 – Top: Map of $|z|$ , defined in Eq. 12. Bottom: Profile of z for position 8. The offset in the declination offset from R136. By definition the height of R136 is z = 0.

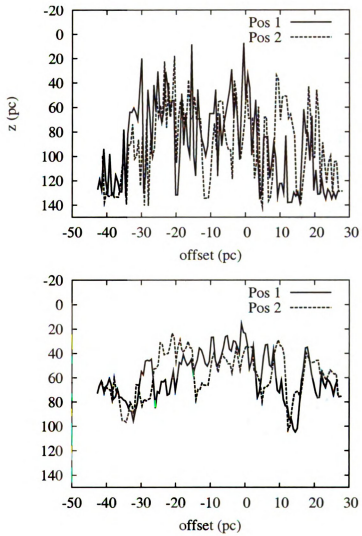


Figure 2.20 -Profile of |z| in slit positions 1 and 2. Top: |z| from the best fitting model; bottom : |z| calculated from equation 13 assuming a smooth density distribution.

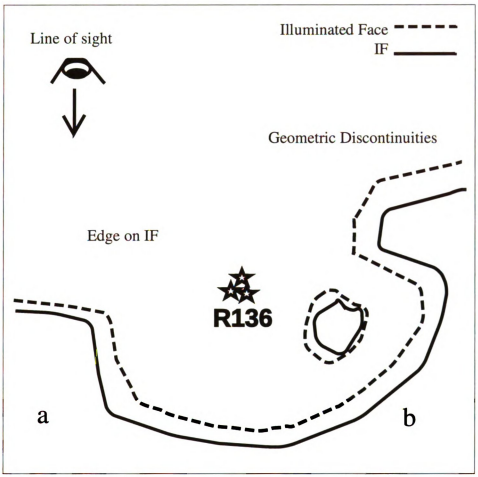


Figure 2.21 - A cartoon of possible geometries in 30 Doradus consistent with the changes in $U$ across the nebula. The region labeled "a" is a continuos ionization front of finit height, seen edge on, facing the ionizing cluster. Region "b" represents possible geometries that would be seen as discontinuities in modeled $R$ or $|z|$.

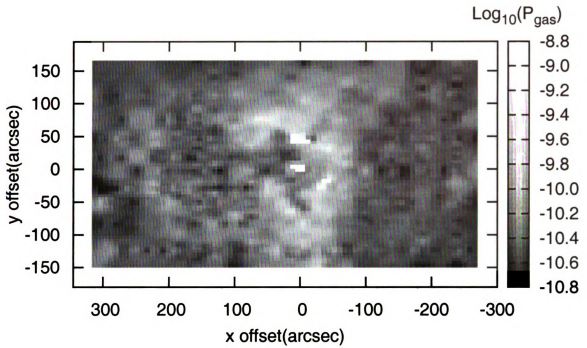


Figure 2.22 - Observed thermal gas pressure interpolated from the Blanco spectra.

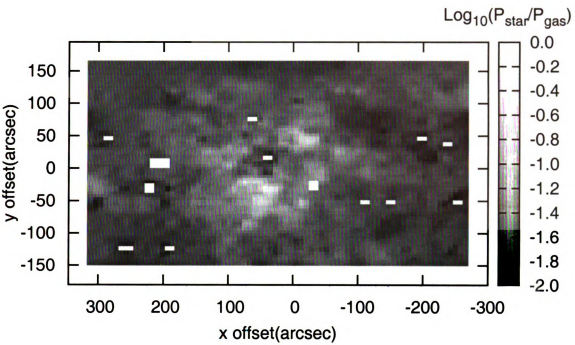


Figure 2.23 – The ratio of pressure from integrated star light (Eq. 17) to gas pressure.

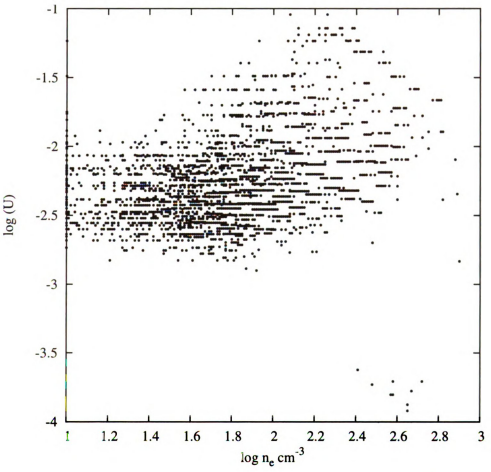


Figure 2.24 - Observed gas density vs modeled ionization parameter U.

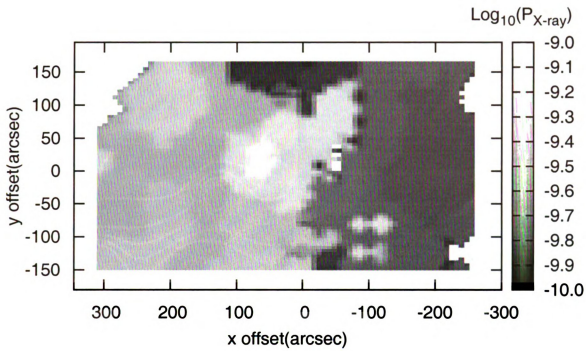


Figure 2.25 – $P_{\text{X-ray}}$ from the regions of diffuse x-ray emission described in Townsley et al. (2006). The pressure was calculated using the reported $T_{\text{X-ray}}$, surface brightness and area.

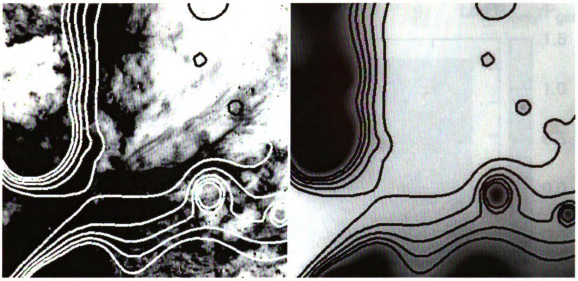

**Figure 2.26 – The r**egion discussed in section 6.3.4 demonstrating an outflow. The contours in both left and **right represent the s**oft, diffuse x-ray emission. Left: SOAR [S II]; Right:0.5 – 0.7 keV emission. The x-ray **data was made avail**able by Liesa Townsley.

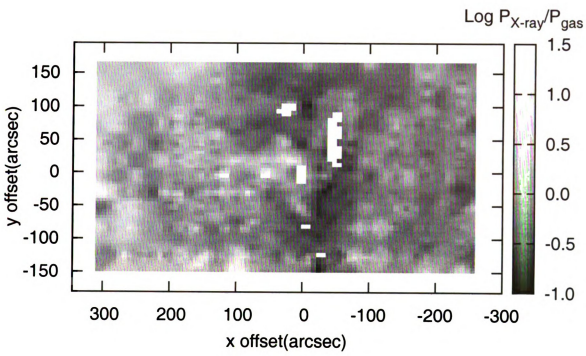


Figure 2.27 – The ratio of $P_{x\text{-}ray}$ to $P_{gas}$.

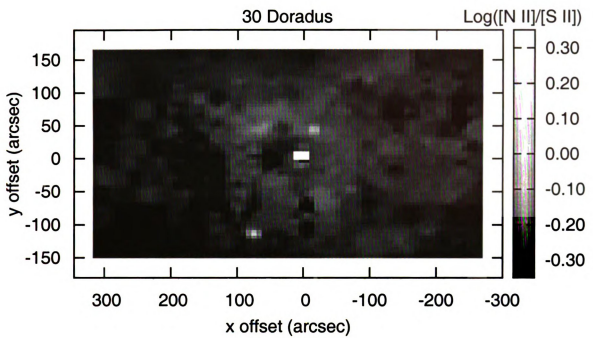


Figure 2.28 - The spatial distribution of the [N II] λ6584 / [S II] (λ6716 + λ6731) ratio.

**References**


Adelman-McCarthy, J. K., et al., 2006, ApJS, 162, 38

Baldwin, J. A., Phillips, M. M., & Terlevich, R., 1981, PASP, 93, 5 (BPT)

Bresolin, F., Gieren, W., Kudritzki, R., Pietrzynski, G., Urbaneja, M. A., Carroro, G., 2009, ApJ, 700, 309

Cardelli, J. A., Clayton, G. C., Mathis, J. S., 1989, ApJ, 345, 245

Chu, Y., and Kennicutt, R. C. 1994, ApJ, 425, 720

Crowther, P. A., 2007, ARA&A 45, 177

Davis, L., Jr., & Greenstein, J. L., 1951, ApJ, 114, 206

Dopita, M. A., Fischera, J., Sutherland, R. S. 2006, ApJ, 167, 177

Dobashi, K., Bernard, J. P., Paradis, D., Reach, W. T., Kawamura, A., 2008, A&A, 484,205

Garnett, D. R. 1999, IAUS, 190, 266

Heap, S.R., Lanz, T. & Hubeny, I. 2006, ApJ, 638, 409

Hu, E. M., Cowie, L. L., Kakazu, Y. Barger, A., 2009, ApJ, 698, 2014

Indebetouw, R., et al. 2009, ApJ, 694, 84 ( I09)

Kewley, L. J., Geller, M. J., Jansen, R. A., & Dopita, M. A. 2002, AJ, 124, 3135

Kewley, L.J. & Ellison, S.L. 2008, ApJ, 681, 1183

Krabbe, A. C., and Copetti, M. V. F, 2002, A&A, 387, 295

Landi, E., & Landini, M., 1999, A&A, 347, 401

Lazendic, J. S., Dickel, J.R., & Jones, P. A., 2003, ApJ, 569, 287

Lebouteiller, V., Bernard-Salas, J., Brandl, B., Whelan, et al., 2008, ApJ, 680, 398

Marci, M. L., Stanek, K. Z., Bersier, D., Greenhill, L. J., Reid, M. J., 2006, ApJ, 652,1133

Massey, P., et al., 2009, ApJ, 692, 618

Mathis, J. S., Chu, Y.H. and Peterson, D. E., 1985, ApJ, 292, 155

Meixner, M., et al., 2006, AJ, 132, 2268

Nakajima, Y., Kandori, R., Tamura, M. Kusakabe, N. Hashimoto, J., Nagayma, T., Nagata, T., Hatano, H., Kata, D., Hough, H., 2007, PASJ, 59, 519

Osterbrock, D.E. & Ferland, G. J., 2006, Astophysics of Gaseous Nebula and Active Galactic Nuclei 2nd Edition, Sausalito, California: University Science Books (AGN3)

Oey, M. S., Dopita, M. A., Sheilds, J. C., Smith, R. C., 2000, ApJS, 128, 511

Pagel, B. E. J., Edmunds, M. G., Blackwell, D. E., Chun, M. S., & Smith, G., 1997, MNRAS, 189, 95

Pagel, B. E. J., Simonson, E. A., Terlevich, R. J. & Edmonds, M., 1992, MNRAS, 255, 325

Peimbert, A., 2003, ApJ, 584, 735 (P03)

Pellegrini, E. W., Baldwin, J. A., Ferland, G., to submitted MNRAS, 2009

Pettini, M., Ellison, S.L., Bergeron, J & Petitjean, P. 2002, A&A, 391, 21.

Pettini, M., Pagel, B., 2004, MNRAS, 348, L59

Poglitsch, A, et al., 1995, ApJ, 454, 293

Rosa, Michael, & Mathis, J. S. 1987, ApJ, 317, 163

Schaerer, D., 1996, A&A, 310, 837

Scowen, P. A. et al., 1998, AJ, 116, 163

Smith, R. C., Points, S. D., Chu, Y.H., Winkler, P.F., Augilera, C., Leiton, R., MCELS Team, 2005, AAS, 207, 2507

Townsley, L. K., et al. 2006, AJ, 2006, 131, 2140

Tsamis, Y. G., Barlow, M. J., Liu, X. W., Danziger, I. J., Storey, P. J., 2003, MNRAS, 338, 687

Tsamis, Y. G., Pequignot, D., 2005, MNRAS, 364, 687 (TP03)

Vacca et al. 1996

Veilleux, S., & Osterbrock, D. E., 1987, ApJS, 63, 295

Vermeij et al. 2002

Vilchez, J. M., & Pagel, B. E., 1988, MNRAS, 231, 257

Walborn, N. R., Mais-Apellaniz, J., Barba, R. H., 2002, AJ, 124, 1601

Weingartner, J.C., & Draine, B.T., 2001, AJ, 548, 296

Wen, Z. & O'Dell, 1995, ApJ, 438, 784

Yan, T. T., Kewley, L. J., 2009, ApJ, 699, 161

Yin, S. Y., Liang, Y. C., Hammer, F., Brinchmann, J., Zhang, B., Deng, L. C., & Flores, H., 2007, A&A, 462, 535

# Chapter 3
# Spectroscopic Observations of NGC 3603

## 1 NGC3603 – A Large Star-Forming Region in the Milky Way

NGC 3603 is a large, yet compact Galactic HII region with dozens of O5 to O4 ( M > 35 $M_{\odot}$) stars within a 1 pc diameter. It clearly is one of the most luminous star-forming regions in our own Galaxy. The cluster mass has been estimated to be as high as $10^5$ $M_{\odot}$, half that of R136 with a luminosity equal to $6.1 \times 10^5$ $L_{\odot}$ (Eisenhauer et al. 1998). A recent spectroscopic study of 26 cluster members by Melena et al. (2008) place the nebula at 7.6 kpc, more than 6 times closer than 30 Doradus. In addition to its proximity, the age of the massive stars studied by Melena et al. (2008) suggest the cluster age is between 1-2 Myr. Because of it's youth, the nebula has not yet been disturbed by supernovae and is likely to present a less complex example of star formation than 30 Doradus. The region is further simplified because there are no additional sources of ionization competing with the central cluster, unlike the case of 30 Doradus.

Empirical abundance from optical studies show the log (O/H ) abundance to be -3.29 (Garcia-Rojas et al. 2008), almost 3 times greater than our value for 30 Doradus. In addition to 30 Doradus, Lebouteiller et al. (2008) also obtained abundances for S, Ar, Ne and Fe in NGC 3603 at 7 locations. On average, the abundance of these elements are 0.2 dex greater in NGC 3603 than in 30 Doradus with a scatter of about 0.08. These factors make NGC3603 a logical intermediate step in our study of H II regions as a function of size and abundance as we work our way toward GEHIIRs.

However an optical study of NGC3603 must face a number of challenges. The region

lies in the disk of the Milky Way and has an average extinction $A_V = 5.23$ (see Table 3.3 below). Additional H II regions along the line of sight contaminate any study which, like ours, does not have sufficient velocity resolution to separate the various components. The extinction makes detecting a faint auroral line like [O III] λ4363 in our survey impossible in all but the brightest parts of the nebula. Without a measure of the global gas temperature we cannot directly apply the technique for determining the metal abundances that we used to study 30 Doradus.

In keeping with our original NOAO observing proposal, the spectroscopic grid of NGC 3603 will also be made available to the public along with the reduced data and calibration frames. Due to the additional complications regarding NGC 3603, these data will be presented in a short journal article describing the observations and a few basic results that can be obtained without extensive Cloudy modeling.

**2 SOAR Imaging**

In the same way as was done for 30 Doradus, we took a series of narrow band images with the SOAR Telescope in order to map the spatial structure of NGC 3603 at sub-arcsec resolution. For present purposes, we present mosaic images (Figures 3.1, 3.2 and 3.3) constructed from these observations in two of the band-passes to serve as high-resolution finding charts to show the slit positions of the spectroscopic observations described below. The mosaics presented represent a combination of 4 fields spanning an area 5.3 across. A journal of the full set of SOAR images is presented in Table 3.1. The filters used were a combination of those available through CTIO ( 6850 red continuum, 6563x75, 5130 green continuum) and those generously provided by Frank Winkler

( 6734, 6572 and 5007). As the filters became available over a 2 year time period we observations during three runs: April 4 – 8 2007, Jan 6 & 7 2008 and April 16 & 19. A continuum subtraction of each filter to account for both stellar and scattered light was done in accordance with the description of the 30 Doradus images. The surface brightness profile of each of slit position was checked against these direct images using a combination of emission line and stellar band-passes. The RAs and Declinations reported in Table 3.2 were computed using such a comparison and are accurate to 1 arcsec.

**3 Spectroscopic Observations with the Blanco Telescope**

A full grid of spectra of NGC 3603 were obtained during two observing runs, one on 22 March 2007 and one 8-9 Feb 2008. The NGC 3603 spectra were part of the same program as the 30 Doradus survey, and used the same instrument setup described in section 2.3.1 of chapter 2 of this thesis. The data were reduced using the calibration steps and extraction processes for emission lines that have already been described for 30 Doradus.

It should be noted that there are many fewer detected and extracted lines in the case of NGC 3603 than for 30 Dor, due to the lower apparent surface brightness of NGC 3603. The lines that are strong enough to be extracted automatically are shown in Table 3.3. These are presented at their rest wavelengths because NGC 3603 is essentially at zero velocity with respect to the Sun. Following the format of Tables 2.4 and 2.5 of this thesis, all reddened line fluxes are presented relative to the dereddened Hβ strength. The lines listed here in Table 3.2 include Hβ, Hα and the [S II] λλ 6716,6731 doublet. From these

we measured $A_V$ and the electron density. Both of these quantities are included here in Table 3.4. The average extinction in the nebula is $A_V = 5.23 \pm 1.11$, without correction for outliers effected by the considerable number of field stars. Melena et al (2009) report an E(B-V) of 1.394 ±0.012 for the stars in the cluster, corresponding to an $A_V = 4.31$. Position 8 passes near to the cluster but is far enough that underlying stellar absorption features do not effect the measured emission line strengths. At it's closest approach of 19 arcsec we find $A_V = 4.27$. Tables 3.2-3.4 and the reduced 2D spectra are all available electronically to the public on the same permanent web site where we have posted the 30 Dor data [1].

There are two common emission line diagnostic diagrams available in in Table 3.4 used through out the study of 30 Doradus. These are shown below in Figures 3.4 and 3.5 without a detailed analysis. Figure 3.4 is the diagnostic ([S II] λλ6716+6731)/Hα vs. [O III]/Hβ. Figure 3.5 is the [N II]/Hα vs [O III]/Hβ. Just as in the case of 30 Doradus a large range in the ionization state of the gas is visible in the observations. In an upcoming paper we will apply the results from 30 Doradus and combine the existing empirical abundances in the literature with photo ionization models to measure the ionization parameter. This will require data to constrain the gas temperature. Some observations may be found in the literature for a small number of positions, but given the importance of the [O III] abundance to the gas temperatures in 30 Dor, additional observations are likely required to proceed.

[1] http/www.pa.msu.edu/astro/thesis/pellegrini/ngc3603/

Table 3.1: The direct imaging observing journal for NGC 3603. These observations span 2 years and the exact number and duration of exposures in each 4 fields vary slightly by field.

| Table 3.1<br>DETAILS OF NARROWBAND OBSERVATIONS OF NGC3603 | | | | |
|---|---|---|---|---|
| Filter | No. of Exp x Duration at each position | No. Positions | FWHM (arcsec) | Min/Max Exposure(s) |
| 6563 | 3 x 300s | 4 | 0.7 | 300/4000 |
| 6572 | 3 x 300s | 4 | 0.5-0.8 | 590/3200 |
| 6734 | 7 x 600s | 5 | 0.85 | 4000/14000 |
| 6850 | (Number of exposures matched to each read frame) | 5 | 0.5 -1 | 900/5700 |
| 5007 | 3 x 200s | 4 | 0.7-0.8 | 400/1800 |
| 5130 | 3 x 300s | 4 | 0.7-0.8 | 600/2400 |

Table 3.2: The coordinates of the NGC 3603 slit positions with position angle and total exposure time, excluding short exposures used to fix saturation.

| Table 3.2 Journal of NGC 3603 Spectroscopic Observations | | | | |
|---|---|---|---|---|
| Pos | R.A. (2000) | Dec. (2000) | PA (deg E of N) | Exposure Time (s) |
| 1 | 11:15:29.45 | -61:18:17.46 | 57 | 750 |
| 2 | 11:15:26.36 | -61:17:32.62 | 57 | 600 |
| 3 | 11:15:18.90 | -61:17:28.03 | 57 | 900 |
| 4 | 11:15:14.99 | -61:17:13.20 | 57 | 600 |
| 5 | 11:15:13.39 | -61:16:41.09 | 57 | 900 |
| 6 | 11:15:10.79 | -61:16:28.09 | 57 | 450 |
| 7 | 11:15:07.96 | -61:16:25.27 | 57 | 900 |
| 8 | 11:15:03.38 | -61:16:20.31 | 57 | 600 |
| 9 | 11:15:02.79 | -61:16:01.81 | 57 | 800 |
| 10 | 11:15:02.79 | -61:16:01.81 | 57 | 900 |
| 11 | 11:15:03.44 | -61:15:34.46 | 57 | 900 |
| 12 | 11:15:01.07 | -61:15:03.31 | 57 | 900 |
| 13 | 11:14:58.46 | -61:14:41.34 | 57 | 900 |
| 14 | 11:15:27.72 | -61:13:27.59 | 57 | 600 |
| 15 | 11:15:18.38 | -61:11:53.69 | 57 | 630 |
| 20 | 11:15:28.48 | -61:16:23.42 | 147 | 600 |
| 21 | 11:15:20.86 | -61:15:32.58 | 147 | 900 |
| 22 | 11:15:16.51 | -61:15:43.90 | 147 | 900 |
| 23 | 11:15:21.61 | -61:17:04.51 | 147 | 550 |
| 24 | 11:15:13.52 | -61:15:55.11 | 147 | 900 |
| 25 | 11:15:14.81 | -61:16:38.09 | 147 | 500 |
| 26 | 11:15:07.71 | -61:15:43.98 | 147 | 900 |
| 27 | 11:15:07.01 | -61:16:02.37 | 147 | 500 |
| 28 | 11:15:07.36 | -61:16:24.85 | 147 | 450 |
| 29 | 11:14:53.93 | -61:16:46.67 | 147 | 900 |

| Table 3.2 (cont'd) | | | | |
|---|---|---|---|---|
| 30 | 11:14:51.16 | -61:17:00.13 | 147 | 1350 |
| 31 | 11:15:18.62 | -61:16:33.51 | 147 | 300 |
| 32 | 11:15:13.00 | -61:14:05.72 | 147 | 630 |

Table 3.3: Emission lines identified in the NGC 3603 survey.

| Table 3.3 NGC 3603 Line IDs | | |
|---|---|---|
| $\lambda_0$ | ion | $f_\lambda(R = 3.1)$ |
| 4341 | H I | 1.35 |
| 4800 | Continuum | 1.19 |
| 4861 | H I | 1.16 |
| 4959 | [O III] | 1.13 |
| 5007 | [O III] | 1.12 |
| 5650 | Continuum | 0.97 |
| 5875 | He I | 0.93 |
| 6300 | [O I] | 0.86 |
| 6312 | [S III] | 0.86 |
| 6548 | [N II] | 0.82 |
| 6563 | H I | 0.82 |
| 6584 | [N II] | 0.81 |
| 6678 | He I | 0.80 |
| 6716 | [S II] | 0.79 |
| 6731 | [S II] | 0.79 |
| 7065 | He I | 0.74 |
| 7135 | [Ar III] | 0.73 |

Table 3.4: A portion of the reddening-corrected NGC 3603 Blanco spectroscopic survey in table form as described in the text. The first several rows of slit position 1 are shown. Together there are 28 unique slit positions with line-strength measurements at a total of 2950 extracted locations within a 6x6 arc min area. The units of electron density are $cm^{-3}$. The dereddened Hβ surface brightnesses are reported in units of erg $s^{-1}$ $cm^{-2}$ $arcsec^{-2}$. The other emission lines are reported as 100×S(line)/S(Hβ).

TABLE 3.4
EXAMPLE OF PUBLICLY AVAILABLE SCIENCE PRODUCT FROM BLANCO SPECTROPHOTOMETRIC SURVEY OF NGC 3603

| Slit # | ΔR A | ΔDec | row | log(ne) | -err | +err | Av | F(Hb) | I(Hb) | sig | 4341 | sig | 4959 | sig |
|---|---|---|---|---|---|---|---|---|---|---|---|---|---|---|
| 1 | 2 | 3 | 4 | 5 | 6 | 7 | 8 | 9 | 10 | 11 | 12 | 13 | 14 | 15 |
| 1 | 31.6 | -240.9 | 3 | <1.00 | 1.00 | 1.91 | 5.49 | 1.33E-15 | 5.21E-13 | 4.47E-14 | 64.9 | 32.9 | 36.00 | 6.38 |
| 1 | 33.8 | -239.6 | 8 | <1.00 | 1.00 | 0.00 | 4.28 | 2.12E-15 | 2.23E-13 | 9.65E-15 | 0.54 | 0.13 | 37.79 | 3.32 |
| 1 | 35.9 | -238.2 | 13 | 1.76 | 0.47 | 0.24 | 3.9 | 2.39E-15 | 1.65E-13 | 6.34E-15 | 0.57 | 0.11 | 31.13 | 2.97 |
| 1 | 38.0 | -236.8 | 18 | 1.83 | 0.33 | 0.20 | 4.05 | 2.38E-15 | 1.94E-13 | 7.44E-15 | 0.49 | 0.11 | 32.97 | 2.94 |
| 1 | 40.1 | -235.5 | 23 | 1.37 | 0.37 | 0.41 | 4.47 | 1.99E-15 | 2.55E-13 | 1.17E-14 | 0.40 | 0.15 | 37.59 | 3.46 |
| 1 | 42.2 | -234.1 | 28 | 1.49 | 0.49 | 0.34 | 4.37 | 2.21E-15 | 2.55E-13 | 1.05E-14 | 0.43 | 0.13 | 38.48 | 3.09 |
| 1 | 44.3 | -232.7 | 33 | 1.49 | 0.49 | 0.32 | 4.48 | 2.23E-15 | 2.89E-13 | 1.17E-14 | 0.58 | 0.13 | 38.79 | 3.05 |
| 1 | 46.5 | -231.3 | 38 | 1.86 | 0.23 | 0.16 | 4.36 | 2.46E-15 | 2.81E-13 | 1.04E-14 | 0.47 | 0.12 | 39.64 | 2.77 |
| 1 | 48.6 | -230.0 | 43 | 1.91 | 0.20 | 0.14 | 4.42 | 2.55E-15 | 3.12E-13 | 1.11E-14 | 0.40 | 0.11 | 47.03 | 2.67 |
| 1 | 50.7 | -228.6 | 48 | 2.16 | 0.11 | 0.09 | 4.52 | 2.29E-15 | 3.11E-13 | 1.22E-14 | 0.50 | 0.13 | 58.25 | 2.97 |
| 1 | 52.8 | -227.2 | 53 | 2.21 | 0.12 | 0.10 | 4.43 | 2.12E-15 | 2.63E-13 | 1.11E-14 | 0.37 | 0.14 | 36.88 | 3.18 |

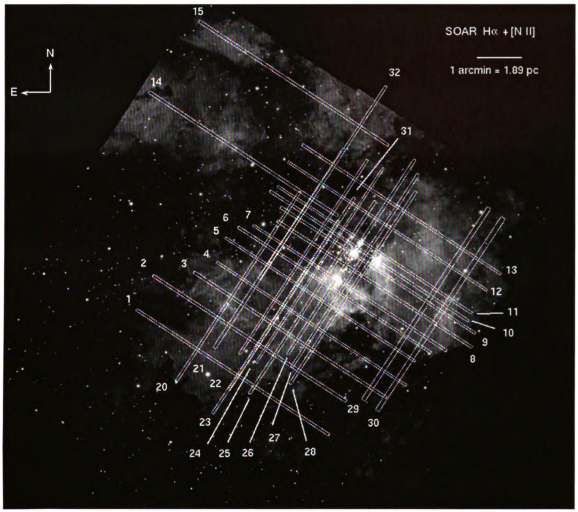


Figure 3.1: Narrow-band Hα mosaic image of NGC 3603, from observations using the SOAR telescope. The NGC3603 Blanco slit positions are shown with labels. Slits with position angles PA = 147 deg are labeled 1-15. Observations with PA = 57 deg are labeled 20-32. A 1 arcmin scale bar is shown along with the projected physical scale assuming a distance of 6.5 kpc.

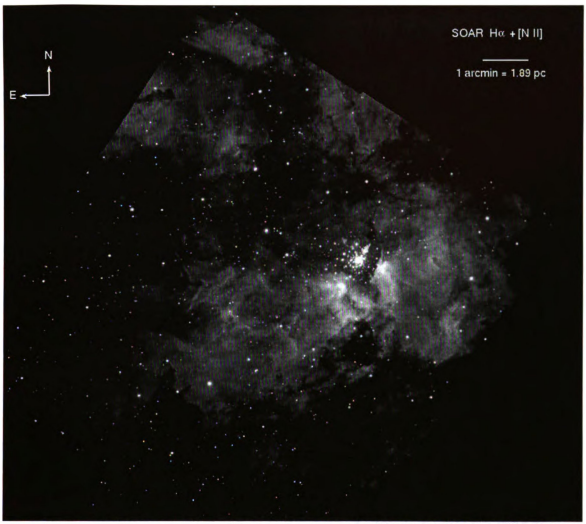


Figure 3.2: The same Hα mosaic image of NGC 3603 as in Figure 3.1, without the observed slit positions super imposed.

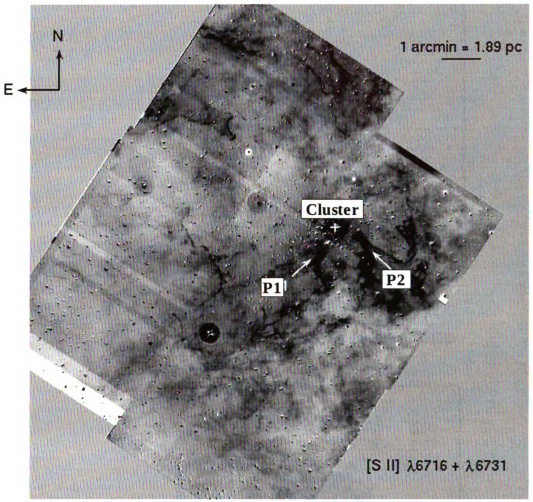


Figure 3.3: An [S II] mosaic covering the same field as Figure 3.1, also created from observations using the SOAR telescope. Two predominate pillars, P1 and P2 are indicated. These were observed extensively in our spectroscopic survey, with multiple position angles.

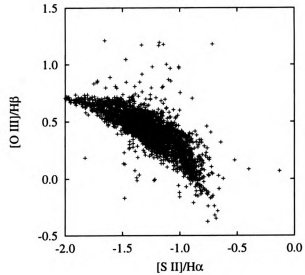


Figure 3.4: The emission line diagnostic ([S II] 6716+6731)/Hα vs [OIII]/Hβ from the NGC 3603 Blanco data. A higher degree of ionization corresponds to lower [S II]/Hα and high [O III]/Hβ.

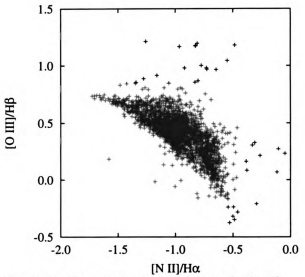


Figure 3.5: The emission line diagnostic plot [N II] 6584/Hα vs. [O III]/Hβ from the NGC 3603 Blanco data. A higher degree of ionization corresponds to lower [N II]/Hα and high [O III]/Hβ. This is analogous to Figure 3.4.

References

Eisenhauer, F., Quirrenbach, A., Zinnecker, H., Genzel, R., 1998, ApJ, 498, 278

Garcia-Rojas, J., Esteban, C., Peimbert, M., Costado, M. T., Rodriguez, M., Peimbert, A., Ruiz, M. T., 2006, MNRAS, 368, 253

Lebouteiller, V., Bernard-Salas, J., Brandl, B., Whelan, D. G., Wu, Yanling, Charmandaris, V., Devost, D., Houck, J. R., 2008, ApJ, 680, 398L

Melena, N. W., Massey, P., Morrell, N. I., Zangari, A. M., 2008, AJ, 135, 878